

AD-A148 810

IMPROVED MATERIALS AND PROCESSES OF DISPENSER CATHODES

1/2

(U) HUGHES AIRCRAFT CO TORRANCE CA ELECTRON DYNAMICS

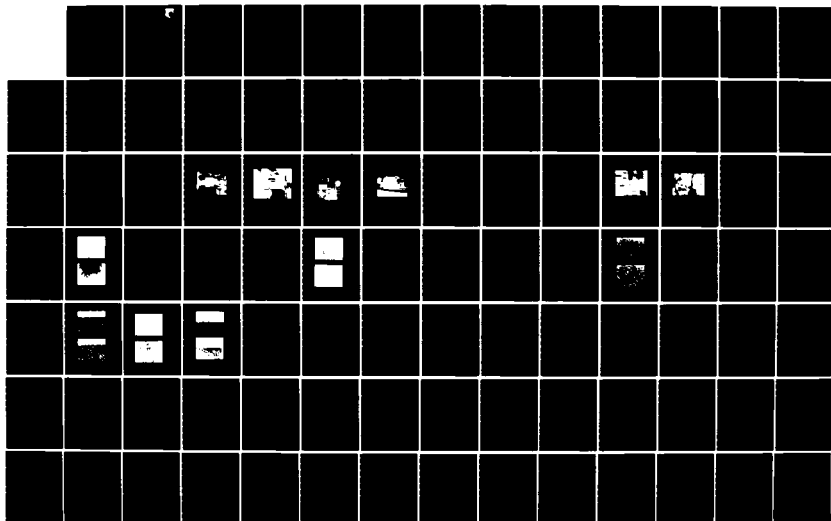
DIV R T LONGO ET AL AUG 84 EDD-W-09514

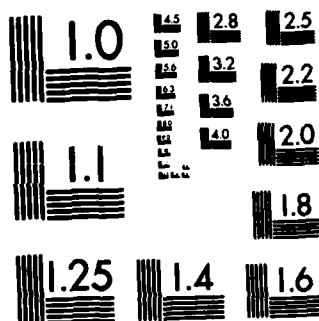
UNCLASSIFIED

AFWAL-TR-84-4072 F33615-80-C-5191

F/G 9/1

NL

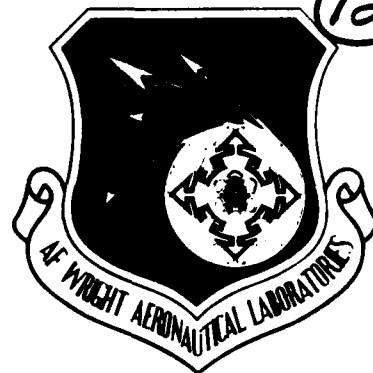




MICROCOPY RESOLUTION TEST CHART  
NATIONAL BUREAU OF STANDARDS-1963-A

AD-A148 810

AFWAL-TR-84-4072



IMPROVED MATERIALS AND PROCESSES OF DISPENSER CATHODES

R. T. Longo  
W. F. Sundquist  
E. A. Adler

HUGHES AIRCRAFT COMPANY  
Electron Dynamics Division  
P.O. Box 2999  
Torrance, CA 90509

AUGUST 1984

FINAL REPORT FOR PERIOD 1 APRIL 1980 TO 1 APRIL 1984

APPROVED FOR PUBLIC RELEASE; DISTRIBUTION UNLIMITED

MATERIALS LABORATORY  
AIR FORCE WRIGHT AERONAUTICAL LABORATORIES  
AIR FORCE SYSTEMS COMMAND  
Wright-Patterson AFB, Ohio 45433

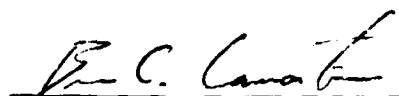
84 12 17 082

## NOTICE

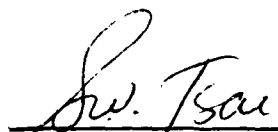
*When Government drawings, specifications, or other data are used for any purpose other than in connection with a definitely related Government procurement operation, the United States Government thereby incurs no responsibility nor any obligation whatsoever; and the fact that the Government may have formulated, furnished, or in any way supplied the said drawings, specifications, or other data, is not to be regarded by implication or otherwise as in any manner licensing the holder or any other person or corporation, or conveying any rights or permission to manufacture, use, or sell any patented invention that may in any way be related thereto.*

*This report has been reviewed by the Office of Public Affairs (ASD/PA) and is releasable to the National Technical Information Service (NTIS). At NTIS, it will be available to the general public, including foreign nations.*

*This technical report has been revised and is approved for publication.*



BRUCE C. LAMARTINE  
Materials Research Engineer  
Mechanics & Surface Interactions Br



STEPHEN W. TSAI, Chief  
Mechanics & Surface Interactions Br  
Nonmetallic Materials Division

FOR THE COMMANDER



FRANKLIN D. CHERRY, Chief  
Nonmetallic Materials Division

*"If your address has changed, if you wish to be removed from our mailing list, or if the addressee is no longer employed by your organization please notify AFWAL/MLBM, W-PAFB, Ohio 45433 to help us maintain a current mailing list."*

*Copies of this report should not be returned unless return is required by security considerations, contractual obligations, or notice on a specific document.*

Unclassified

SECURITY CLASSIFICATION OF THIS PAGE

## REPORT DOCUMENTATION PAGE

1a. REPORT SECURITY CLASSIFICATION Unclassified			1b. RESTRICTIVE MARKINGS N/A	
2a. SECURITY CLASSIFICATION AUTHORITY N/A			3. DISTRIBUTION/AVAILABILITY OF REPORT Approved for public release; distribution unlimited.	
2b. DECLASSIFICATION/DOWNGRADING SCHEDULE N/A				
4. PERFORMING ORGANIZATION REPORT NUMBER(S) W-09514			5. MONITORING ORGANIZATION REPORT NUMBER(S) AFWAL-TR-84-4072	
6a. NAME OF PERFORMING ORGANIZATION Hughes Aircraft Company		6b. OFFICE SYMBOL (If applicable) AFWAL/MLBM	7a. NAME OF MONITORING ORGANIZATION Mechanics & Surface Interactions Branch	
6c. ADDRESS (City, State and ZIP Code) Electron Dynamics Division 3100 West Lomita Blvd, P.O. Box 2999 Torrance, CA 90509			7b. ADDRESS (City, State and ZIP Code) AFWAL/MLBM WPAFB, OH 45433	
8a. NAME OF FUNDING/SPONSORING ORGANIZATION Materials Laboratory		8b. OFFICE SYMBOL (If applicable) AFWAL/MLBM	9. PROCUREMENT INSTRUMENT IDENTIFICATION NUMBER F33615-80-C-5191	
8c. ADDRESS (City, State and ZIP Code) Same as 7b.			10. SOURCE OF FUNDING NOS.	
			PROGRAM ELEMENT NO. 61102F	PROJECT NO. 2303
			TASK NO. 01	WORK UNIT NO. 06
11. TITLE (Include Security Classification) Improved Materials & Processes of Dispenser Cathodes				
12. PERSONAL AUTHOR(S) R. T. Longo, W. F. Sundquist, E. A. Adler				
13a. TYPE OF REPORT Final Report		13b. TIME COVERED FROM 1980 TO 1984		14. DATE OF REPORT (Yr., Mo., Day) August 1984
15. PAGE COUNT 165				
16. SUPPLEMENTARY NOTATION				
17. COSATI CODES			18. SUBJECT TERMS (Continue on reverse if necessary and identify by block number)	
FIELD 09	GROUP 01	SUB. GR.	Thermionic Emission, Dispenser Cathode, Impregnated Cathode, M-Type Cathode	
19. ABSTRACT (Continue on reverse if necessary and identify by block number)				
<p>Several process variables affecting the final electron emission properties of impregnated dispenser cathodes were investigated. In particular, the influence of billet porosity, impregnant composition and purity, and osmium-ruthenium coating were studied.</p> <p>Work function and cathode evaporation data were used to evaluate cathode performance and to formulate a model of cathode activation and emission.</p> <p>Results showed that sorted tungsten powder can be reproducibly fabricated into cathode billets. Billet porosity was observed to have the least effect on cathode performance. Use of the 4:1:1 aluminate mixture resulted in lower work functions than did use of the 5:3:2 mixture. Under similar drawout conditions, the coated cathodes showed superior emission relative to uncoated cathodes. In actual Pierce gun structures under accelerated life test, the influence of impregnant sulfur is clearly shown to reduce cathode performance.</p>				
20. DISTRIBUTION/AVAILABILITY OF ABSTRACT UNCLASSIFIED/UNLIMITED <input type="checkbox"/> SAME AS RPT. <input checked="" type="checkbox"/> DTIC USERS <input type="checkbox"/>			21. ABSTRACT SECURITY CLASSIFICATION Unclassified	
22a. NAME OF RESPONSIBLE INDIVIDUAL Bruce C. Lamartine			22b. TELEPHONE NUMBER (Include Area Code) (513) 255-5892	22c. OFFICE SYMBOL AFWAL/MLBM

## TABLE OF CONTENTS

<u>Section</u>	<u>Page</u>
1.0 INTRODUCTION	1-1
2.0 BACKGROUND	2-1
2.1 General Review of the Tungsten Dispenser Cathode	2-1
2.2 The Physics and Chemistry of the Tungsten Dispenser Cathode	2-5
2.3 Transport of the Active Material to the Emitter Surface	2-8
2.4 Surface Chemistry and Physics	2-11
3.0 FACILITIES AND EQUIPMENT	3-1
3.1 HEDD Dispenser Cathode Fabrication Facilities	3-1
3.2 Emission Testing Process Evaluation Tester (PET)	3-1
3.3 Barium Evaporation Measurements	3-7
4.0 MATERIALS AND CATHODE MANUFACTURING	4-1
4.1 Tungsten Powders	4-1
4.2 Tungsten Billets	4-12
4.3 Aluminate and Aluminate Material	4-14
4.4 M-Coating	4-17
4.5 Sample Preparation	4-18
4.6 Cathode Geometry and Identification	4-21
5.0 CATHODE MEASUREMENT	5-1
5.1 Cathode Activation	5-1
5.2 Pulsed Cathode Characteristics	5-1
5.3 Evaluation of Cathode Characteristics	5-6
5.4 Evaporation Rate Measurements	5-13
6.0 RESULTS AND DISCUSSIONS	6-1
6.1 Workfunction Distribution	6-1
6.2 Barium Evaporation	6-38
6.3 Dependence of Workfunction on Evaporation Rate	6-38
6.4 Effects of Impurities	6-43
7.0 THEORETICAL MODELING OF THE DISPENSER CATHODE	7-1
7.1 Evaluation of Emission Current	7-2
7.2 Surface Coverage Workfunction Model	7-7
7.3 Barium Evaporation Rate	7-15

# TABLE OF CONTENTS (CONTINUED)

<u>Section</u>	<u>Page</u>
7.4 Modeling Surface Coverage With Barium Evaporation Rate	7-16
7.4.1 Geometric Factor	7-17
7.4.2 Analysis of Data With Surface Coverage Model	7-19
7.5 Summarizing the Model	7-22
7.6 Final Remarks	7-24
8.0 CONCLUDING REMARKS	8-1
8.1 Further Work	8-2
8.2 Acknowledgement	8-2
<u>Appendix</u>	
A UNIVERSAL THERMIONIC EMISSION CURVE	A-1
B BARIUM EVAPORATION DATA	B-1

Accession For	
NTIS GRA&I	<input checked="" type="checkbox"/>
DTIC TAB	<input type="checkbox"/>
Unannounced	<input type="checkbox"/>
Justification	
By _____	
Distribution/	
Availability Codes	
Dist	Avail. for
A-1	



## LIST OF ILLUSTRATIONS

<u>Figure</u>	<u>Page</u>
3.1-1 View of the cathode laboratory showing the hydrogen furnace, vacuum furnace and air furnace.	3-2
3.1-2 View of the cathode laboratory showing inspection, analysis and assembly areas.	3-3
3.1-3 High temperature hydrogen furnace for sintering tungsten and aluminum oxide potting material.	3-4
3.1-4 Hydrogen furnace for infiltrating the billets with copper.	3-5
3.2-1 Schematic drawing of the PET test equipment.	3-6
3.2-2 Schematic of the PET with data acquisition system.	3-8
3.2-3 Photograph of the Process Evaluation Tester (PET).	3-9
3.2-4 This photograph shows the inside of the PET vacuum system.	3-10
4.1-1 1500x SEM photomicrographs of (a) U4.5 and (b) U9.5 tungsten powder before classification.	4-4
4.1-2 Distribution of unclassified tungsten powder U4.5.	4-5
4.1-3 Distribution of unclassified tungsten powder U9.5.	4-6
4.1-4 1500x SEM photomicrographs of the classified powders.	4-8
4.1-5 Distribution of classified tungsten powder, 5 micron.	4-9
4.1-6 Distribution of classified tungsten powder, 11 micron.	4-10
4.2-1 1000x photomicrographs of the (a) 5 micron billet and the (b) 11 micron billet.	4-13
4.4-1 1000x photomicrograph of the M-coating on the (a) cathode made from a 5 micron billet and (b) a cathode made from an 11 micron billet.	4-18
4.4-2 SEM of emitter surface of (a) an uncoated cathode and (b) a coated cathode.	4-19



# LIST OF ILLUSTRATIONS (CONTINUED)

<u>Figure</u>		<u>Page</u>
4.5-1	(a) Shows the results of a 5 minute water etch, the etch depth is 10 microns. (b) Is the results of a 10 minute water etch, the etch depth is 30 microns.	4-20
4.6-1	Cathode print.	4-22
5.2-1	Digital pulsed curve which shows the typical pulse and position on the pulse at which the measurements were made.	5-2
5.2-2	Current density-voltage-temperature ( $^{\circ}\text{K}$ ) characteristic at cathode-to-anode spacing of 0.22 cm.	5-3
5.2-3	Current density-voltage-temperature ( $^{\circ}\text{K}$ ) characteristics at cathode-to-anode spacing of 0.15 cm.	5-4
5.2-4	Current density-voltage-temperature ( $^{\circ}\text{K}$ ) characteristics at cathode-to-anode spacing of 0.08 cm.	5-5
5.3-1	Schottky plot of data using equation 1 to fit data.	5-7
5.3-2	Schottky plot of data using equation 1 to fit data.	5-8
5.3-3	Schottky plot of data using equation 1 to fit data.	5-9
5.3-4	Schottky plot using the Schottky technique to fit the data.	5-10
5.3-5	Schottky plot using the Schottky techniques to fit the data.	5-11
5.3-6	Schottky plot using the Schottky technique to plot the data.	5-12
6.1-1	Single histogram combining all cathode measured in this program.	6-7
6.1-2	All tungsten cathodes.	6-8
6.1-3	All OsRu coated cathodes.	6-9
6.1-4	All S-type, OSRu coated cathodes.	6-10

# LIST OF ILLUSTRATIONS (CONTINUED)

<u>Figure</u>		<u>Page</u>
6.1-5	S-type classified OsRu coated.	6-11
6.1-6	S-type unclassified, OsRu coated.	6-12
6.1-7	All B-type OsRu coated.	6-13
6.1-8	B-type classified OsRu coated.	6-14
6.1-9	B-type unclassified OsRu coated.	6-15
6.1-10	All S-type tungsten.	6-16
6.1-11	S-type classified tungsten.	6-17
6.1-12	S-type unclassified tungsten.	6-18
6.1-13	All B-type tungsten.	6-19
6.1-14	B-type classified tungsten.	6-20
6.1-15	B-type unclassified, tungsten.	6-21
6.1-16	B-type 5 micron tungsten.	6-22
6.1-17	B-type 11 micron tungsten.	6-23
6.1-18	S-type 5 micron tungsten.	6-24
6.1-19	S-type 11 micron tungsten.	6-25
6.1-20	B-type 5 micron Osmium: Ruthenium.	6-26
6.1-21	B-type 11 micron Osmium: Ruthenium.	6-27
6.1-22	S-type 5 micron Osmium: Ruthenium.	6-28
6.1-23	S-type 11 micron Osmium: Ruthenium.	6-29
6.1-24	B-type 5 micron unclassified tungsten.	6-30
6.1-25	B-type 11 micron unclassified tungsten.	6-31
6.1-26	S-type 5 micron unclassified tungsten.	6-32

# LIST OF ILLUSTRATIONS (CONTINUED)

<u>Figure</u>		<u>Page</u>
6.1-27	S-type 11 micron unclassified tungsten.	6-33
6.1-28	B-type 5 micron unclassified Osmium: Ruthenium.	6-34
6.1-29	B-type 11 micron unclassified Osmium: Ruthenium.	6-35
6.1-30	S-type 5 micron unclassified Osmium: Ruthenium.	6-36
6.1-31	S-type 11 micron unclassified Osmium: Ruthenium.	6-37
6.3-1	The expected value of the work function vs barium evaporation rate.	6-40
6.3-2	The minimum value of the work function vs barium evaporation rate.	6-41
6.4-1	Histogram of HEDD life tests. The solid line is a gamma function with parameters $\min = 2.028$ ev, expected value = 2.13 ev and standard deviation = 0.004 ev.	6-44
6.4-2	Life test results in a 877HA Pierce gun vehicle.	6-47
7.2-1	Schematic microscopic view of dipole coated surface for different value of the microscopic variable $\theta$ .	7-8
7.2-2	Minimum work function vs $\Gamma$ .	7-13
7.2-3	Average work function $\phi(\theta/\theta_m)$ vs $\theta/\theta_m$ .	7-14
7.4-1	Geometry used to calculate the geometric factor.	7-18
7.4.2	Temperature dependence of diffusional surface coverage.	7-21

## LIST OF TABLES

<u>Tables</u>	<u>Page</u>
4.1-1 Chemical Analysis By General Electric	4-2
4.1-2 Chemical Test of Tungsten Power (Not included in report.)	4-3
4.1-3 Tungsten Particle Size Classification	4-7
4.1-4 Powder Identification	4-11
4.2-1 Billets G.E. Power	4-12
4.3-1 Basic Aluminate Component Raw Materials	4-15
4.3-2 Aluminate Mixes	4-15
4.3-3 Sulfur Analysis On Aluminate Lots	4-16
4.6-1 Cathode Identification	4-21
6.1-1 Gamma Distribution Parameters Obtained By Fit To Work Function Histograms	6-5
6.1-2 Gamma Distribution Parameters Obtained By Fit To Work Function Histograms	6-6
6.2-1 Parameters of Barium Evaporation Measurements	6-39
7.4-1 Summary of Surface Coverage Parameters	7-23
7.4-2 Sticking Times ( $10^{-12}$ sec)	7-23

## 1.0 INTRODUCTION

As the need for higher current density cathodes increases the interest in the dispenser cathode has also increased. The parameters that control the performance of the dispenser cathode are many and to this time have not been thoroughly or systematically studied.

This program was designed to study several of what are believed to be the important process parameters controlling the dispenser cathode's emission characteristics.

The parameters under study are:

1. The billet porosity at constant billet density.
2. The aluminate, using both the (4:1:1) and the (5:3:2) mixes,
3. The surface coating using the uncoated tungsten surface and the osmium-ruthenium coated surface.

The basic goal of the program was to manufacture and test cathodes which varied in each of the processed parameters listed above. Half of the manufactured cathodes were sent to Wright-Patterson where surface analysis studies are to be carried out. The remaining half were studied in this laboratory. Extensive work function and evaporation measurements were made and are reported here.

The basic expectations of the program are to determine how each of the process parameters affect the initial life emission performance of the cathodes and to model the performance of the cathodes to the extent possible with the data available at the conclusion of the work at this laboratory. It is clear that a complete physical model cannot be undertaken with just the work function and evaporation data. The results of the detailed surface study must be obtained to successfully complete the modeling task.

We shall develop however, some empirical modeling ideas that have interested us for some time and attempt to evaluate our data against these ideas. The reader must fully understand that these models are not to be taken too seriously at this point, at least until more fundamental data can be obtained to substantiate them.

This work, we believe, has succeeded with its basic goals. The data does reveal a systematic and quite reasonable result. The coated cathodes clearly exhibit superior performance, as was fully expected. The aluminate type was clearly the next most sensitive parameter, the (4:1:1) having a considerable lower work function than did the (5:3:2) type aluminate. The billet porosity had the least effect, not affecting the work function at all, and having only a small effect on the evaporation rate.

## 2.0 BACKGROUND

### 2.1 GENERAL REVIEW OF THE TUNGSTEN DISPENSER CATHODE

The first cathode of technological importance under the classification of dispenser cathode is the tungsten dispenser cathode developed by Lemmens et. al.<sup>1</sup> The L-type cathode (1950) has been used since that time and is still in use today. The L-type cathode is constructed by using a thin, porous matrix to seal a reservoir of the active Ba carbonate. The activation processes generate free Ba and BaO which transport from the reservoir through the porous tungsten matrix emerging onto the emitter surface. In principle, the reservoir can be made large enough to obtain very long life from this cathode. In practice, there may be limitations due to the chemical reaction products that form in the reaction reservoir. These reaction products tend to impede the reaction, thus slowing down the generation of Ba and BaO. Research on the L-type cathode continues, the latest version called the controlled porosity cathode (CPD).<sup>2</sup> This variation is effectively the same as the earlier L-type except it replaces the porous tungsten plug with a thin tungsten foil having a uniform array of laser drilled holes. The main reason for this design is to improve the uniformity of emission and to control the flow rate of active components to the emitter surface. Using the technology provided by laser drilling, in principle one can design the most efficient dispensing surface. The reported results on the CPD are very promising. It is clear that the L-type construction is an important development in the technology of cathodes based on its use and continued development.

One of the difficulties usually encountered with the L-type of cathode is in obtaining a vapor tight enclosure for the reservoir, which is necessary to assure that the Ba and BaO emerges through the pores onto the emitter surface. Ba carbonate use in the reservoir usually takes considerable activation time since the carbonates must be reduced within the reservoir and the gaseous product pumped away through the restrictive porous plug. The conversion of the carbonates is very temperature sensitive. Hughes et al.<sup>3</sup> showed that when the temperature is too high, unwanted reactions occur which tie up the Ba in the form of  $BaWO_6$ . At low temperatures, the time for activation is

restrictive. Actually, there is a very narrow usable range of temperatures for the activation of this L-type cathode. The use of preconverted carbonates, as in the new CPD type, speeds up the activation substantially.

To overcome fabrication difficulties created by the need for a vapor tight reservoir, Levi<sup>4</sup> developed the impregnated tungsten dispenser cathode. The first of these cathodes was called the A-type cathode and consisted of a porous plug of tungsten filled with a Ba-Al oxide. The impregnation of the porous plug is usually accomplished in an atmosphere of hydrogen.

Comparing emission characteristics of the A-type and the L-type cathode shows that the A-type has about 5 times lower emission than does the L-type cathode. The reason for this reduction is not fully understood. One of the big manufacturing differences is that the Ba-aluminate must be melted in the presence of tungsten to affect the impregnation.

The impregnated dispenser cathode is very reliable and is becoming very popular among users. The reliability and life of this cathode are becoming quite acceptable even for use in space where long life is expected.

The A-type dispenser cathode was followed by the B-type dispenser cathode. Levi<sup>5</sup> found that emission could be considerably improved by adding calcium oxide to the barium and aluminum oxide of the A-type. The B-type is generally known by the molar ratio of its aluminate (5:3:2) - representing 5 moles of BaO, 3 moles of CaO, and 2 moles of Al<sub>2</sub>O<sub>3</sub>. A number of other aluminate mixes have evolved and become popular. The S-type which was introduced by Semicon, Inc. has a (4:1:1) molar ratio. Although many different ratios have been used, only two, the B-type (5:3:2) and S-type (4:1:1), have special names.

Efforts to improve and optimize the Ba-Ca-Aluminate led Zalm and van Stratum<sup>6</sup> to deposit osmium over the tungsten surface of a finished tungsten dispenser cathode. The resulting cathode is generally known as the M-type or metal coated cathode and operates about 100 K cooler than does the uncoated cathode. Presently, ruthenium is added to the osmium primarily to improve its stability



to atmospheric exposure and to reduce the toxic properties of Os for improved handling. The physics of the surface work function are not yet fully understood. There have been suggestions (cf Green)<sup>7</sup> that the real effect of the Os or Os-Ru is to increase the dwell time of the activation material on the surface, thus increasing the surface coverage. The M-type cathodes have excellent properties in general, but they do suffer from a tendency to peel if the coating is not applied under exacting conditions. This, however, is not a fundamental problem and can be overcome by careful attention to processing details. A fundamental effect that is observed, however, is the diffusion of the layer with the tungsten substrate. This diffusion, it is suggested by Tuck<sup>8</sup>, has a beneficial effect on the emission until an optimum W-Os alloy, the  $\gamma$  phase, is reached. The observed emission of this cathode increases with time. As the relative surface concentration of tungsten increases, the cathode is expected to revert to the uncoated properties. Relatively recently, the so-called mixed metal matrix dispenser cathode has appeared (cf Falce)<sup>9</sup> and shows great promise as a high current density, long life dispenser cathode. The mixed metal cathode, instead of overcoating the emitter surface, mixes a percentage of powders of other materials -Ir, Os or Re -into the tungsten powder before the matrix is pressed. The work function and the operating temperature of the mixed metal cathode are reduced by an amount comparable to the M-type cathode of similar material.

The physics of the emitter surface is generally believed to be a surface layer dipole over the tungsten surface. The precise nature of the dipole is in question although numerous experiments are consistent with a tungsten-oxygen-barium hypothesis.

There has been some controversy as to the thickness of the surface dipole layer on the emitter surface. Both thin monolayer films as well as thick semiconducting films have been hypothesized (cf Beck and Ahmed).<sup>10</sup> Recent experiments using AES by Forman<sup>11</sup> and independently by Green<sup>12</sup> have shown the dipole surface coverage to be monolayer or less.

With the advent of satellited communication systems, cathode life has become a very important technological consideration. Until 1977, it was believed by most specialists that the dispenser cathode would perform with a steady current (while operating space charge limited) until the barium supply was exhausted, whereupon the cathode current would decrease suddenly.

Forman<sup>13</sup> found that with synthesized dispenser cathode surfaces, the surface coverage decreased with time. Rittner<sup>14</sup> suggests that his results showed that the current would remain constant with time. Longo<sup>15</sup> found in accelerated life tests on tungsten dispenser cathodes, that the current decreased with time even though the devices (Pierce<sup>16</sup> gun electrostatically focused triodes) were operated well into the space charge limited region. A physical model that relates the current degradation to the decrease in surface coverage was developed. The model described the accelerated life tests quite well. The model developed by Longo supports Forman's observations of time dependent surface coverage. The discrepancy between the different observations was linked to the close spaced parallel plate diode, which had been the standard test vehicle up to that time.

Life tests of various dispenser cathodes had also been underway at Watkins-Johnson since 1971, sponsored by NASA under the direction of Forman.<sup>17</sup> These life tests showed the same degradation effects as did the Hughes accelerated life tests.

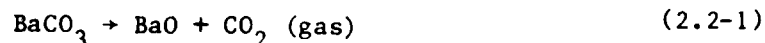
Since then, others have reported similar behavior in dispenser cathodes. Shroff and Palluel<sup>18</sup> reported on their extensive work with B, S and M-type cathodes as well as with mixed metal cathodes. They reported that the degradation followed the same  $t^{-1/2}$  functional behavior as reported by Longo.

At present, it is widely accepted that the degradation observed in the tungsten dispenser cathode is a universal effect. This effect must be considered in the design of systems using the dispenser cathodes.

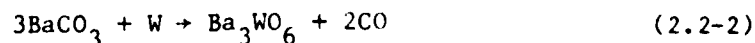
## 2.2 THE PHYSICS AND CHEMISTRY OF THE TUNGSTEN DISPENSER CATHODE

In general, the physics and chemistry of the dispenser cathode is considerably simpler than that of the oxide coated cathode. There, we were faced with the problem of distinguishing between surface and bulk properties, but with the dispenser cathode we must be concerned with: 1) the generation and the transport of the active material to the emitter surface; 2) the physical properties of the emitter surface, both the coverage of the active material and the metal coating that might be applied; and 3) changes that occur with time in both the surface coverage of active material and the metal coatings, and in the generation and transport of active material to the surface.

The L-type cathode contains a reservoir of active material sealed behind the porous plug of tungsten. The active material is generally a combination of  $\text{BaCO}_3$ ,  $\text{SrCO}_3$  and/or  $\text{CaCO}_3$ . The first thing that must be considered with this type of cathode is the conversion of the starting carbonates into the oxides. Rutledge and Rittner,<sup>19</sup> in their analysis of the L-type cathode, discuss the different reactions that can occur during the conversion of the carbonate to the oxide. The desired reaction is



Occurring below  $1,010^\circ\text{C}$ , this reaction usually takes considerable time to convert and outgas the structure. When attempts are made to reduce the conversion time by boosting the conversion temperature, a second reaction

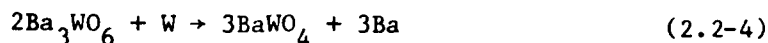


dominates the process. This reaction dominates according to Rutledge and Rittner at  $1,010^\circ\text{C}$  and above, and is totally undesirable, tying up the Ba and preventing its release.

Once the carbonates are all removed and the cathode is placed into operation, the chemical processes that occur are of the basic type



It is seen that the same barium tungstate products are formed in both the normal barium generating process and in the undesirable carbonate reaction. Finally, Rutledge and Rittner suggested the barium tungstate  $\text{Ba}_3\text{WO}_6$  reduces via the reaction

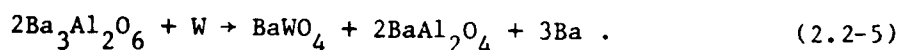


Rutledge and Rittner see the life limiting mechanism to be the onset of reaction 2.2-4 because, they suggest, this reaction releases an oxygen bearing poisoning agent. The evaporation rate of Ba coming from reaction 2.2-3 is about 1/2 the vaporation rate generated by reaction 2.2-4. This suggests that as long as reaction 2.2-3 predominates, the product  $\text{Ba}_3\text{WO}_6$  will build up. Both Ba and BaO should be evaporated from the cathode. Thermodynamic calculations show that the ratio of the vapor pressure of Ba to that of BaO should be 6.1 at 1,483 K. Experimentally, considerably more BaO is observed than is predicted from these calculations. The argument used to account for this difference is that Ba is oxidized as it passes through the matrix.

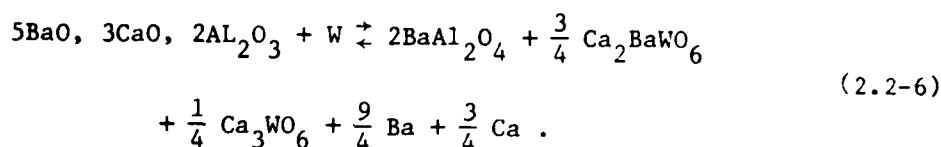
In the impregnated tungsten dispenser cathode, predominately the same reactions take place, with the exception of the carbonate reaction. In general, the carbonate reactions are processed out before the porous matrix is impregnated. The barium-calcium-aluminate is usually mixed from the barium calcium carbonates along with aluminum oxide powder then calcined by firing in a dry air atmosphere to reduce the carbonates to the oxide form. The impregnation of the porous matrix usually takes place at temperatures slightly above the melting point of the barium-calcium-aluminate mix. At those temperatures, the reactions that take place with the tungsten matrix proceed at high rates. This requires that

the impregnation process takes place as fast as possible spending a minimum of time at the high temperature.

The basic chemical reaction that is thought to occur during the operation of the impregnated dispenser cathode (neglecting calcium for this discussion) is



Rittner<sup>20</sup> et al measured by weight the total Ba produced from a tungsten matrix containing 5 BaO:2 Al<sub>2</sub>O<sub>3</sub>. The results suggested that reaction 2.2-5 with the product BaWO<sub>4</sub> predominates over reaction 2.2-3 with the product Ba<sub>3</sub>WO<sub>6</sub>. The full reaction equation for the B-type (5:3:2) is thought to take the form (cf Palluel and Schroff)<sup>21</sup> to be



The degree to which this reaction goes to completion depends upon many conditions that are not fully understood or fully controlled. The details of the complete ternary phase diagram play a very important part in the overall control of reaction 2.2-6. The ternary system is not well known. Wolten<sup>22</sup> compiled enough information from the literature to construct a slice through the ternary system at 1,250°C.

Does the aluminate mix of a given ternary composition remain at its original composition point after impregnation or do reactions with the matrix during the impregnation process change the impregnant composition? For example, at the impregnation temperature of 1,600 to 1,700°C, if Ca<sub>3</sub>WO<sub>6</sub> occurs at a higher

rate than  $\text{Ca}_3\text{BaWO}_6$ , the concentration of the calcium should change with depth into the matrix. These questions are as yet unanswered and could play an important part in the life and reliability of these devices.

As far as the bulk chemical reactions are concerned, we would not expect any differences for the M-type impregnated cathode, since the metal coating on the tungsten matrix is very thin (order of 1 micrometer). Except for very early in the cathode life, we would expect the same chemical reactions and rate to apply to the M-type as does for the B-type (assuming the same aluminate mix composition). The evaporation rate differences between the M- and B-type must be related to the effective binding of the Ba and BaO on the surface. The mixed metal matrix cathode, on the other hand, should be expected to provide different chemical reactions and reaction rates throughout its life, since the additive material (e.g., Ir, Os or Re) is dispersed throughout the matrix and must enter into the chemical reactions. The evaporation rate of Ba and BaO from the mixed metal cathode will be controlled by both the reaction rate and the change in binding energy of the atoms to the emitter surface. Since the mixed metal cathode is relatively new, there is very little information on this topic either experimentally or theoretically.

### 2.3 TRANSPORT OF THE ACTIVE MATERIAL TO THE EMITTER SURFACE

In the dispenser cathode, there are two possible mechanisms by which the active material can be transported to the emitter surface. The first is Knudsen flow, which describes the flow of a gas when the mean free path of the gas is large compared to the size of the confining vessel - in this case, the pores of the tungsten plug. The second possible mechanism is surface migration of the active material along the interior walls of the pores until the emitter surface is reached. Rutledge and Rittner<sup>23</sup> suggest that because of the very good coverage of barium that is observed for the L-type cathode, there would be very little concentration gradient of surface atoms through the porous plug, thus suggesting that Knudsen flow dominates the transport processes. The Knudsen flow through a porous plug is given by Rutledge and Rittner by the relationship

$$\frac{dm}{dt} = - \frac{\alpha A M^{1/2}}{N(2\pi m k T)^{1/2}} P, \quad (2.3-1)$$

where  $m$  is the mass flow through the plug,  $P$  is the active material pressure,  $A$  is the area of the sample,  $N$  is Avogadro's number,  $M$  is the molecular weight, and  $\alpha$  was determined experimentally for different porosities. In general, the transmission coefficient,  $\alpha$ , increases with increasing porosity as expected. Using the experimentally determined transmission coefficient and vapor pressure data for barium in the cavity, the evaporation rate  $dm/dt$  can be calculated and compared to the measured evaporation rate data. The results found by Rutledge and Rittner correlated exceptionally well, confirming for them that Knudsen flow dominates the transport process for the L-type cathode at least.

Brodie and Jenkin<sup>24</sup>, in their work on the evaporation rate of Ba from the L-type cathode, conclude that there are two competing mechanisms controlling the transport of barium. The rate of reaction controls the evaporation when the plug is very porous, according to this work. As the porosity decreases, Knudsen flow dominates the transport. These two mechanisms become even more important in impregnated dispenser cathodes; the generation of active material, barium in our case, is more strongly coupled to the transport of the material. Rittner, Rutledge and Ahlert<sup>25</sup> suggest that Knudsen flow dominates the transport, leading them to envision a "receding surface" or reaction zone moving deeper into the porous matrix with time. The Knudsen flow model that they use is

$$\frac{dm}{dt} = K_1 \left( \frac{r}{L} \right) \sqrt{\frac{M}{T}} P, \quad (2.3-2)$$

where  $r$  is the effective radius of the pores and  $L$  the effective pore length which becomes clogged with time. In equation (2.3-2),  $K_1$  is a constant,  $P$  the

vapor pressure of Ba, M the molecular weight of the evaporant gas, and T the temperature of the cathode.

The receding surface of the reaction zone is introduced into the simple model by assuming that the length of the pores (L) is proportional to the amount of mass evaporated up to time t i.e.,

$$m = K_2 L \quad (2.3-3)$$

where  $K_2$  is a proportionally constant. Combining Eqs. (2.3-2) and (2.3-3), it can easily be shown that

$$\frac{dm}{dt} = \sqrt{\frac{K_3}{2t}} \quad (2.3-4)$$

The expected boundary conditions were not discussed by Rittner et al. Clearly we expect  $dm/dt$  to be finite when  $t = 0$ . Eq. (2.3-4) is shown to be consistent with evaporation experiments. Experiments of evaporation rate with pellet thickness suggested to Brodie and Jenkin<sup>24</sup> that the reaction generating barium is taking place uniformly throughout the impregnated matrix. They suggest that barium leaves the reaction sites freely, and migrate along the interface between the impregnate and the tungsten powder walls. They suggest that this migration, and not Knudsen flow, controls the transport of the barium. Brodie and Jenkin do not discuss the time dependence of the evaporation rate. In fact, their measurements were made only at the beginning of life. The time dependence of the mechanism suggested by Brodie and Jenkin could, however, yield a functional behavior as is observed, if the products of the reactions are relatively immobile. Rittner<sup>26</sup> solved the appropriate diffusion equation in this case for the interface layer growth of the oxide cathode and showed that an interface layer would grow with a thickness that would depend on time as



$$a = a_0 \sqrt{1 + \beta t} \quad (2.3-5)$$

where  $\beta$  depends on the diffusion coefficient and the surface concentration. The main component of the chemical reaction would then have to diffuse through this growing layer before reacting. Thus, the pressure and, in turn, the evolved mass would depend upon  $1/a$ , and the same functional form in time is observed.

Palluel and Shroff<sup>27</sup> recently reported observing a gradient of barium and calcium on fractured pellets using electron microprobe analysis. The depletion depth of barium versus operating hours has a square root of time dependence. The depletion depth of calcium has a  $t^{-1/3}$  dependence which cannot be easily explained. The observation of the depletion depth or a concentration gradient across the porous pellet in the impregnated cathode case points to Knudsen flow dominance depending upon the details of the matrix and impregnate system. Clearly, if the barium freed by chemical reaction with the walls of the pores is not readily removed, the concentration of barium will build up driving the reaction in the reverse direction and causing no net effect. In that case, there will be a net effect only near the surface where the pressure of barium drops sufficiently for the reaction to proceed in the forward direction. This narrow volume near the surface will then become depleted first, causing the effect of a receding surface as envisioned for the Knudsen flow arguments. The discrepancy between the two experiments might very well be in the difficulty of controlling the porous matrix and the impregnation process.

#### 2.4 SURFACE CHEMISTRY AND PHYSICS

Once the active material reaches the emitter surface, the processes that are responsible for the lowering of the work function begin. The exact nature of the surface dipoles and the interaction with the substrate surface has been subject of investigation for many years. Until recently, the experimental evidence has been deductive (cf Wagener<sup>28</sup> for a discussion of the earlier

works), with the advent of surface analysis tools the atomic nature of the surface is more directly observable. Many of the deductive results of earlier experiments are being shown to be true with these new tools.

There is much evidence to support the hypothesis that the surface dipoles for the tungsten dispenser cathode are barium on oxygen on tungsten. There remains much not understood about the precise nature of the surface dipoles on an atomic level. The role of calcium, for example, is not thoroughly understood. Ba forms a dipole with oxygen on tungsten, but the nature of the bonding and sharing of electrons between the Ba, the oxygen and the substrate metal remains unknown. Green<sup>29</sup> has recently speculated on the nature of the bonds. There is, however, overwhelming direct and indirect evidence that barium and oxygen are in a one-to-one correspondence on the surface. Springer and Haas<sup>30</sup> have observed, using AES, barium to oxygen ratio that is one to one on the active cathode if corrections are made for the escape depth of the Auger electrons with barium over oxygen. Maloney et al<sup>31</sup> also observed the one to one correspondence of barium to oxygen on the tungsten surface of a fully activated cathode. The same one to one correspondence in a fully activated cathode is observed by Green.<sup>32</sup> Eng<sup>33</sup> has made similar observations using AES. There seems little doubt that the dipole responsible for the emission properties of the tungsten barium aluminate dispenser cathode is formed by barium on oxygen on tungsten. These observations, however, are not without discrepancy. Jones et al<sup>34</sup> observed with AES a considerably different Ba/O ratio of about 0.3 for various dispenser types (3:1:1), (4:1:1) and (5:3:2) for tungsten surfaces as well as for typical M-type dispenser cathodes.

It is well known that considerable improvements in the emission levels can be obtained if calcium is added to the barium aluminate mixture. The exact nature of the calcium effect is not known. Early speculations (cf Brodie and Jenkins<sup>35</sup>) suggest that the addition of calcium causes the pores to become more emissive, effectively increasing the emitting area. Other suggestions are that calcium regulates the release of barium in the pores.

It is curious that calcium is not observed on the emitter surface of a well activated dispenser cathode. Attempts to find calcium even in the pores have

failed. The disappearance of calcium upon activation has been observed by numerous investigators. Among those reporting this effect are Springer and Haas<sup>36</sup> using a 0.5 mm beam size AES, Sickafus<sup>37</sup> et al using a 0.1 micrometer beam size AES system, and Jones et al<sup>38</sup> and Forman.<sup>39</sup>

Sickafus et al have specifically searched for the missing calcium, using their relatively small beam size AES system to look into the pores, and have reported finding no calcium. They do find calcium deep in the matrix when the porous plug is fractured (the case reported was for a 22,000 hour cathode). This observation suggests that a gradient of calcium should be observed across a fractured cathode that has been used for some time. Palluel and Shroff<sup>40</sup> have observed a gradient for both barium and calcium.

#### REFERENCE LIST

1. Lemmens, H. J., U.S. Patent 2,543,728, 1948.
2. Falce, L. R., Tri Service Cathode Workshop, 1978.
3. Hughes, R. C., U.S. Patent 2,700,118, 1951.
4. Levi, R. J., Appl. Phys., 26, 639, 1955.
5. Levi, R., op cit, 1955.
6. Zalm, P.; Van Strutem, A. J. A., Phillips Tech. Rev, 27, p. 69, 1966.
7. Green, M., RADC TR-81-211 Report, 1981.
8. Tuck, R., Jr. Services Cathode Workshop, 1979.
9. Falce, L. R., Tri Services Cathode Workshop, 1978.
10. Beck, A. H. W.; Ahmed H., J. Elect. Cont., 14, p. 623, 1963.
11. Forman, R., J. Appl. Physics 47, p. 5272, 1976.  
Forman, R., IEEE Trans. Elec. Dev., 24, p. 56, 1977.  
Forman, R., Appl. Surf. Sci., 2, p. 258, 1979.
12. Green, M., op cit, 1981.
13. Forman, R., op cit, 1979.
14. Rittner, J. Appl. Physics, 48, p. 4344, 1977.
15. Longo, R. T., IEDM, p. 152, 1978.
16. Pierce, J. R., Theory and Design of Electron Beams, D. Van Nostrand Co., Inc., 1954.

17. Forman, R., IEEE Trans. Elect. Dev., 26, p. 1567, 1979.
18. Palluel, P. and Shroff, A., J. Appl. Physics, 51, p. 2894, 1979.
19. Rutledge, W. C. and Rittner, E. S., J. Appl. Physics, 28, pp. 157, 167, 1957.
20. Rittner, E. S., J. Appl Physics, 28, p. 1468, 1957.
21. Palluel, P. and Shroff, A., opt cit, 1979.
22. Wolten, G. M. Aerospace Corp., Report SD-TR-80-67.
23. Rutledge, W. C. and Rittner, E. S., op cit, 1957.
24. Brodie, I. and Jenkin, R. O., Brit. J. Appl. Physics, 8, p. 27, 1957.  
Brodie, I. and Jenkin, J. Electr., p. 457, 1956.  
Brodie, I. and Jenkin, J. Electr., p. 33, 1957.
25. Rittner, E. S. and Rutledge, W. C. Alert, J. Appl. Physics, 28, p. 1468, 1957.
26. Rittner, F. S., Philips, Res. Rep., 8, p. 184, 1953.
27. Palluel, P. and Shroff, A., op cit, 1980.
28. Wagener, S., The Oxide Coated Cathode, Vols. I and II, Chapman and Hall Ltd., 1951.
29. Green, M., op cit, 1981.
30. Springer, R. W. and Haas, T. W., J. Appl. Physics, 45, p. 5260, 1974.
31. Maloney, E. D., MSN, 119, 1979.

32. Green, M., op cit, 1981.
33. Eng, G., Rep. SD-TR-81-35, 1981.
34. Jones, D., Appl. Surf Sci., 2, p. 232, 1979.
35. Brodie, I. and Jenkin, R. O., op cit, 1957.
36. Springer, R. W. and Haas, G. A., J. Appl. Physics, 45, p. 5260, 1974.
37. Sickafus, E. N., Appl. Surf. Sci., 2, p. 213, 1979.
38. Jones, D., op cit, 1979.
39. Forman, R., J. Appl. Physics, 47, p. 5272, 1976.
40. Palluel, P. and Shroff, A., op cit, 1980.

### 3.0 FACILITIES AND EQUIPMENT

#### 3.1 HEDD DISPENSER CATHODE FABRICATION FACILITIES

HEDD has a modern, well equipped, dispenser cathodes manufacturing facility to fabricate dispenser cathodes from the raw materials. The heart of the facility is the system of three major furnaces, dedicated for cathode fabrication, shown in Figure 3.1-1. At the left in Figure 3.1-1 is the hydrogen fast cycle impregnation furnace. In the center is a high temperature vacuum furnace used to remove copper from the tungsten billet.

At the right, in Figure 3.1-1, an air furnace is shown. This furnace is used to prepare the active barium-calcium-aluminates from the barium, carbonates, calcium carbonate and aluminum oxide. Figure 3.1-2 is a view of the cathode laboratory showing inspection, analysis and assembly areas.

Tungsten billets, prepared from tungsten powder using standard techniques are sintered and copper infiltrated in the furnaces shown in Figure 3.1-3 and Figure 3.1-4, respectively. Figure 3.1-3 is a high temperature hydrogen furnace capable of 3,000°C. Figure 3.1-4 is a hydrogen tube furnace used to infiltrate the billets with copper.

An isostatic press is used to press tungsten powders to form the tungsten billets, and various other support equipment which are not shown make up the complete cathode fabrication facility. Part of this equipment includes sputtering facilities used to deposit the osmium/ruthenium films required in the fabrication of "M" type cathodes.

#### 3.2 EMISSION TESTING PROCESS EVALUATION TESTER (PET)

The Process Evaluation Tester (PET) is a multiple cathode test vehicle which has been designed to yield relatively rapid information about the emission properties of cathodes.

Figure 3.2-1 is an overall assembly drawing of the PET system. The cathode coupons are inserted in the fixture on the left and then the entire multi-cathode test fixture is inserted into the vacuum system. Figure 3.2-2 is

E1476



Figure 3.1-1 View of the cathode laboratory showing the hydrogen furnace, vacuum furnace and air furnace.



E1026



Figure 3.1-2 View of the cathode laboratory showing inspection, analysis and assembly areas.

E1477

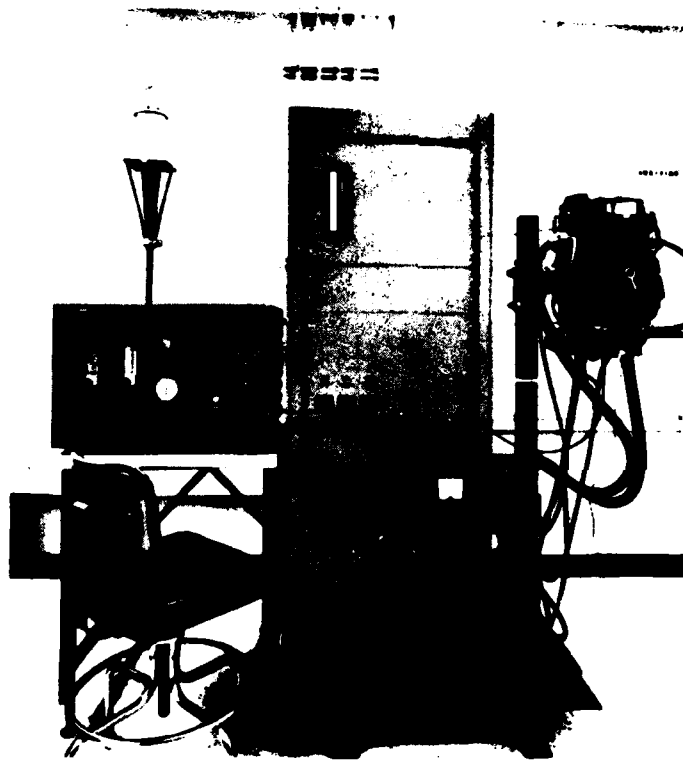


Figure 3.1-3 High temperature hydrogen furnace  
for sintering tungsten and aluminum  
oxide potting material.

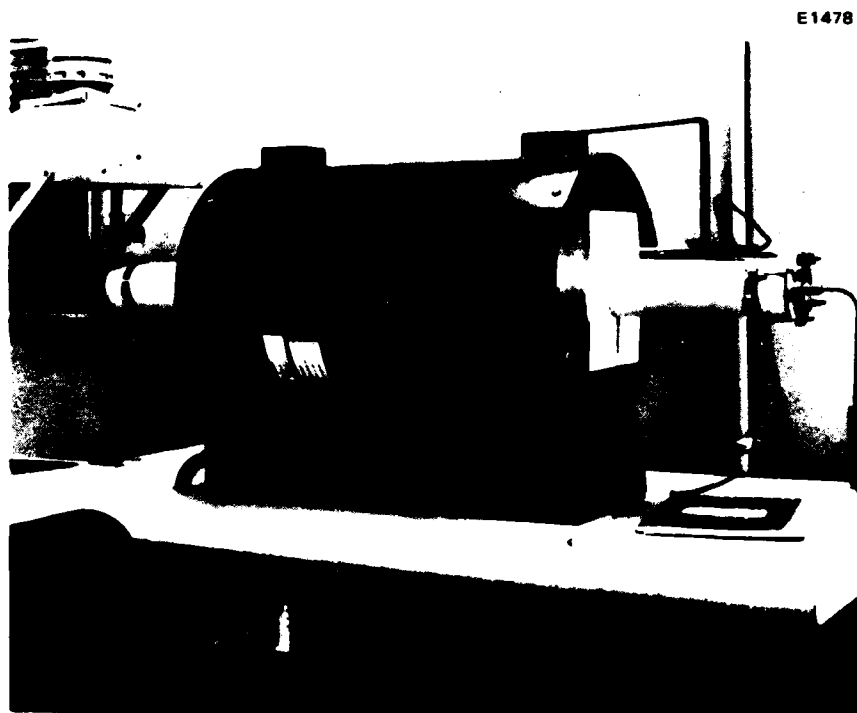


Figure 3.1-4 Hydrogen furnace for infiltrating the tungsten billets with copper.

G5831

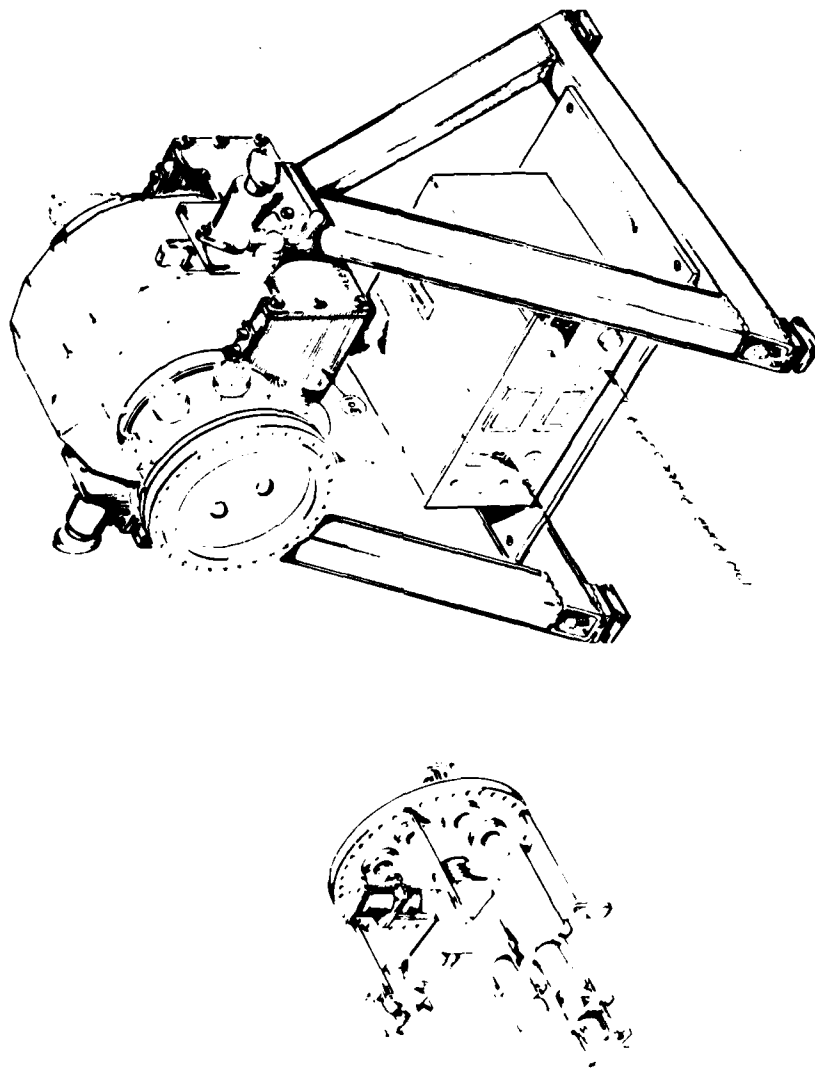


Figure 3.2-1 Schematic drawing of the PET test equipment.

a schematic drawing of the interface of the multicathode test fixture with a HP 3052A data acquisition system. The computer will control all operation of the PET, acquire the data on each cathode sequentially, process the data, and present the data in a usable form, both printed and plotted.

Figure 3.2-3 is a photograph of the complete system. On the left is the computer and data acquisition system with associated electronics. At the right is the mass spectrometer electronics. In the center is the vacuum system, which has 3-axis micromanipulator capability for the anode and the mass spectrometer head at the top. Figure 3.2-4 is a photograph of the inside of the vacuum system. This photograph shows only one cathode assembly; however, stations for five (5) others can be seen. The cathode and anode in the PET form a parallel plate diode.

The temperature of the cathodes was measured optically through a sapphire window in the face plate. There is a blackbody hole in the side of the cathode coupon to reduce the effects of emissivity. The temperature accuracy is near 0.5%, after window corrections are taken into account.

### 3.3 BARIUM EVAPORATION MEASUREMENTS

Barium evaporation rate measurements were measured in a separate vacuum system. These measurements are made by exposing a hot tantalum wire to the barium compounds streaming through an aperture from the cathode and measuring the emission current from the wire. This wire emission current rises to a peak as the barium coating passes through a monolayer.

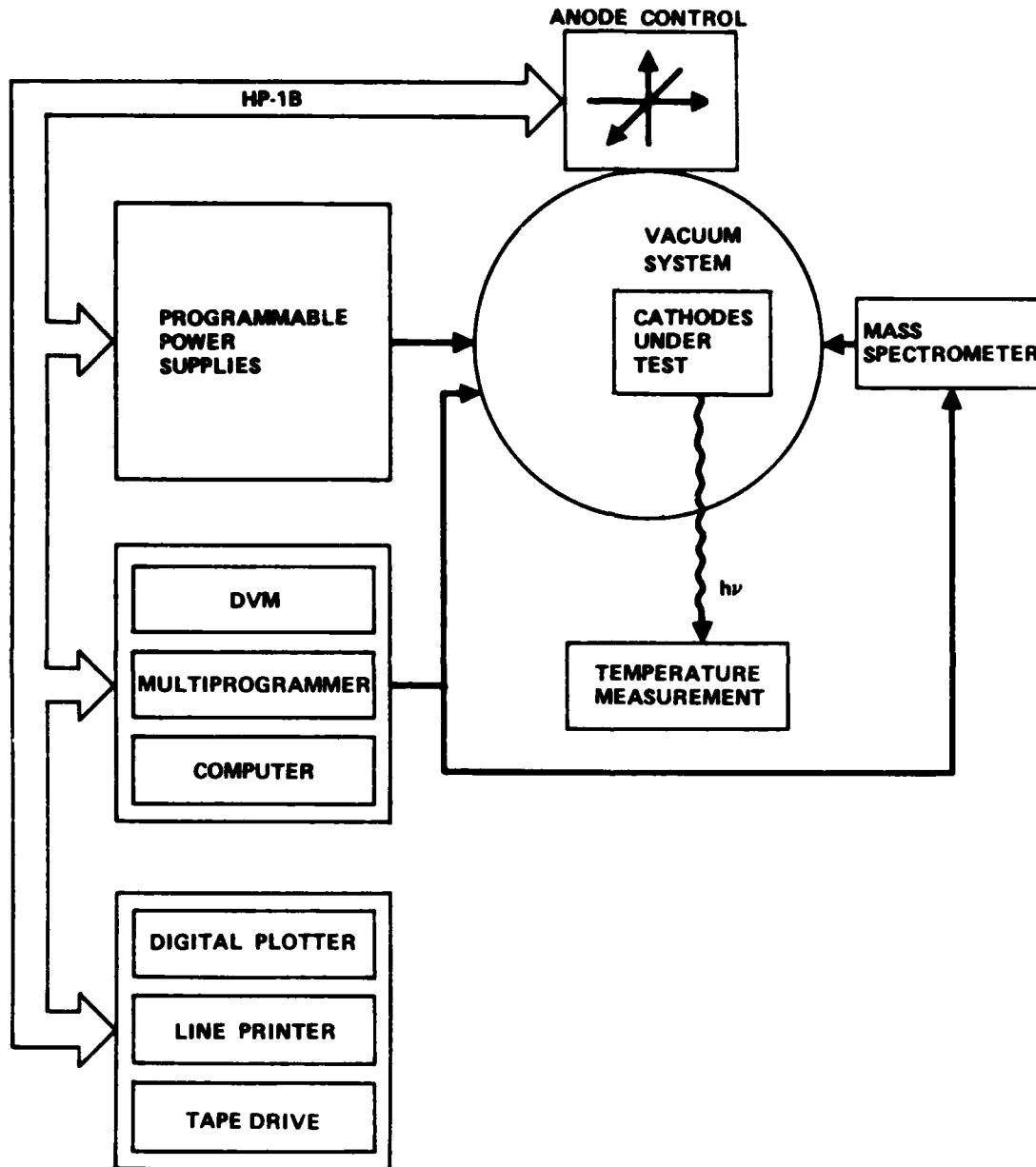


Figure 3.2-2 Schematic of the PET with data acquisition system.



Figure 3.2-3 Photograph of the Process Evaluation Tester (PET). The vacuum assembly is shown in the center with associated pump supplies below. The unit attached to the top of the vacuum system is a quadrupole mass spectrometer. The two racks to the left of the vacuum system are the HP 3052A data acquisition system which contains the computer, A to D converters and associated power supplies, scanner and DVM integral with the computer is a printer (top of left rack) and a plotter (center left rack). The rack on the right contains the electronics for the quadrupole mass spectrometer.

E2600

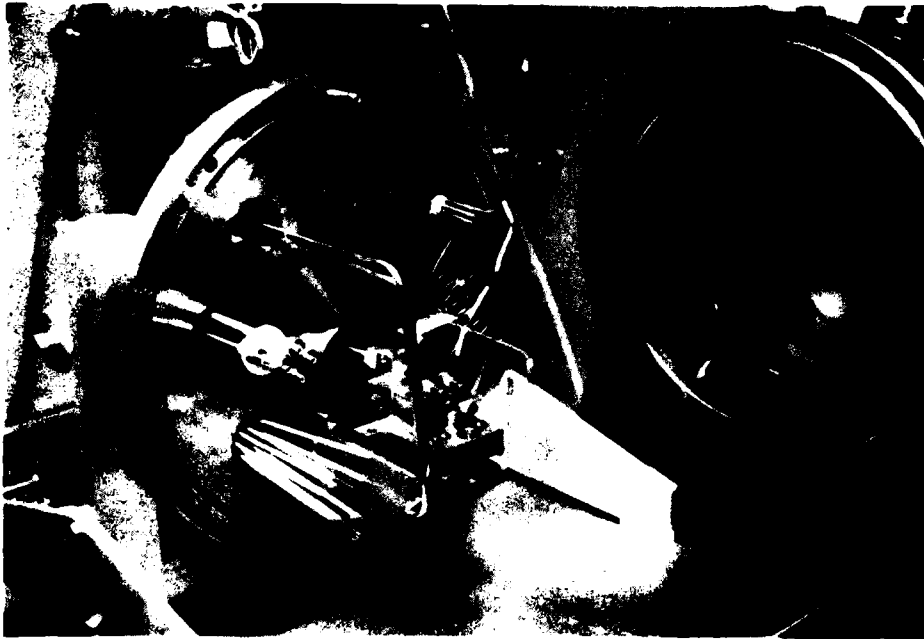


Figure 3.2-4 This photograph shows the inside of the PET vacuum system. Only one cathode assembly is shown in the photograph.



#### 4.0 MATERIALS AND CATHODE MANUFACTURING

All of the materials used in this program, with the exception of the Osmium-Ruthenium sputter target, were purchased specifically for this program. The cathodes that were manufactured, tested and shipped to Wright-Patterson were all made from these special materials.

##### 4.1 TUNGSTEN POWDERS

The tungsten powders were purchased in two lots from General Electric. Lot No. U4.5-8100D was a 25 kgm lot of powder centered on 4.5 micrometer particle size. Lot No. U9.5-7833D was also a 25 kgm lot of powder with particle size centered on 9.5 micrometers. The tungsten powders were analyzed by General Electric and are reported in Table 4.1-1. The raw powders as received by Hughes were reanalyzed chemically. The results of those tests are shown in Table 4.1-2. Figure 4.1-1a and b are Scanning Electron photomicrographs (SEM) of the as received powders. The as received particle distributions are shown in Figure 4.1-2 and 4.1-3.

The tungsten powder lots were then sent to Vortex for particle size classification. Table 4.1-3 shows the results of this process. In order to assure cleanliness of the particle separator a 3 kgm lot of tungsten powder was supplied as a clean up lot. This lot (which was not part of the material purchased for this program) was run through the separator before the program lots were run.

TABLE 4.1-1

## CHEMICAL ANALYSIS BY GENERAL ELECTRIC

Element*	(ppm) Lot # U4.5	(ppm) Lot # U9.5
Mo	87	410
Fe	31	18
Cr	9	3
Ni	17	6
Al	3	-
Sn	3	-
O	419	176

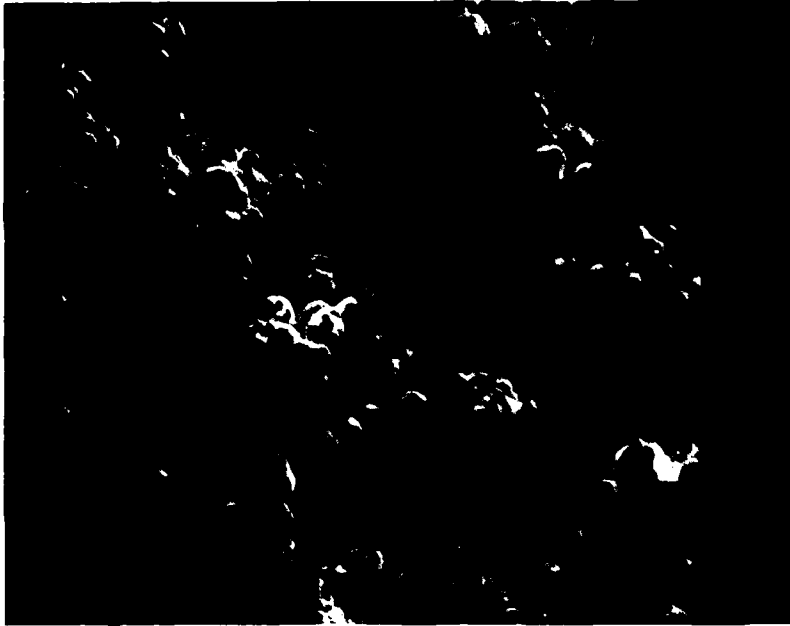
\*Other elements tested for but not found were Ca, Si, Su, Mn, Mg, C

TABLE 4.1-2  
CHEMICAL TEST OF TUNGSTEN POWDER

Element <sup>(a)</sup>	Lot # U4.5 Weight Percent	Lot # U9.5 Weight Percent
Mo	-	.01 ± .001
Fe	.011 ± .001	.01 ± .001
Ca	.001	.002
C	.002 ± .001	.003 ± .001

(a) Other elements tested for but not found were Al, Sb, As, Ba, Be, Bi, B, Cd, Cr, Co, Cu, Ga, Ge, In, Pb, Mg, Mn, Hg, Ni, P, Si, Ag, Sr, Sn, Ti, V, Zn, Zr, Na, Cs, Li, K, Rb

E4351



(a)



(b)

Figure 4.1-1 1500x SEM photomicrographs of (a) U4.5 and (b) U9.5 tungsten powder before classification.

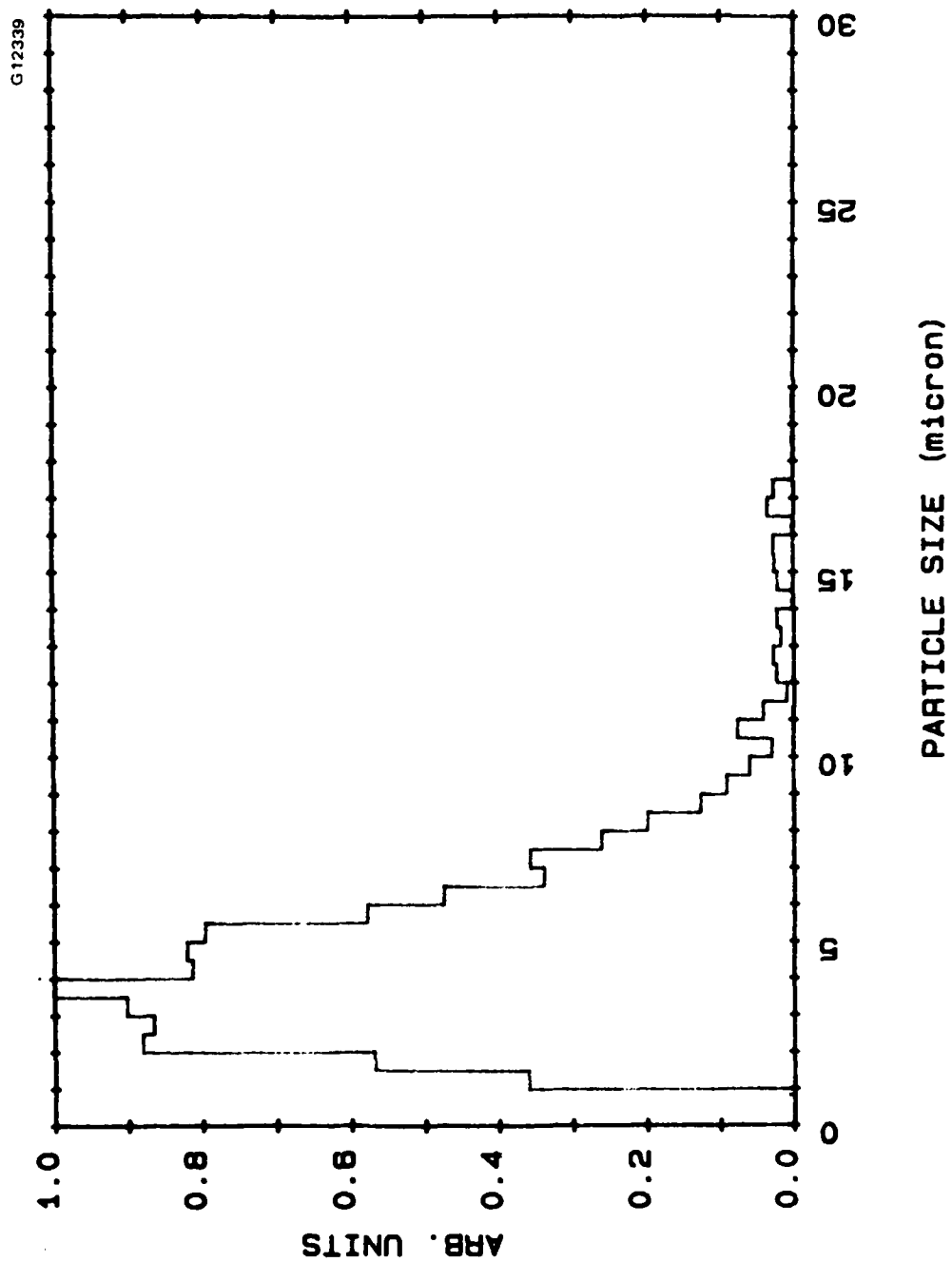


Figure 4.1-2 Distribution of unclassified tungsten powder U4.5.

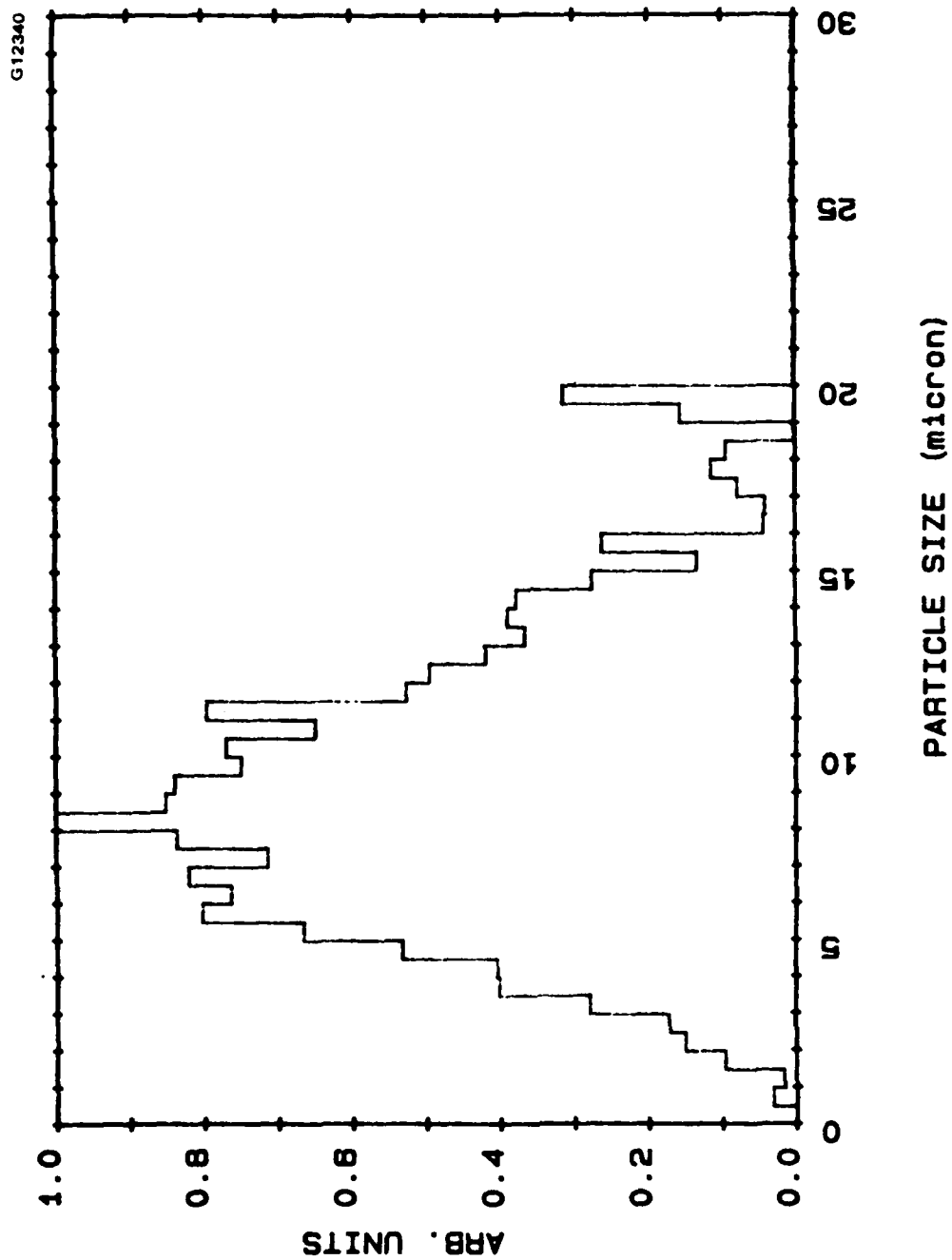


Figure 4.1-3 Distribution of unclassified tungsten powder U9.5.

TABLE 4.1-3  
TUNGSTEN PARTICLE SIZE CLASSIFICATION

Lot #	Partial Size Range (micron)	% of Total Material
U4.5	0-4	51.5
	4-6	32
	>6	16.5
U9.5	0-10	43
	10-12	27
	>12	30

Figure 4.1-4a and b are Scanning Electron photomicrographs (SEM) of the classified powders. The corresponding distribution for the classified powders are shown in Figures 4.1-5 and 4.1-6. Table 4.1-4 gives the identification of the powders that will be used throughout the remainder of this report. The unclassified powders were actually remixed in the percentages stated in Table 4.1-3.



(a)



(b)

Figure 4.1-4 1500x SEM photomicrographs of the classified powders. (a) is the 11 micron classified powder and (b) is the 5 micron classified powder.



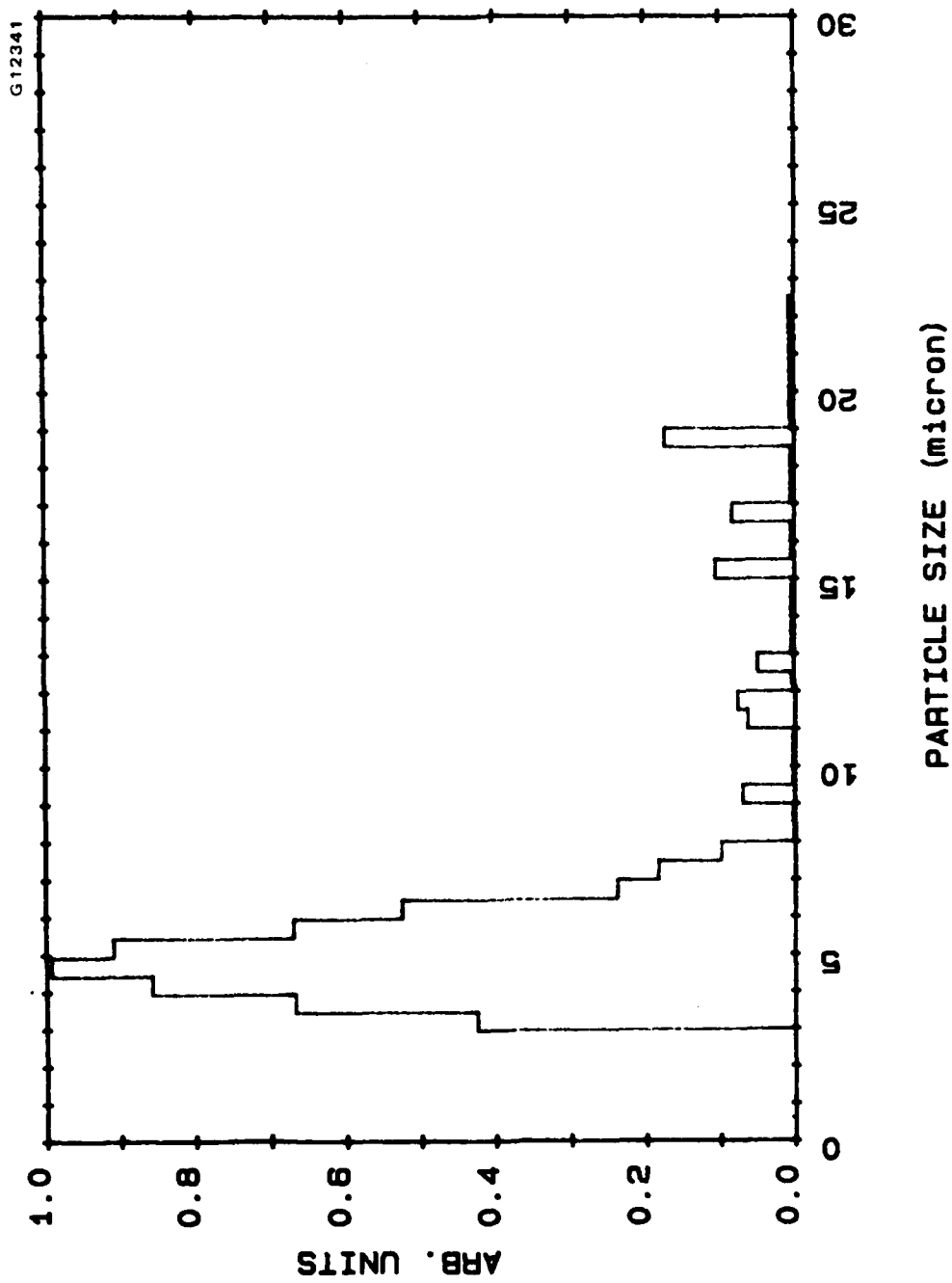


Figure 4.1-5 Distribution of classified tungsten powder, 5 micron.

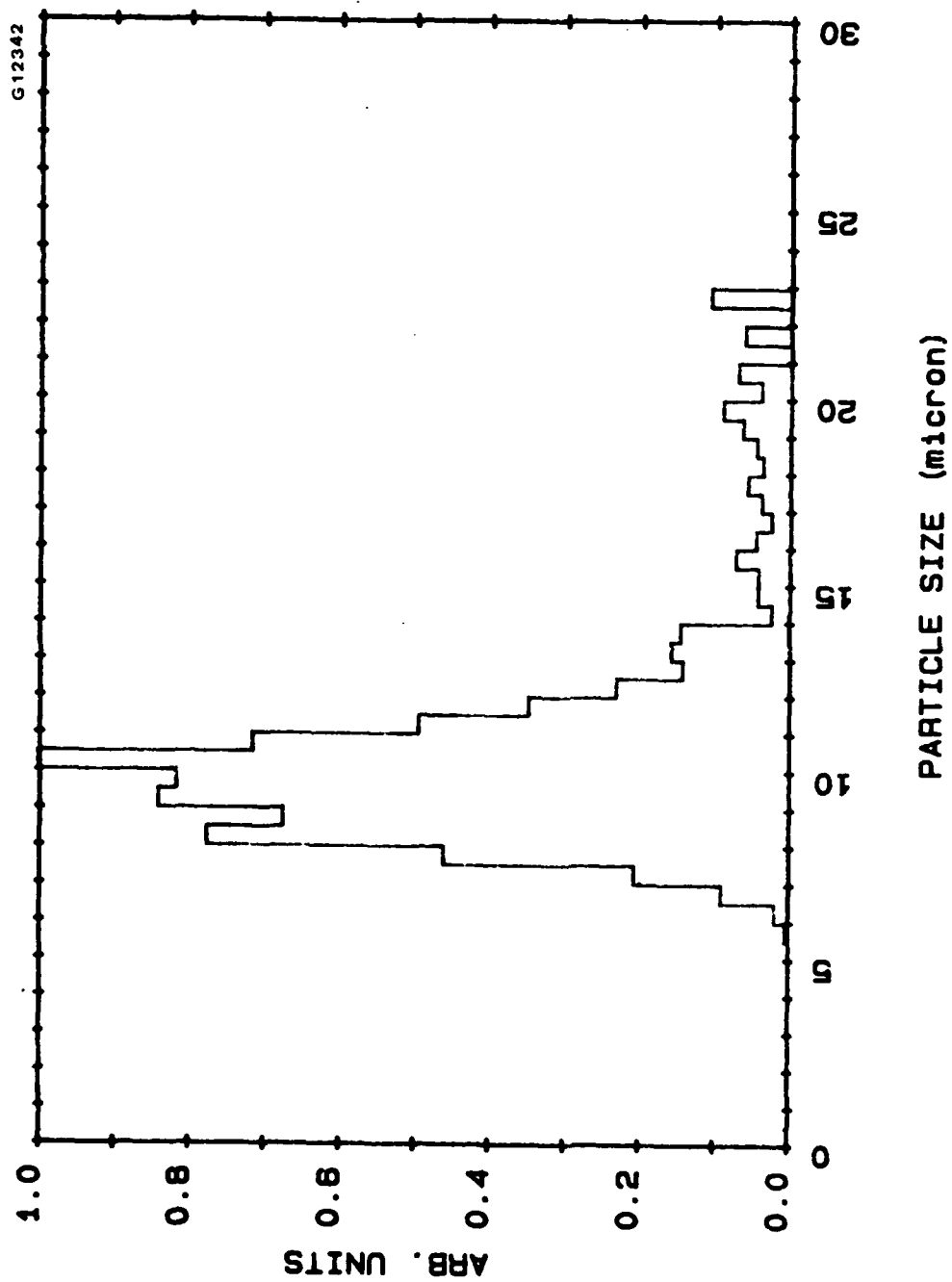


Figure 4.1-6 Distribution of classified tungsten powder, 11 micron.

TABLE 4.1-4

## POWDER IDENTIFICATION

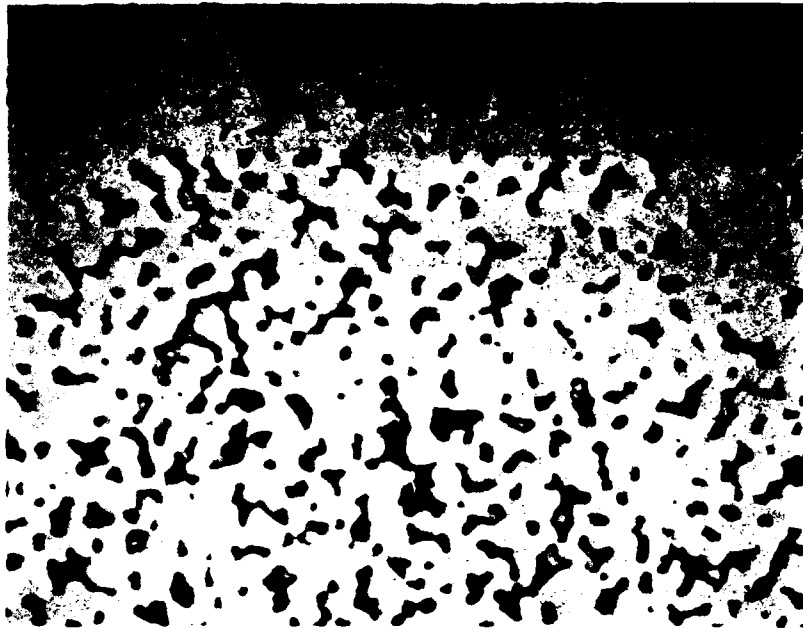
Classified	Unclassified
5	5U
11	11U

#### 4.2 TUNGSTEN BILLETS

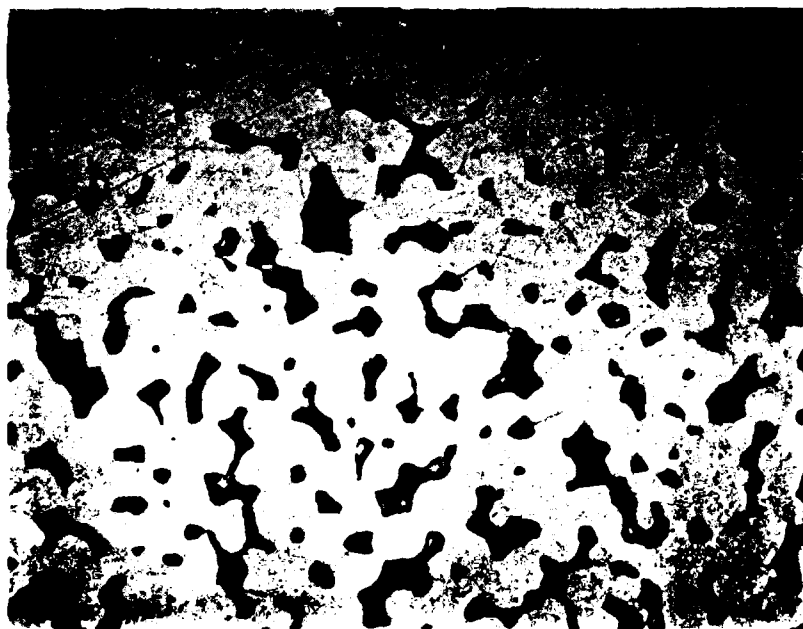
After the tungsten powders were prepared as discussed in section 4.1, the powders were isostatically pressed and sintered in a  $H_2$  atmosphere to a theoretical density of 80 plus or minus 2%. Table 4.2-1 gives the billet identifications the powder used and the billet density. The billets were then infiltrated with copper under a  $H_2$  atmosphere and machined into rods. Cross sections of the 5 and 11 billets are shown in Figure 4.2-1. These billets were then machined into the cathode which will be discussed in a later section.

TABLE 4.2-1  
BILLETS G.E. POWER

Billet Ident	Powder	Density
9C-62	5	$81.2 \pm 0.8$
10C-63	11	$79.4 \pm .3$
9A-65	5U	79.7
10A-64	11U	81.2



(a)



(b)

Figure 4.2-1 1000x photomicrographs of the (a) 5 micron billet and the (b) 11 micron billet.

#### 4.3 ALUMINATES AND ALUMINATE MATERIAL

The aluminate materials ( $\text{Al}_2\text{O}_3$ ,  $\text{BaCO}_3$  and  $\text{CaCO}_3$ ) were obtained from Atomergic Chemicals. The Atomergic material specification is given in Table 4.3.1.

The aluminate materials were blended into two lots, lot No. 12 with a (5:3:2) molar ratio of ( $\text{BaO}:\text{CaO}:\text{Al}_2\text{O}_3$ ) and lot No. 13 with (4:1:1) molar ratio. Table 4.3-2 gives the details of the blended powders before calcining. Samples of each of the individual powders (i.e. before mixing and blending) were sent to Wright-Patterson for analysis.

Atomergic could only supply the  $\text{BaCO}_3$  and the  $\text{CaCO}_3$  in powder sizes of -100 mesh. Previous experience with large grain size material (i.e.  $\text{Al}_2\text{O}_3$ ) indicated a problem with thorough reaction into the final aluminate.

At our request, Atomergic ground the  $\text{BaCO}_3$  and the  $\text{CaCO}_3$  to -325 mesh using a  $\text{Al}_2\text{O}_3$  mortar and pestle. We dropped the Al impurity specification so that this grinding could be accomplished. Atomergic indicated that they could hold all of the other impurity at their specified limit. The purity was not measured by Atomergic or by us due to the small quantities involved. Samples were, however, sent to Wright-Patterson, per the contract requirements, for chemical analysis. The results of analysis by B. Lamertine indicated that we had an unexpected sulfur contamination, which entered from the  $\text{BaCO}_3$ .

Sulfur impurity was the basic reason we chose not to use Linde B ( $\text{Al}_2\text{O}_3$ ) material (which is an industry standard). After becoming aware of the contamination, we began an independent chemical analysis on the small amount of mixed powder we had left. Table 4.3-3 shows the results of a LECO analysis on lots No. 12 and No. 13 of this program. We added for comparison other lots used in our manufacturing facility. The concentration of sulfur in the aluminate mix (lots 12 and 13) is a factor of 2 to 3 larger than expected. However, it is about a factor of 2 smaller than would be obtained with the standardly used material (compare lots #12 and #13 with lots #9 and #14 in Table 4.3-3). The major difference is the source of the contamination in the usual case (e.g. lot 9) sulfur enters from the  $\text{Al}_2\text{O}_3$ . In the case of lot 12 and 13 it enters from the  $\text{BaCO}_3$ . Whether this makes any difference or not is uncertain, however workers<sup>(1)</sup> have reported two forms of sulfur, electrically active and electrically neutral.

TABLE 4.3-1

## BASIC ALLUMINATE COMPONENT RAW MATERIALS

	Atomergic Specification	Chemical Lot #	Amount Obtained
$\text{Al}_2\text{O}_3$	99.995%	E5094	1 lbs
$\text{Ba CO}_3$	99.999%	F4151	100 gm
$\text{Ca CO}_3$	99.999%	F4152	100 gm

TABLE 4.3-2

## ALUMINATE MIXES

Aluminate Lot #	Type Molar Ratios*	Chemicals	Chemical Lots	Weights gm
12	(5:3:2)	$\text{Al}_2\text{O}_3$	E5094	6.85
		$\text{BaCO}_3$	F4151	33.10
		$\text{CaCO}_3$	F4152	10.05
13	(4:1:1)	$\text{Al}_2\text{O}_3$	E5094	5.15
		$\text{BaCO}_3$	F4151	39.80
		$\text{CaCO}_3$	F4152	5.05

\*(BaO: CaO:  $\text{Al}_2\text{O}_3$ )

TABLE 4.3-3

## SULFUR ANALYSIS ON ALUMINATE LOTS

Lot #	Sulfur % by Weight	Remarks
#12	0.016 ± .003	(5:3:2) (This program) before calcining
#13	0.024 ± .003	(4:1:1) (This program) before calcining
#9	0.037 ± .003	Space qualified material using Linde-B ( $\text{Al}_2\text{O}_3$ ) before calcining
#9	0.042 ± .003	After calcining
#14	0.009 ± .001	Production high purity before calcining
#14	<0.002	After calcining



#### 4.4 M-COATING

The experimental matrix of samples contains both standard tungsten dispenser cathodes and coated tungsten dispenser cathodes. The cathodes that were coated had a  $1\mu\text{Os}(80\%):\text{Ru}(20\%)$  coating sputtered over the emitter surface of the completely finished tungsten dispenser cathode. Typical coatings are shown in cross section in Figure 4.4-1. The tolerance on the coating thickness is estimated to be plus or minus  $.25\mu$ .

The Os(80%):Ru(20%) sputter target is the standard manufacturing target. (A new target was not purchased for this program.) The target is 2 inches in diameter and the sputter process uses argon in a 4 inch cold trapped diffusion pump system.

All of the M-coated cathodes were processed via the procedure described in the Nasa Philips report<sup>1</sup>.

Figure 4.4-2 shows a SEM of the emitter surface of a typical coated and uncoated cathode manufactured for this program.

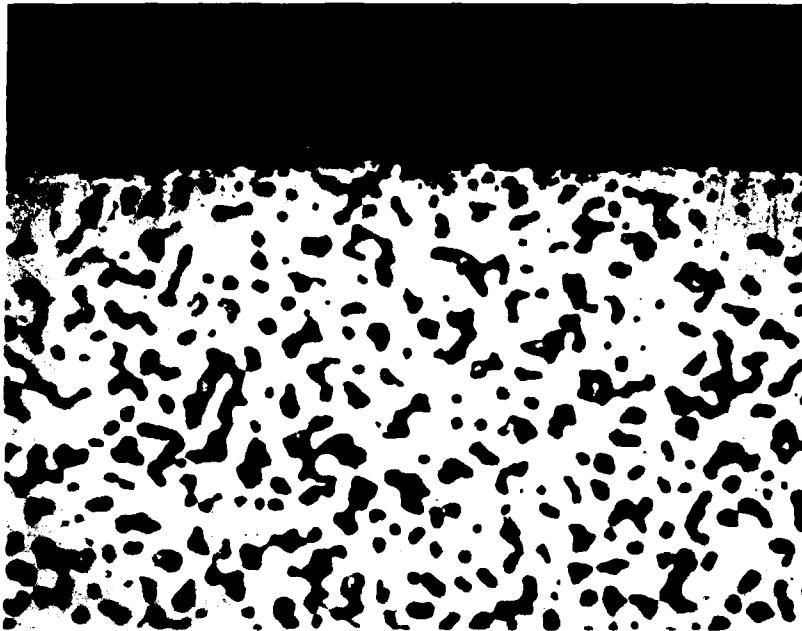
#### 4.5 SAMPLE PREPARATION

Since the intent is to determine the variations of work function on the process parameters, it was decided to prepare the emitter surface by a deionized  $\text{H}_2\text{O}$  bath rather than the more usual polishing. The use of  $\text{H}_2\text{O}$  to etch off the excess aluminate that remains after the impregnation step has no ill effects on the cathode provided the initial operation brings the cathode up through  $500^\circ\text{C}$  slowly and allows all the adsorbed water to deabsorb and be pumped from the test vehicle.

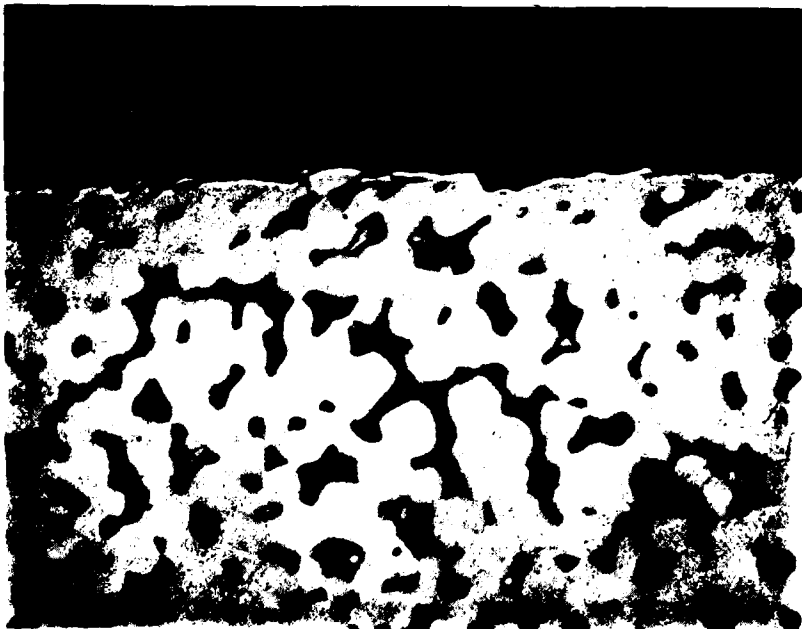
The purpose for using water as a surface cleaning procedure is to avoid the smearing of the surface associated with polishing. It is well known that the effects of polishing are slowly removed by thermal effects but requires

---

<sup>1</sup> Philips/Nasa Report, C21219, May 1977, Manufacture of M-type impregnated cathodes.



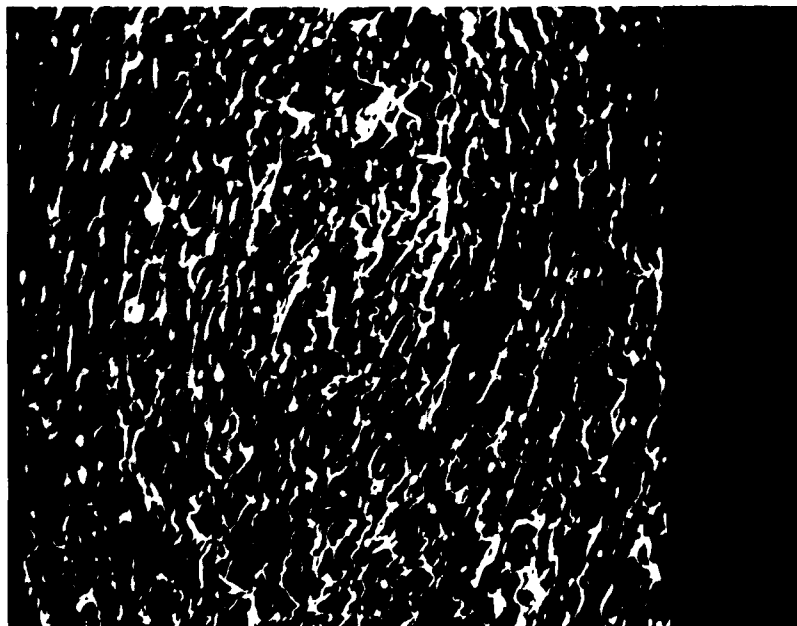
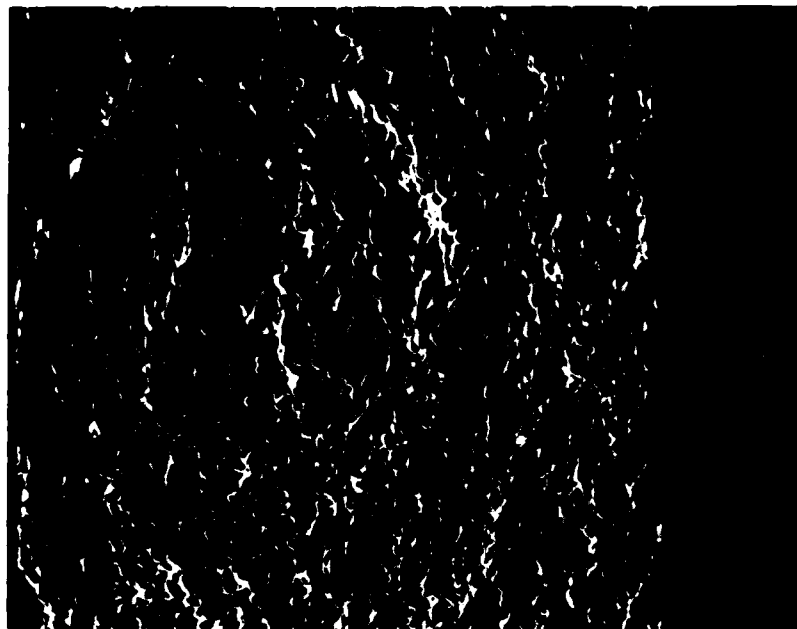
(a)



(b)

Figure 4.4-1 1000x photomicrograph of the M-coating on the (a) cathode made from a 5 micron billet and (b) a cathode made from an 11 micron billet.

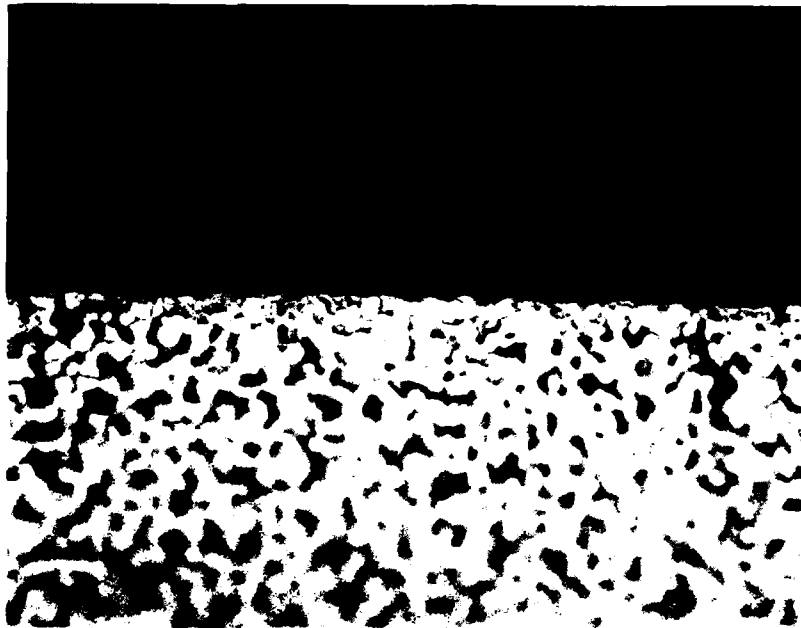
E4355



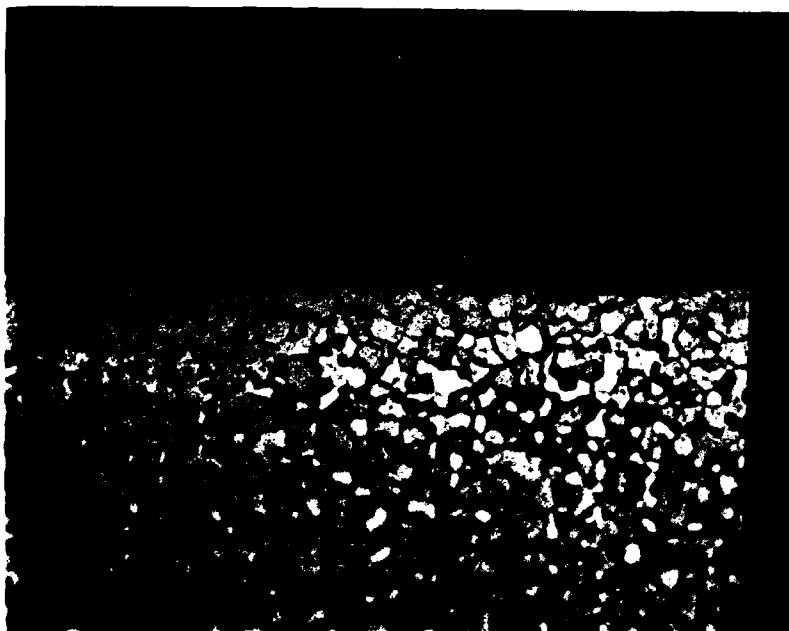
(b) COATED

(a) UNCOATED

Figure 4.4-2 SEM of emitter surface of (a) an uncoated cathode and (b) a coated cathode.



(a)



(b)

Figure 4.5-1 (a) shows the results of a 5 minute water etch, the etch depth is 10 microns. (b) is the results of a 10 minute water etch, the etch depth is 30 microns.

upwards of 200 hours. Since our complete runs are considerably shorter than that, we felt that we had to avoid the smearing in order to improve the ability to see the effect of the processing.

The water etch of the cathode was for 5 min while in an ultrasonic bath.





The depth to which the water leached the aluminates from the pores was studied and can be seen in Figure 4.5-1 a and b. Five minutes of etch removed aluminate  $10\mu$  below the surface. At 10 minutes of etch the depth of aluminate removed was  $30\mu$  below the surface.

#### 4.6 CATHODE GEOMETRY AND IDENTIFICATION

The cathodes fabricated for this study were single tungsten pellets with no other attached parts. Figure 4.6-1 shows the physical layout of the cathodes.

The cathodes were cylinders with a "blackbody hole" in the side. The bottom of the cathode had a notch so that they could be aligned in the heaters. Each cathode that was machined from a given billet was encoded with a specific identification, see Table 4.6-1. These markings identify the powder distribution. On the side of the cathode a letter A, B, C and D were scribed after impregnation so that the aluminate type could be identified and tracked. Impregnation lots A and B were (5:3:2) type and lots C and D were (4:1:1) type.

TABLE 4.6-1  
CATHODE IDENTIFICATION

BILLET	CATHODE MARKINGS
5	 NO MARKINGS
11	 (2) SCRIBE MARKS
5U	 (1) SCRIBE MARK
11U	 (3) SCRIBE MARKS

G12343

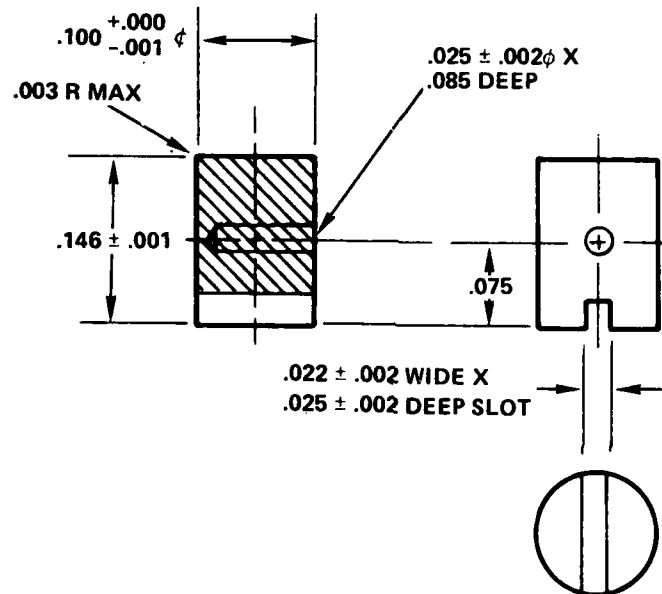


Figure 4.6-1 Cathode print.

## 5.0 CATHODE MEASUREMENT

### 5.1 CATHODE ACTIVATION

After the P.E.T. system was loaded with six (6) pellets it was pumped down and baked out at 200°C for 2 days. The temperature of all the cathodes was brought up relatively slowly so that water and CO could be deabsorbed. After this was done the cathodes were reset to 1100°C until the final background pressure reached the 9 range ( $8-9 \times 10^{-9}$ ). After the background pressure reaches this range, the cathodes and the bakeout heaters were turned off.

At this point cathode measurements begin. The individual cathodes are raised in temperature to 1200°C, for 1 hour, to complete the activation and then are immediately measured.

### 5.2 PULSED CATHODE CHARACTERISTICS

The characteristics of the cathodes were measured (one at a time) by measuring the pulsed cathode current vs. applied accelerating voltage at four (4) different temperatures and three different cathode-to-anode spacings.

The pulsed measurements were made at a .01% duty to prevent anode heating.

Figure 5.2-1 shows a typical pulsed curve. This set of curves was taken once with each cathode to ensure that the pulse was flat in the measurement region and to obtain the delay necessary for the digital Hewlett-Packard high speed DVM system voltmeter which was used to measure the pulses. The delay is marked by the dotted line in Figure 5.2-1. The window over which the voltmeter samples the pulse is 0.5  $\mu$ s.

In Figure 5.2-1 the voltage is seen by circles and the current on an arbitrary scale is shown with crosses. Figure 5.2-2 through 5.2-4 shows a typical set

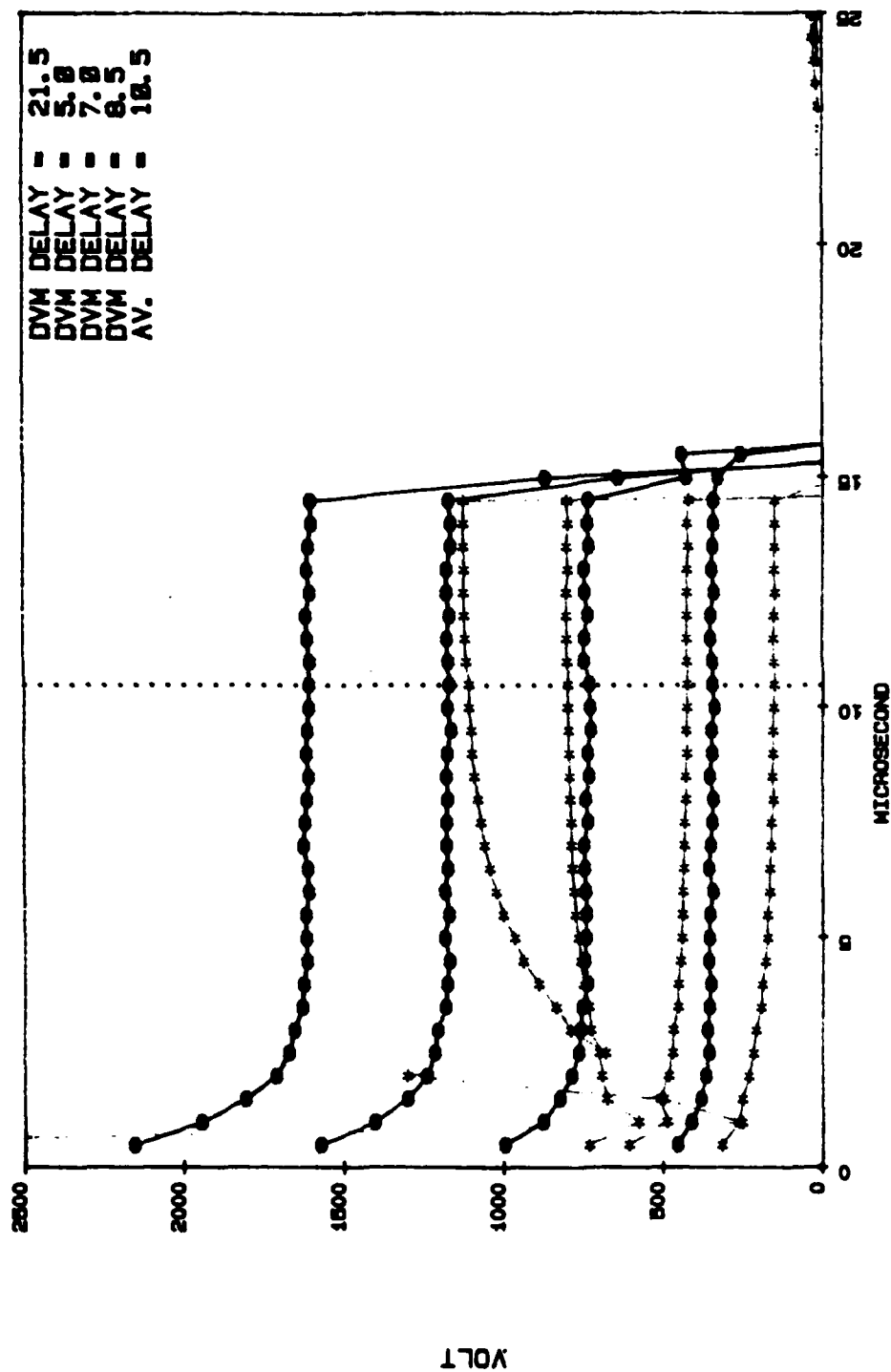


Figure 5.2-1 Digital pulsed curve which shows the typical pulse and position on the pulse at which the measurements were made.  
 (1) are voltage and \* are currents (in arbitrary units).



SAMPLE ID. B5M

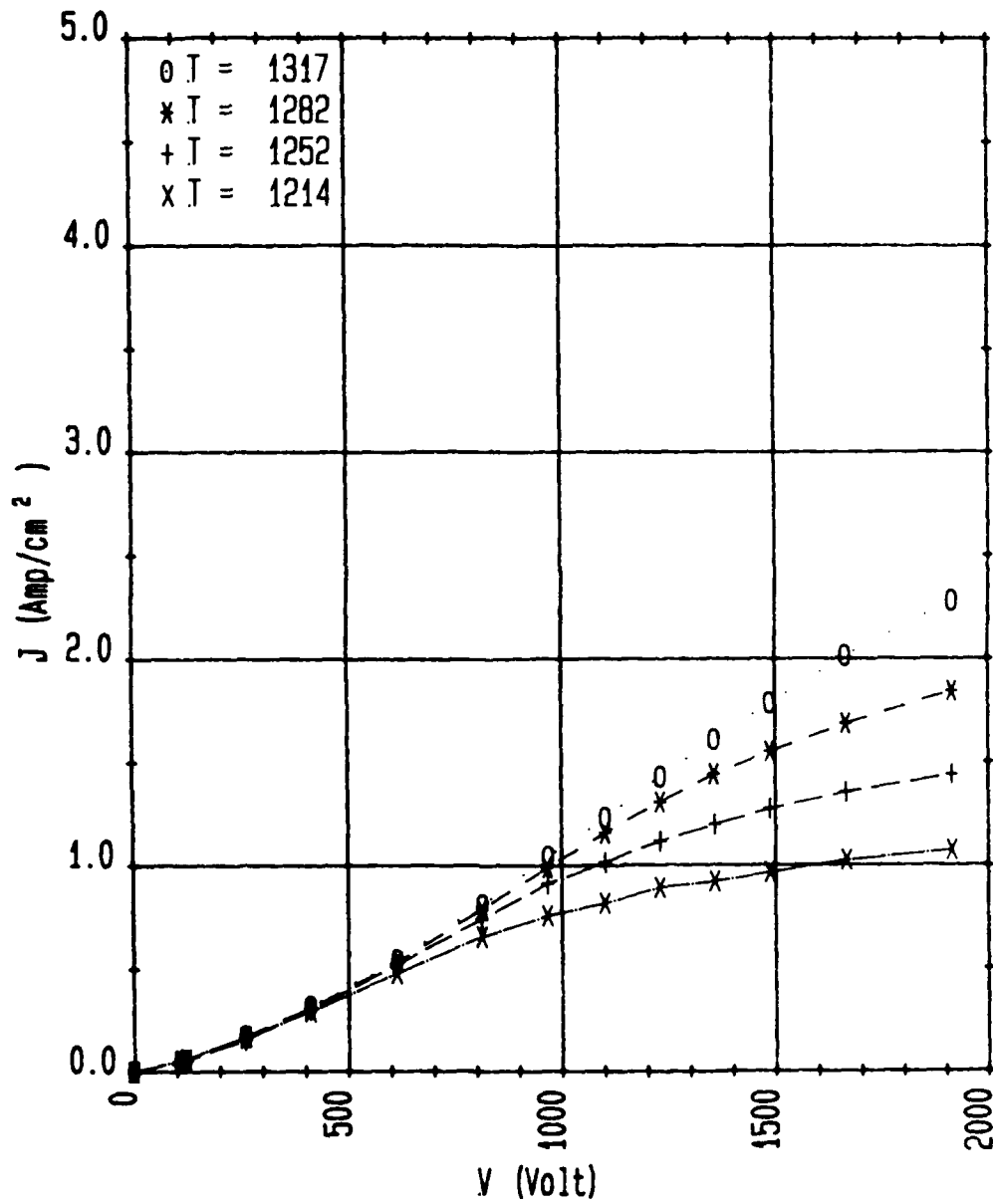


Figure 5.2-2 Current density-voltage-temperature ( $^{\circ}\text{K}$ ) characteristic at cathode-to-anode spacing of 0.22 cm.

SAMPLE ID. B5M

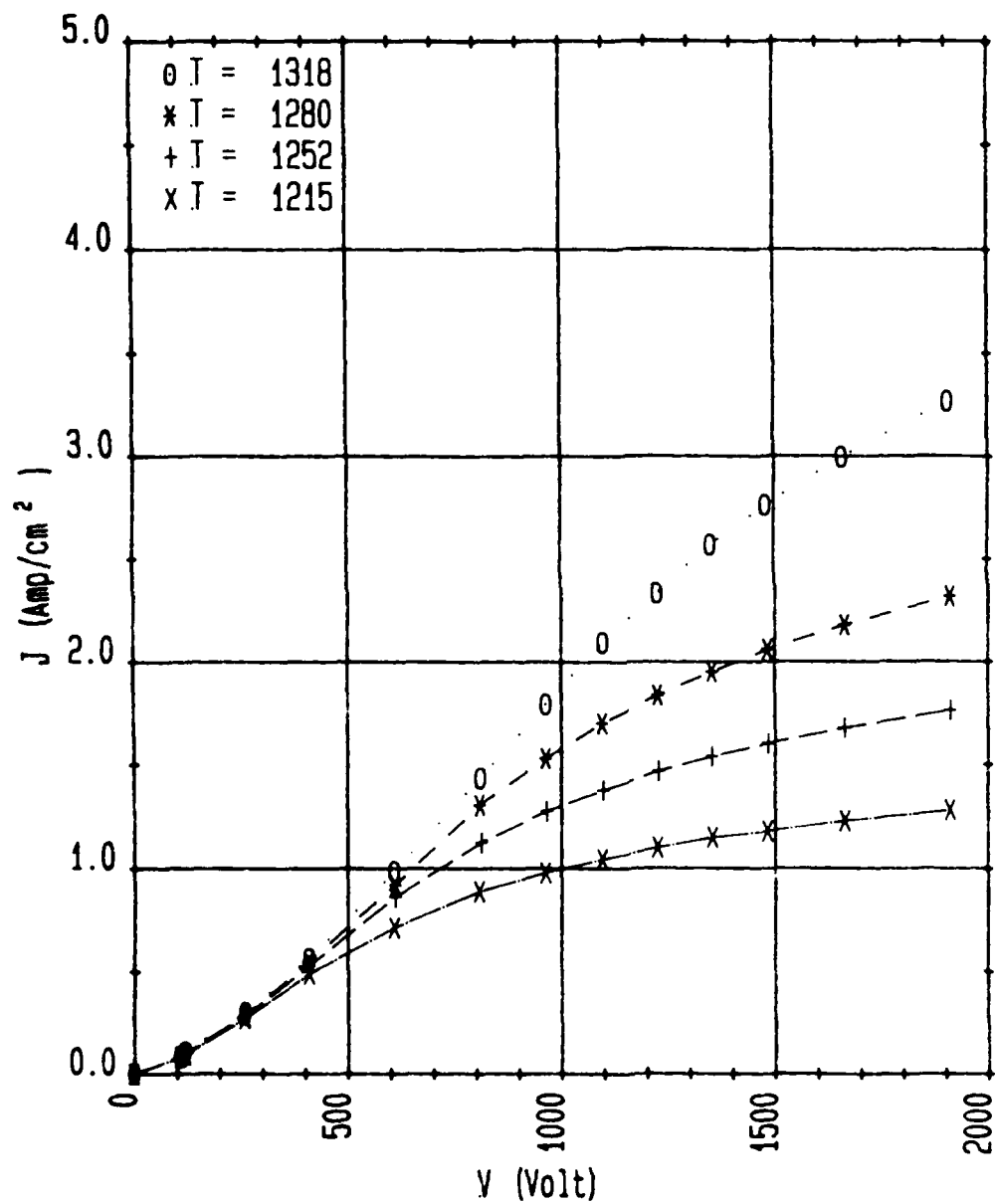


Figure 5.2.3 Current density-voltage-temperature ( $^{\circ}\text{F}$ ) characteristics at cathode-to-anode spacing of 0.15 cm.

SAMPLE ID. B5M

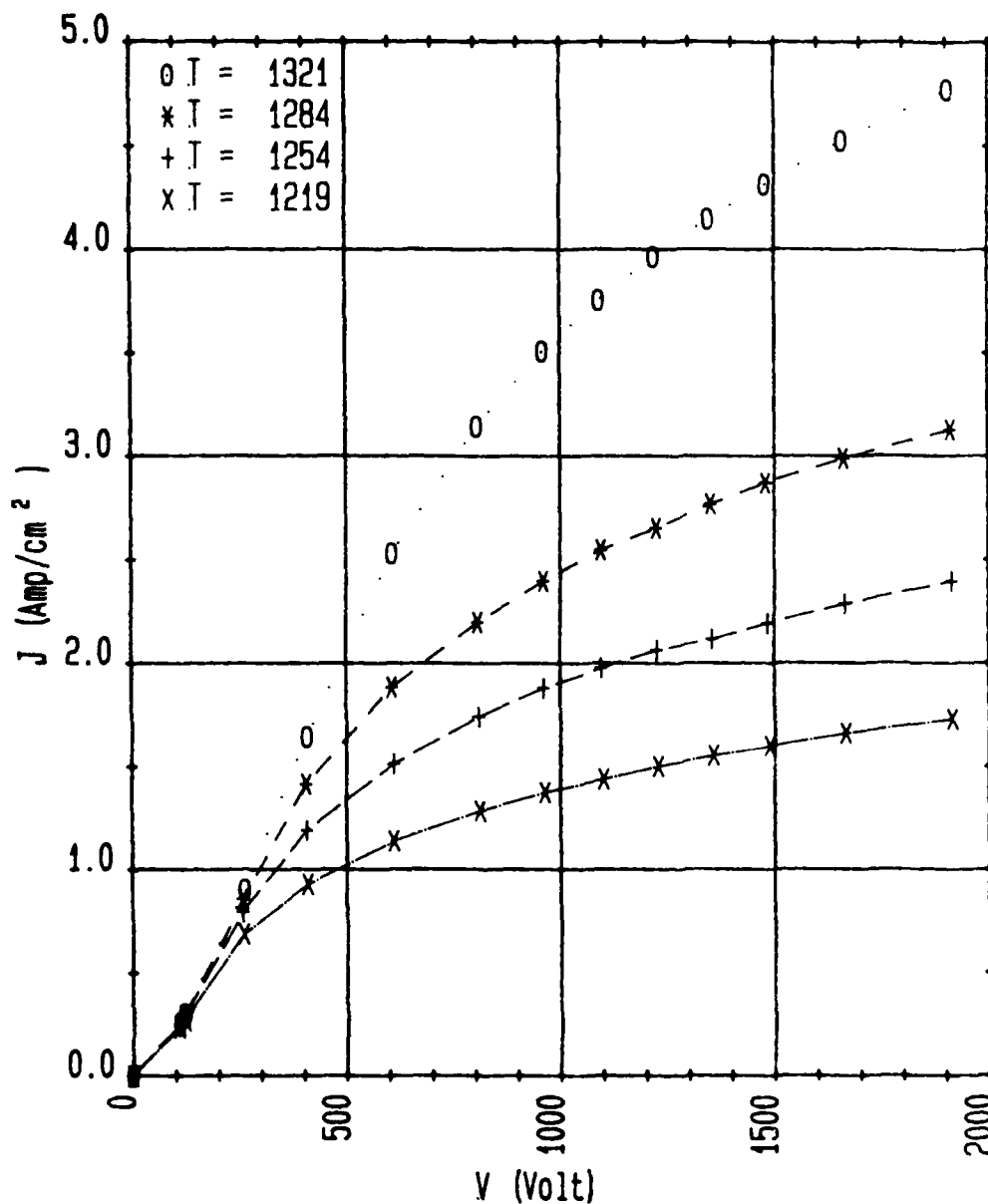


Figure 5.2-4 Current density-voltage-temperature ( $^{\circ}\text{K}$ ) characteristics at cathode-to-anode spacing of 0.08 cm.

of current-voltage-temperature (I-V-T) data. All measurements were made under computer control (using a HP 9825) and the data stored on tape.

All temperatures were measured with a single color, disappearing wire optical pyrometer. The temperatures are true temperatures since they were measured on the "blackbody hole" provided in the cathode. All temperatures were corrected for the sapphire window through which they were measured.

### 5.3 EVALUATION OF CATHODE CHARACTERISTICS

The pulsed current-voltage temperature and spacing (I-V-T-D) data was analyzed via the technique described in Appendix A using the reciprocal formula

$$J = \frac{J_{SC} J_{TL}}{J_{SC} + J_{TL}} \quad (5.3-1)$$

to extract  $J_{TL}$  from the data, and finally the work function by inverting  $J_{TL}$ .

In Figures 5.3-1 to 5.3-6, data for BSM are plotted using the Schottky format. The horizontal axis is the square root of the cathode to anode voltage and the vertical axis is the natural log of the current density.

In Figures 5.3-1 to 5.3-3 the data is shown at one temperature and 3 spacings. The circles are the experimental data, the solid line that fits the circles is the best fit to equation 1 and the dotted line is  $J_{TL}$ .

In Figures 5.3-4 to 5.3-6 the same data is shown. In these figures the Schottky technique is used to obtain  $J_{TL}$  at  $V=0$ . This technique essentially takes the last two or so points and draws a tangent to them which is then extrapolated to  $V=0$ . The solid line is the tangent line. The circles are the data points and the dotted line is just a line drawn through the points and is not a fit.

In Appendix A we present a more detailed discussion of these analysis techniques.

SAMPLE ID. B5M

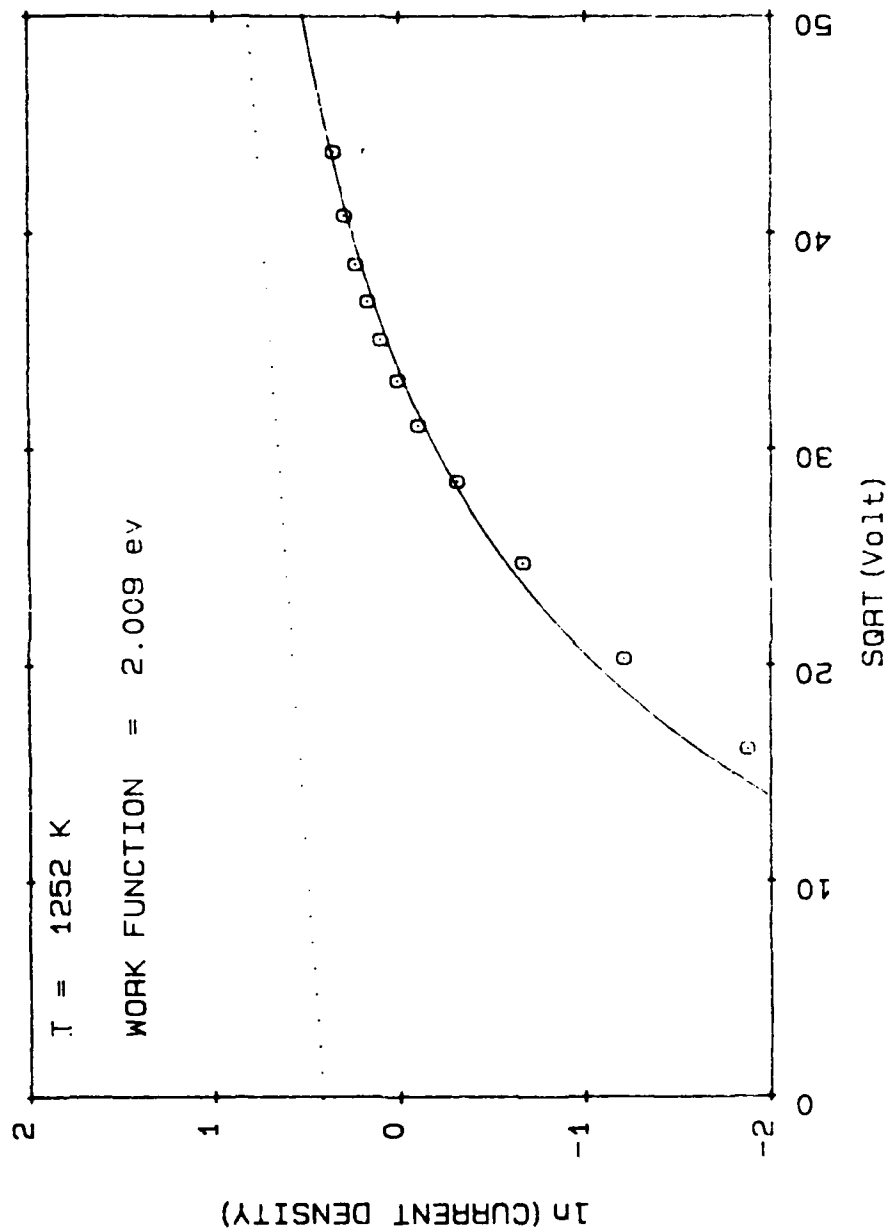


Figure 5.3-1 Schottky plot of data using equation 1 to fit data.

SAMPLE ID. B5M

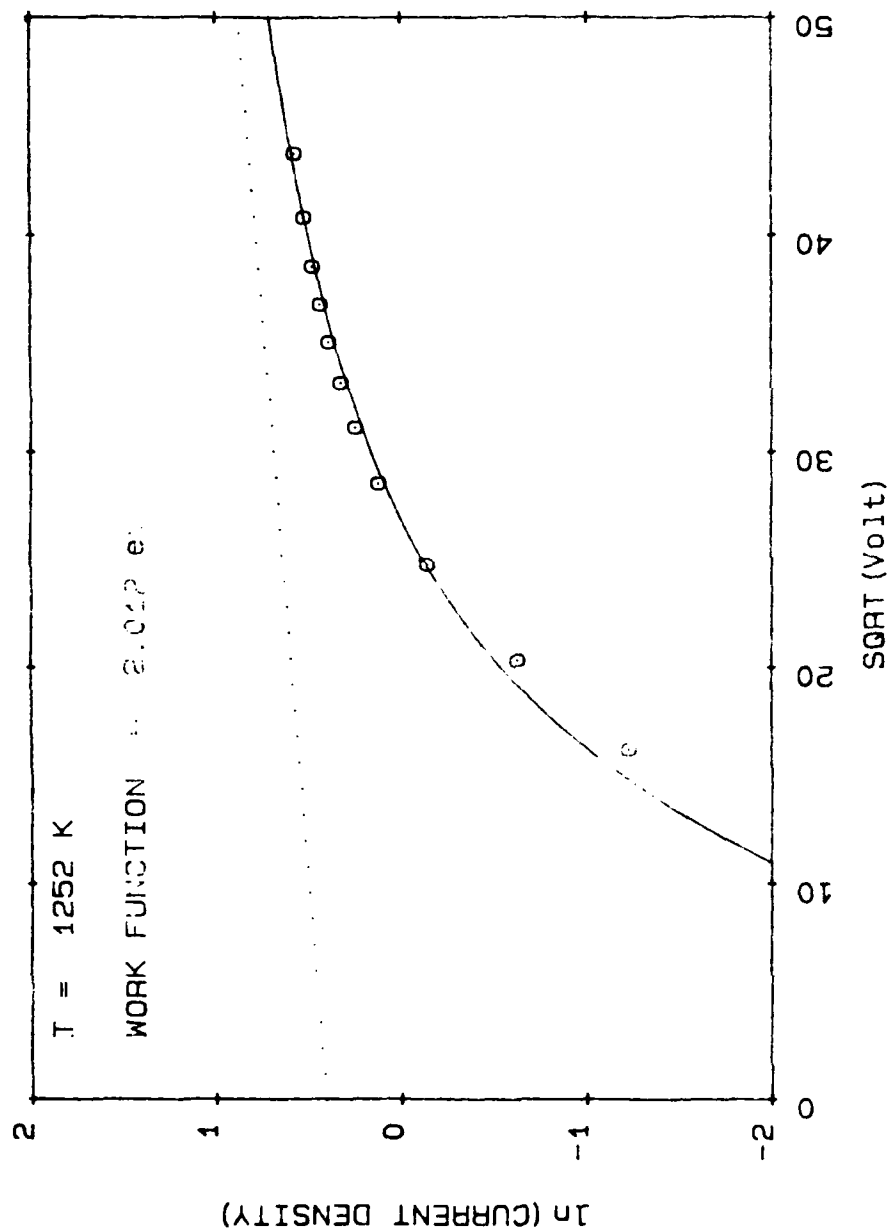


Figure 5.3-2 Schottky plot of data using equation 1 to fit data.

SAMPLE ID. B5M

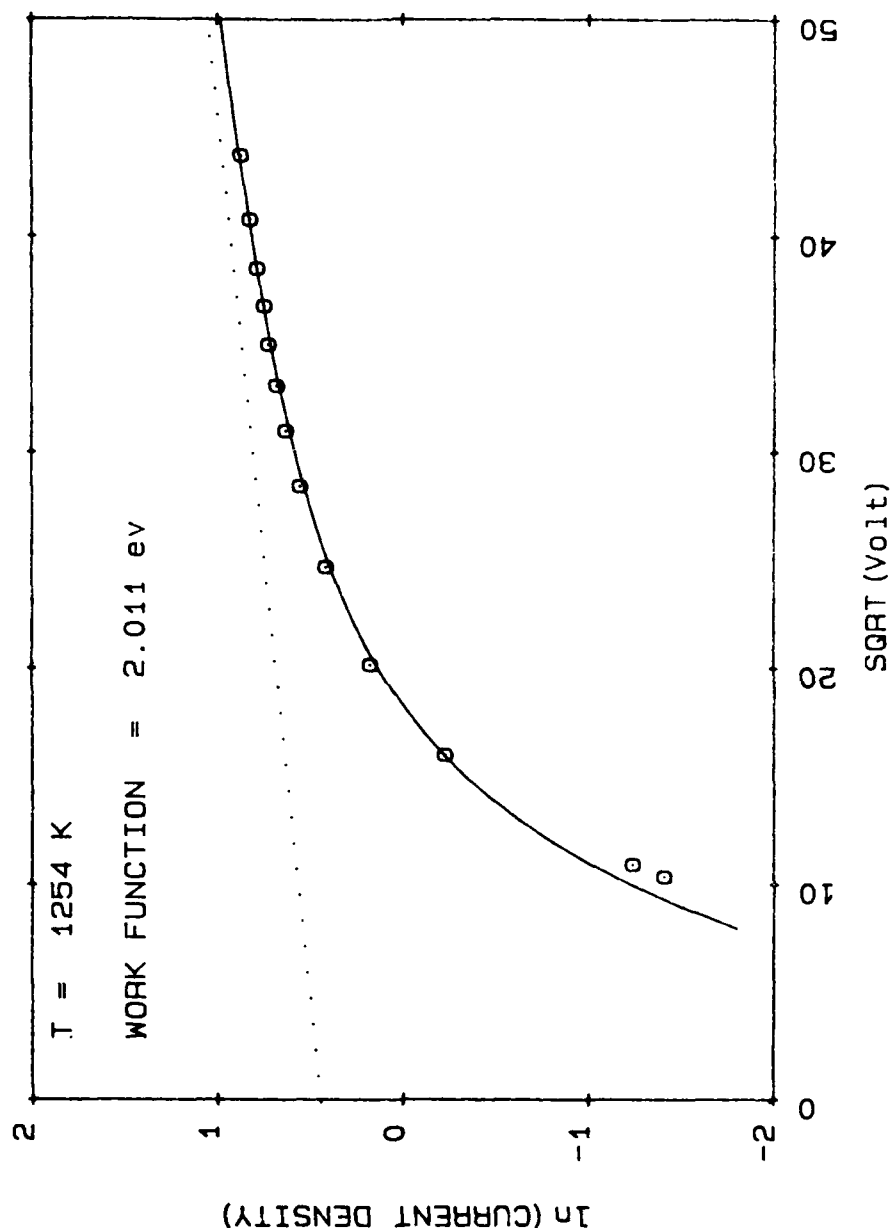


Figure 5.3-3 Schottky plot of data using equation 1 to fit data.

SAMPLE ID. B5M

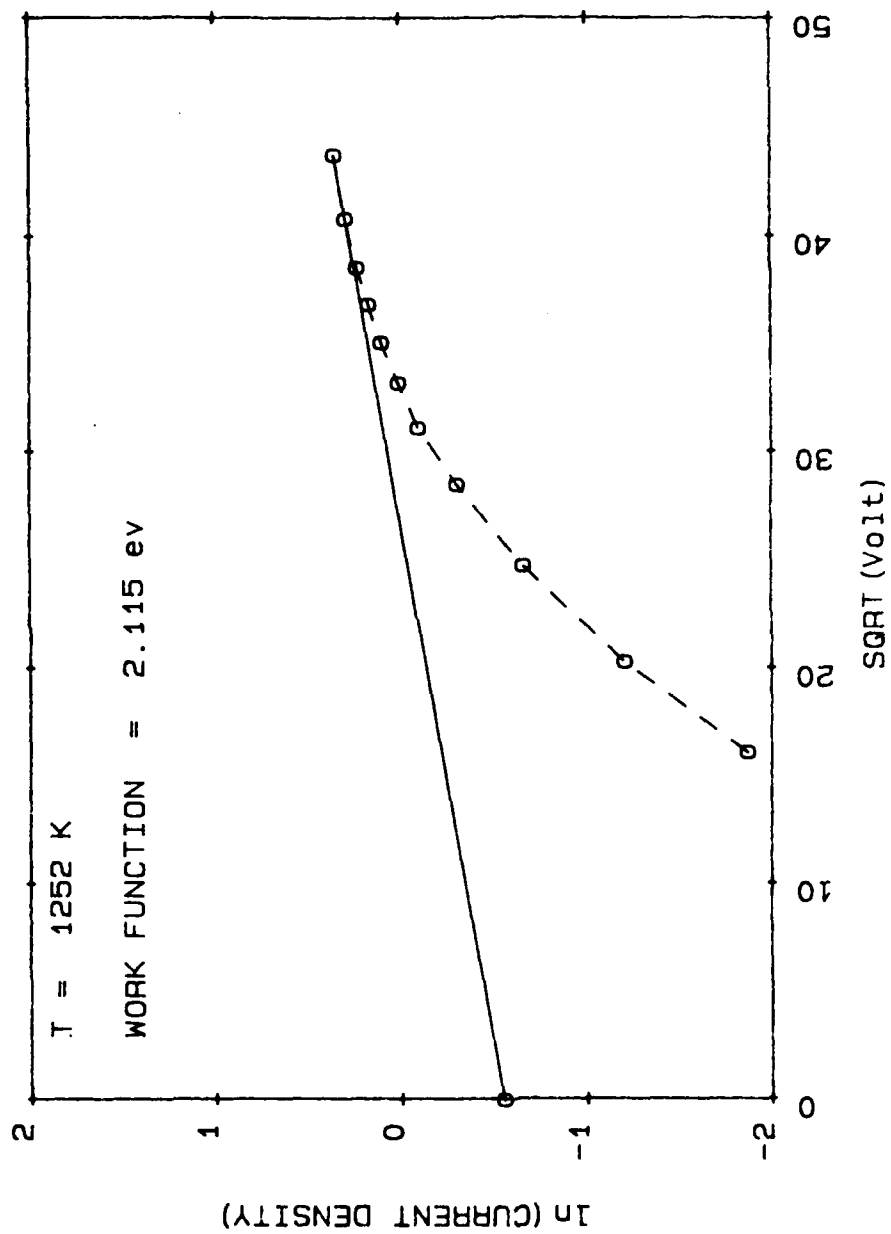


Figure 5.3-4 Schottky plot using the Schottky technique to fit the data.



SAMPLE ID. B5M

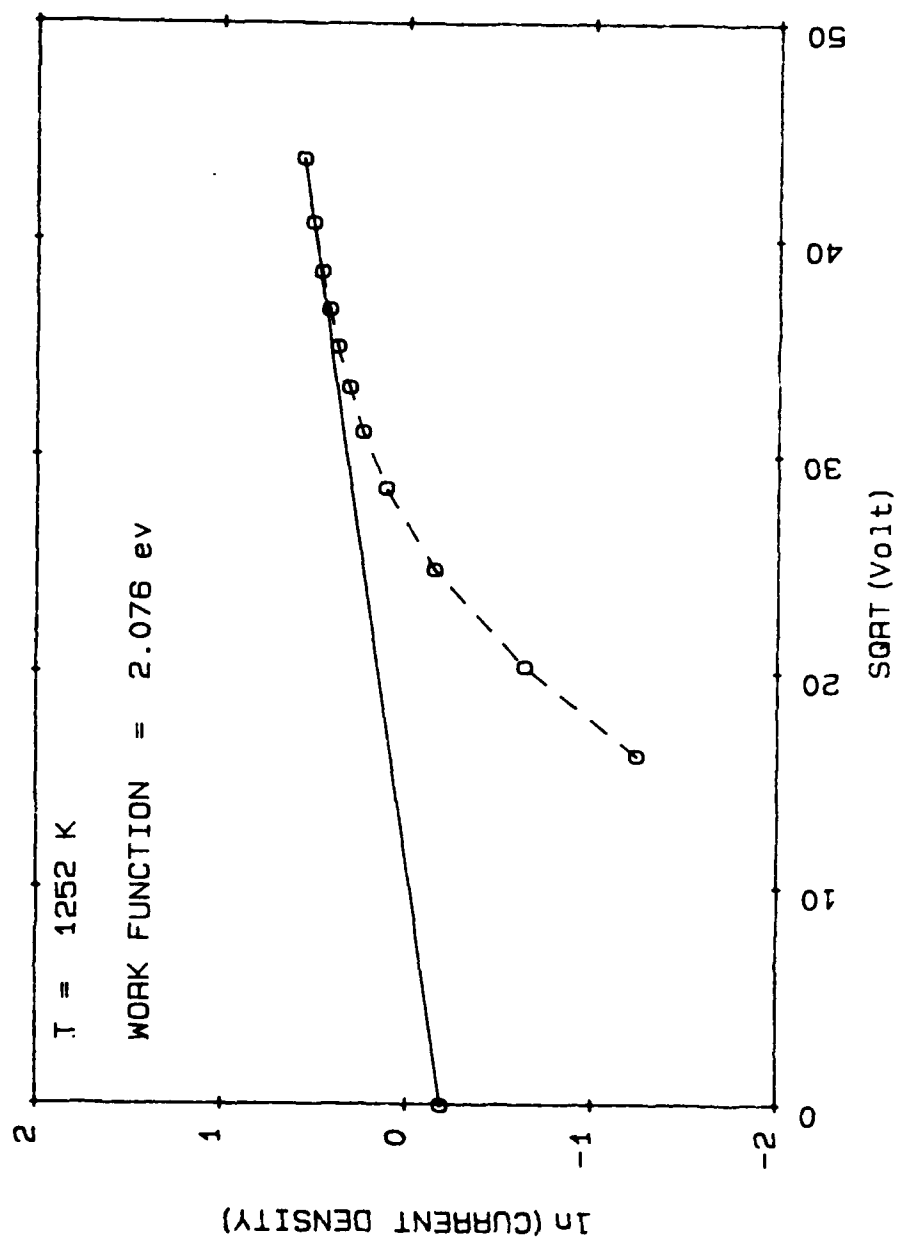


Figure 5.3-5 Schottky plot using the Schottky technique to fit data.

SAMPLE ID. B5M

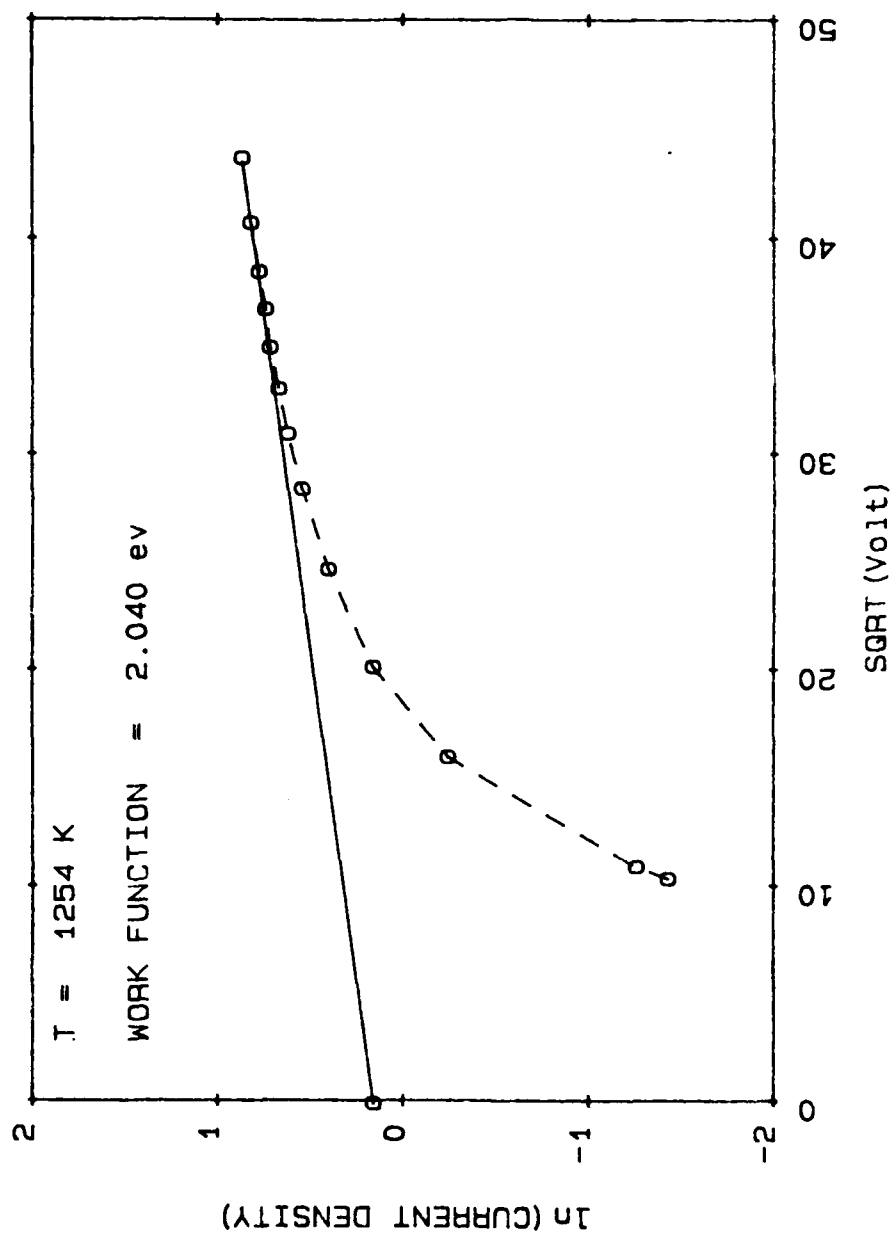


Figure 5.3-6 Schottky plot using the Schottky technique to plot the data.

#### 5.4 EVAPORATION RATE MEASUREMENTS

Evaporation rate measurements were made by the Becker wire technique. There are a number of subtleties and difficulties with this technique. Care must be taken to identify the correct peak. Usually two peaks can be observed. The first peak is sometimes observed as a shoulder instead of a real peak. The shape of this curve depends upon the temperature of the Becker wire. If care is not taken to measure the first peak, an erroneous result will be obtained. The second peak is much broader, and we now believe it is due to surface diffusion along the Becker wire until the entire hot zone of the wire is coated. The first peak is the real peak of interest and if the Becker wire temperature is too high it does not appear. The data taken and presented in this report was obtained from the first peak. The data is given in Appendix B.

## 6.0 RESULTS AND DISCUSSIONS

There were a total of 500 individual current-voltage-temperature-spacing (I-V-T-D) measurements made on the samples in this program. The analysis of the I-V-T-D data was discussed in detail in section 5 and in Appendix A. In this section we present the analysis and workfunctions which were derived from the reciprocal current formula. These results are the basis of all the modeling we will do in section 7.0. The analysis of the data involved extracting a workfunction from each of the I-V-T-D curves. The set of workfunction data thus derived was then statistically analyzed and the result presented in this section.

There was one main selection criterion used to keep or reject work functions for the data set. The criterion to keep data is that

$$J_{TL}/J_{SC} < 1, \quad (6.1)$$

at the highest voltage measured for the I-V-T-D curve. This criterion insures that the data contains sufficient amount of temperature limited information so that a reliable workfunction can be obtained. When  $J_{TL}/J_{SC} \approx 1$ , the I-V-T-D curve contains mostly space charge information with very little cathode information.

### 6.1 WORKFUNCTION DISTRIBUTION

The workfunction of the data set is summarized by a series of histograms. Each histogram represents a statistical distribution and was evaluated against both the Gamma distribution and the Wiebull distribution.

These two distributions were selected for study because we believe that a single ended distribution is necessary for the study of workfunctions. This

comes from the argument that there can be a maximum lowering of the workfunction created by a perfect dipole covered surface. Any disruption of this perfect dipole coverage will only raise the workfunction, never lower it.

The single ended nature of the distribution assumes however that the variations due to dipole arrangement are dominant over the distribution due to measurement errors, which will be gaussian.

The gamma distribution function is considered by many to be the basic distribution of statistics for variable bounded on one side ( $0 < x < \infty$ )

The gamma probability density function is

$$f(x; \eta, \lambda) = \begin{cases} \frac{\lambda^\eta}{\Gamma(\eta)} x^{\eta-1} e^{-\lambda x} & x \geq 0, \lambda > 0, \eta > 0 \\ 0 & \text{elsewhere} \end{cases} \quad (6.1-1)$$

where

$$\Gamma(\eta) = \int_0^\infty x^{\eta-1} e^{-x} dx, \quad (6.1-2)$$

is the gamma function.

The generalized gamma distribution is obtained by the linear transformation

$$x \rightarrow x - \mu \quad (6.1-3)$$

where  $\mu$  is the minimum value.

The expected value for the gamma distribution is given by

$$\langle x \rangle = \mu + \frac{\eta}{\lambda}, \quad (6.1-4)$$

and the standard deviation is the square root of the variance

$$\eta/\lambda^2. \quad (6.1-5)$$

The generalized Weibull distribution is also bounded on one end ( $0 \leq x \leq \infty$ ) and is given by

$$f(x, \eta, \sigma, \mu) = \begin{cases} \frac{\eta}{\sigma} \left( \frac{x-\mu}{\sigma} \right)^{\eta-1} e^{-\left( \frac{x-\mu}{\sigma} \right)^{\eta}} & x \geq \mu, -\infty < \eta < +\infty \\ 0 & \text{elsewhere} \end{cases} \quad \begin{matrix} \sigma > 0, \mu > 0 \end{matrix} \quad (6.1-6)$$

The expected value is

$$\langle x \rangle = \mu + \sigma \Gamma\left(\frac{1}{\eta} + 1\right) \quad (6.1-7)$$

and the variance is

$$\sigma^2 \left\{ \Gamma\left(\frac{2}{n} + 1\right) - \left( \Gamma\left(\frac{1}{n} + 1\right) \right)^2 \right\} . \quad (6.1-8)$$

Both these distribution were fit to the histograms. The gamma distribution gave consistently a lower chi squared  $\chi^2$  (i.e., a better fit to the histogram).

We have consequently only given the gamma distribution results.

In Table 6.1-1 the gamma distribution parameters are summarized for all the samples in the experimental matrix. Table 6.1-2 gives a more coarse analysis where the classified and unclassified powder distribution are not broken out by particle size.

Figure 6.1-1 shows a histogram of all samples combined, both coated and uncoated, S and B types. This data clearly show the lower bounded nature of the distribution. Figure 6.1-2 and 6.1-3 separate out the uncoated and the coated cathodes again combining the S and B types. Figures 6.1-4, 6.1-5 and 6.1-6 are the coated S-type cathodes combining all the power distributions, (i.e., 5, 11, 5U and 11U). In Figures 6.1-7, 6.1-8 and 9.6-9 the coated B-type cathodes are given again combining the 5, 11, 5U and 11U powder distributions. Figures 6.1-10, 11, 12, 13, 14 and 15 are similar histograms for the uncoated cathodes. The next of 16 figures, Figure 6.1-16 to Figure 6.1-31 break the distribution down to the individual cathodes in the experimental matrix.

TABLE 6.1-1  
 GAMMA DISTRIBUTION PARAMETERS OBTAINED BY FIT TO WORK FUNCTION HISTOGRAMS

	B-TYPE (5: 3: 2)				S-TYPE (4: 1: 1)			
	5	11	5U	11U	5	11	5U	11U
UNCOATED								
MINIMUM	2.13	2.14	2.20	2.08	2.02	2.03	2.04	2.02
AVERAGE	2.20	2.20	2.22	2.12	2.07	2.07	2.08	2.04
STD DEV	0.04	0.06	0.01	0.02	0.02	0.03	0.02	0.01
COATED								
MINIMUM	1.95	1.91	1.93	2.02	1.89	1.93	1.93	1.94
AVERAGE	2.00	2.05	2.01	2.06	1.98	1.98	1.97	1.98
STD DEV	0.03	0.02	0.02	0.02	0.02	0.03	0.02	0.01



TABLE 6.1-2

GAMMA DISTRIBUTION PARAMETERS OBTAINED BY FIT TO WORK FUNCTION HISTOGRAMS

	B-TYPE (5: 3: 2)		S-TYPE (4: 1: 1)	
	CLASSIFIED	UNCLASSIFIED	CLASSIFIED	UNCLASSIFIED
UNCOATED				
MINIMUM	2.15	2.09	2.02	2.03
AVERAGE	2.22	2.13	2.07	2.08
STD DEV	0.07	0.04	0.02	0.02
COATED				
MINIMUM	1.95	1.94	1.92	1.89
AVERAGE	2.04	2.03	1.98	1.97
STD DEV	0.06	0.04	0.03	0.02

# ALL CATHODES

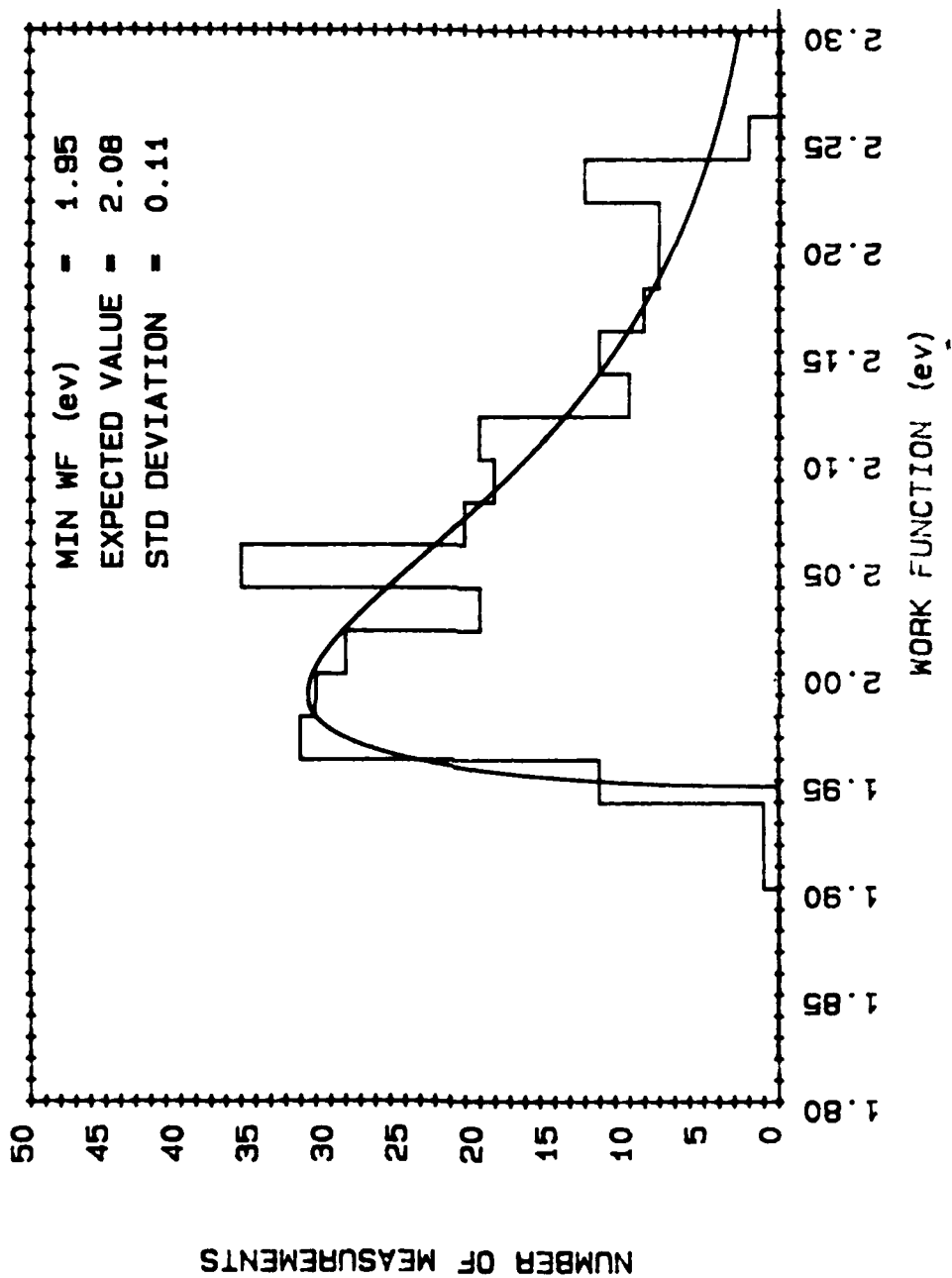


Figure 6.1-1 Single histogram combining all cathodes measured in this program.

# ALL TUNGSTEN UNCOATED CATHODES

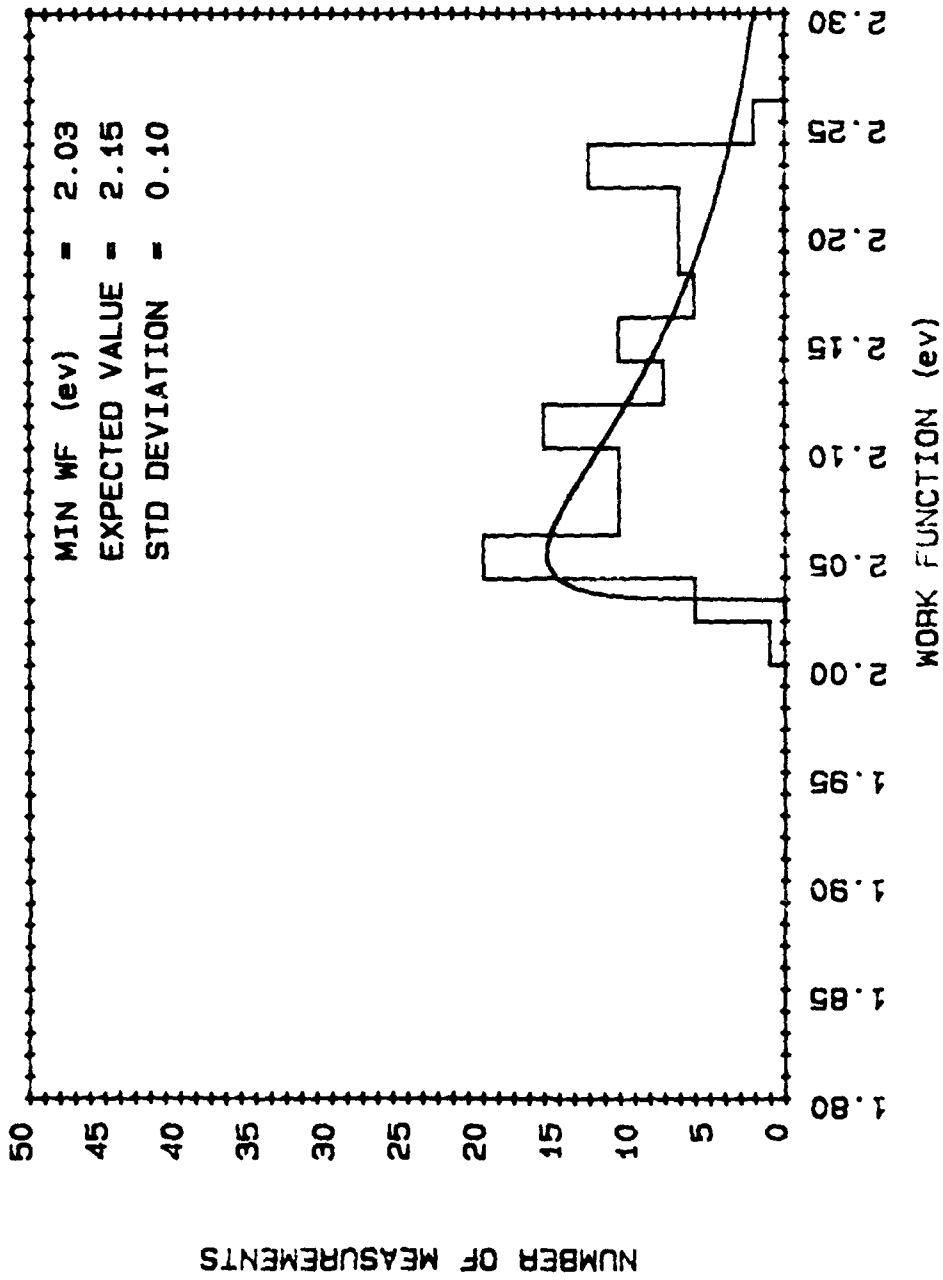


Figure 6.1-2 All tungsten cathodes.

# ALL OsRu COATED CATHODES

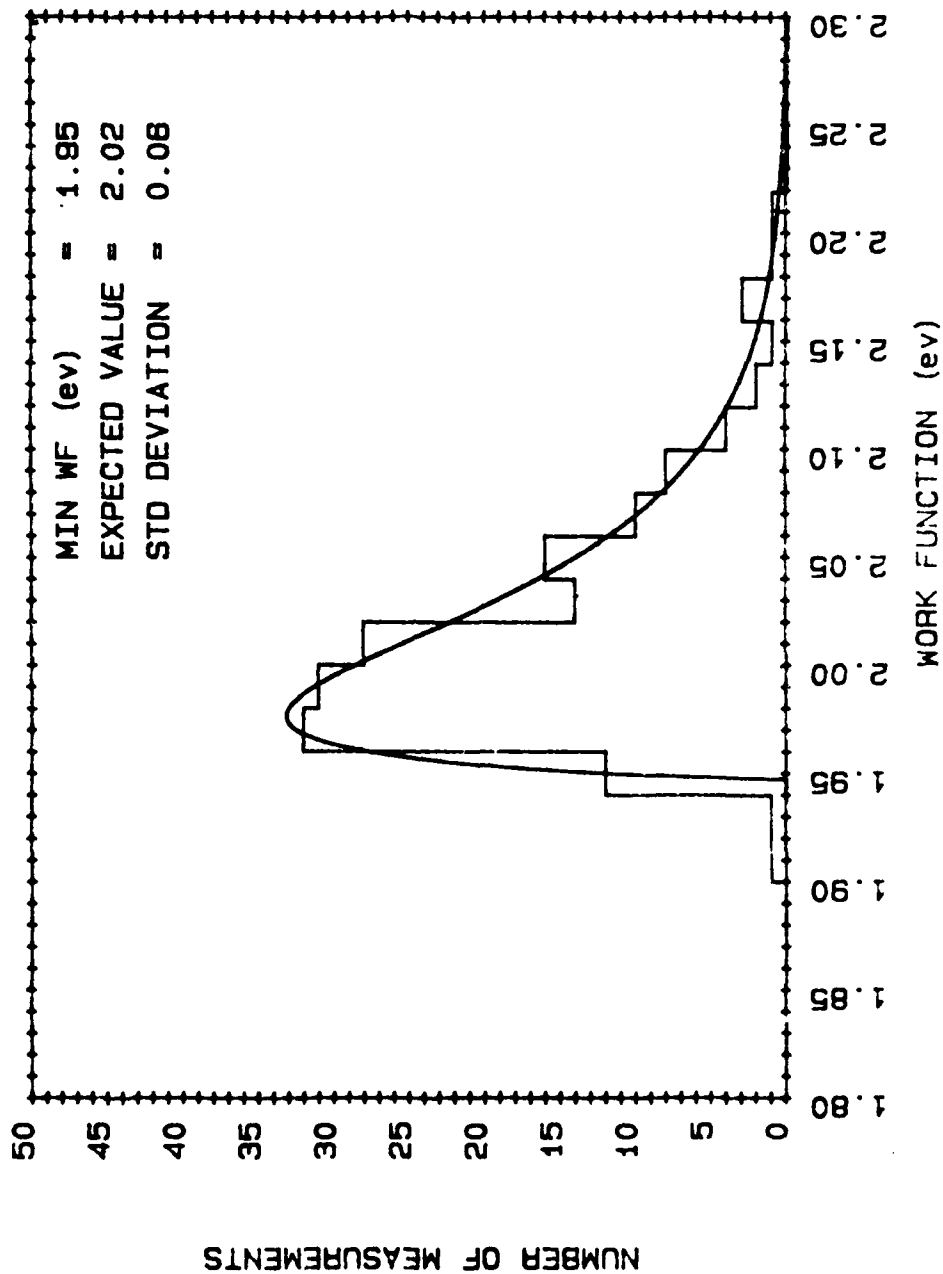


Figure 6.1-3 All OsRu coated cathodes.

# OsRu COATED S-TYPE CATHODES

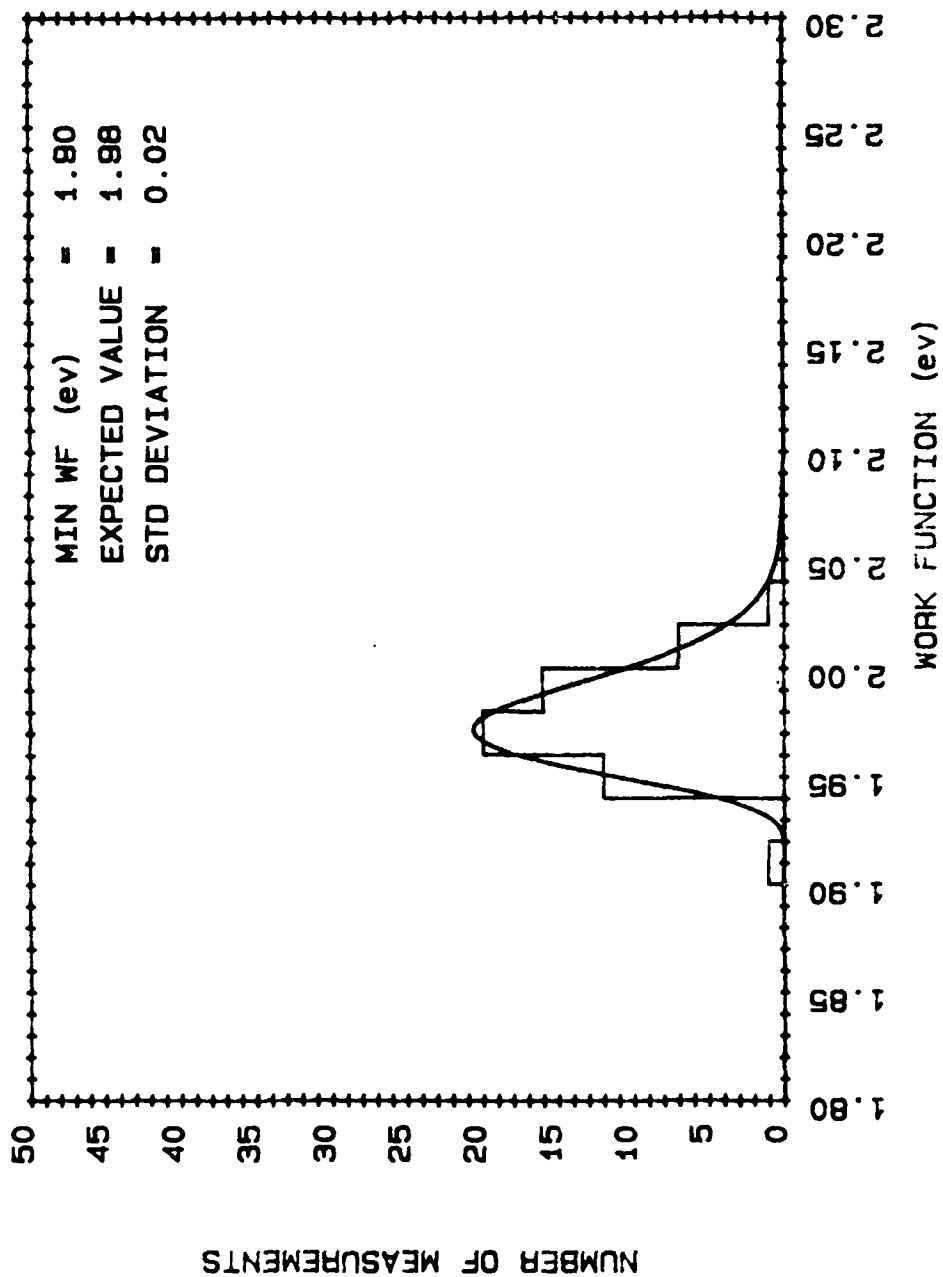


Figure 6.1-4 All S-type, OsRu coated cathodes.

# OsRu COATED S-TYPE 5 AND 11 MICRON

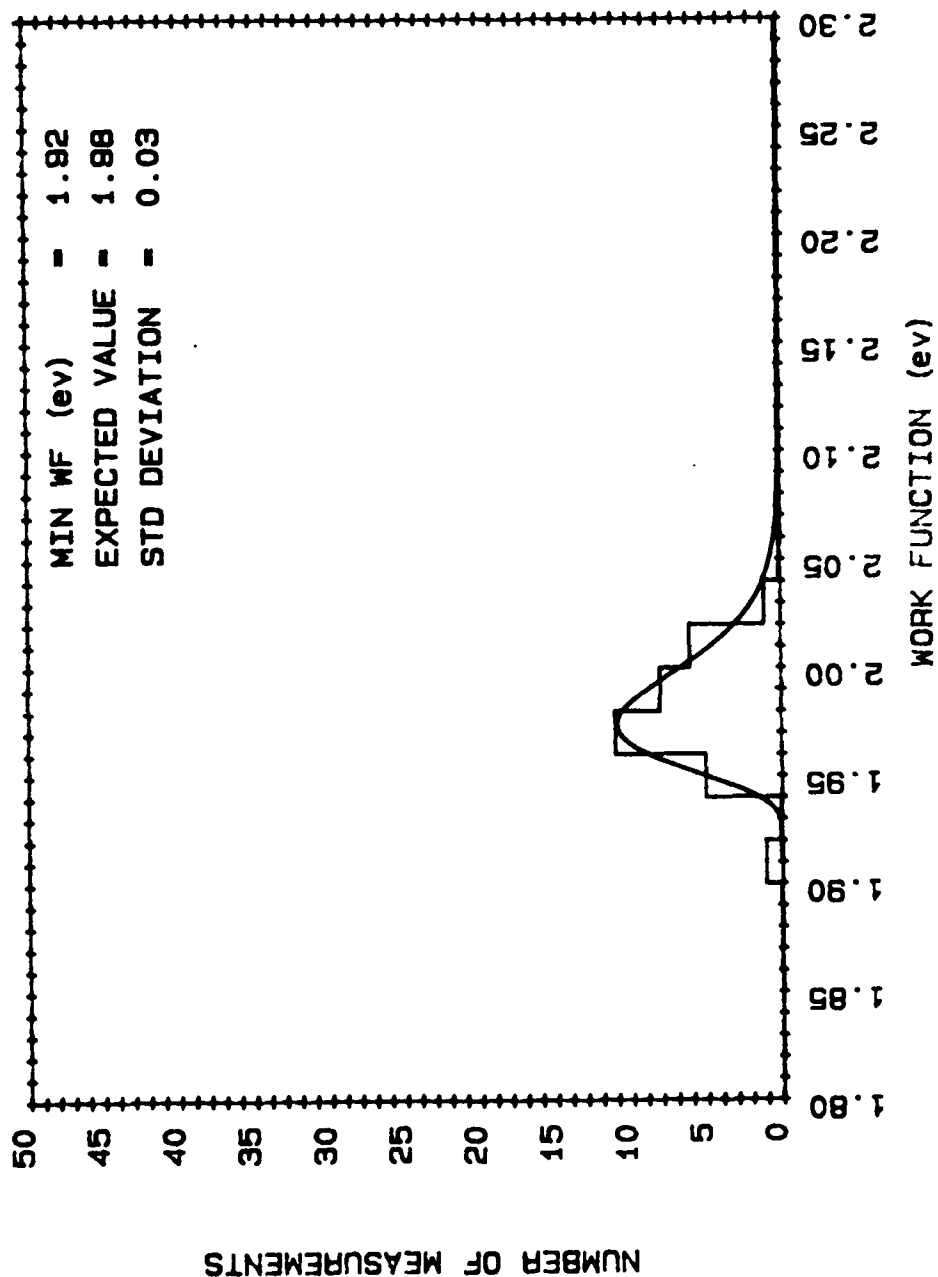


Figure 6.1-5 S-type classified OsRu coated.

# OsRu COATED S-TYPE UNCLASSIFIED

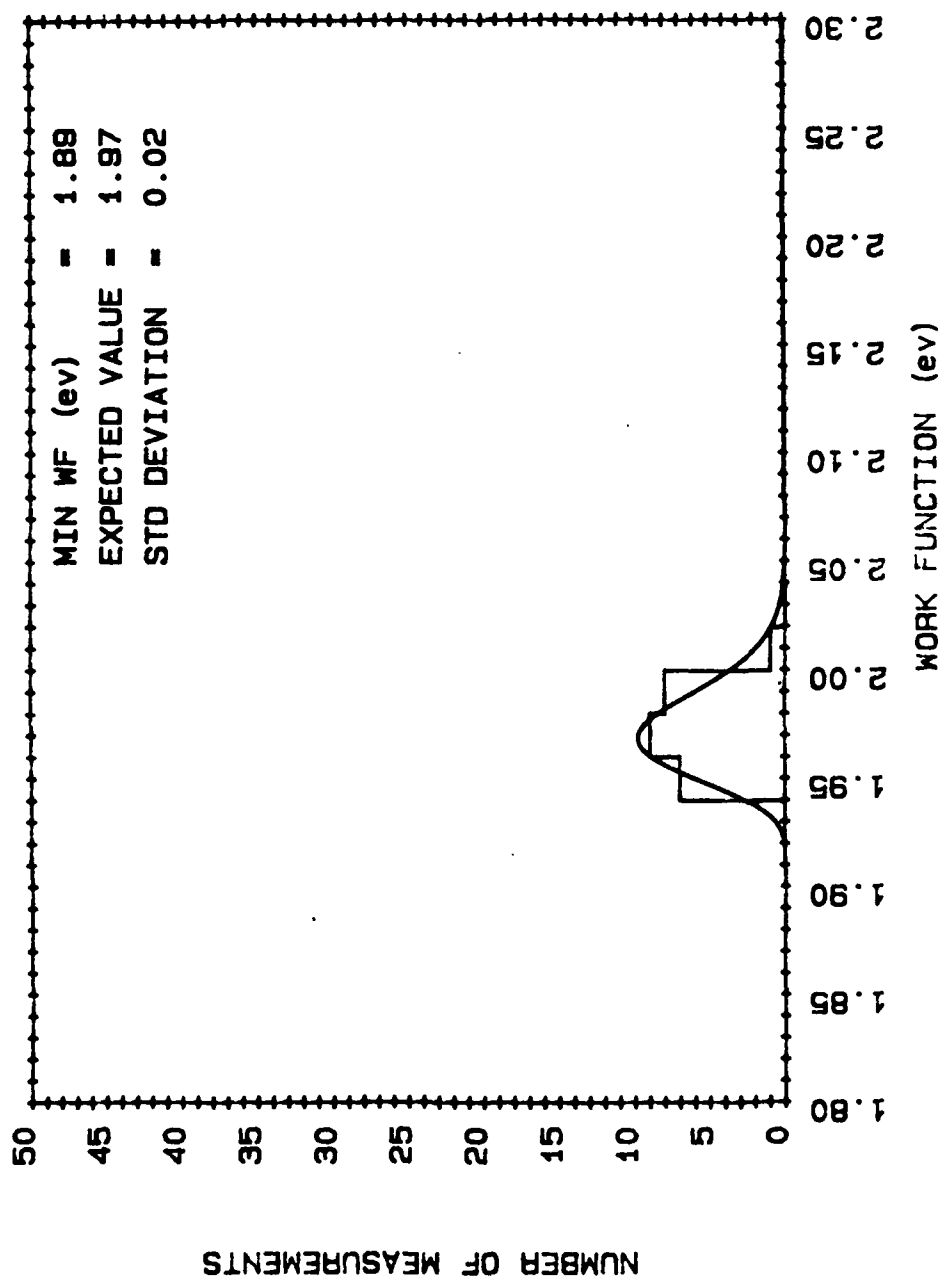


Figure 6.1-6 S-type unclassified, OsRu coated.

# ALL OsRu COATED B-TYPE CATHODES

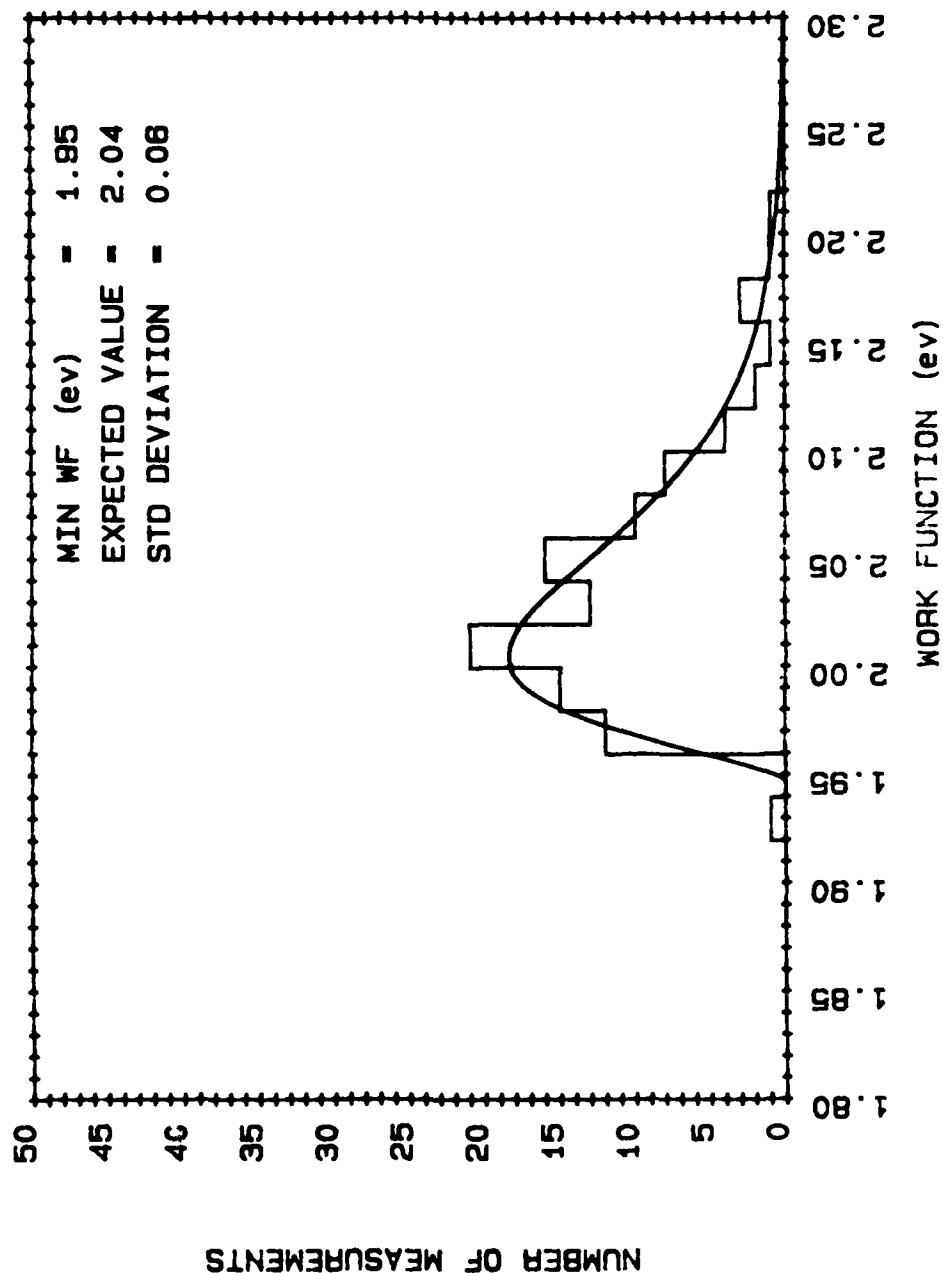


Figure 6.1-7 All B-type OsRu coated.



# OsRu COATED B-TYPE 5 AND 11 MICRON

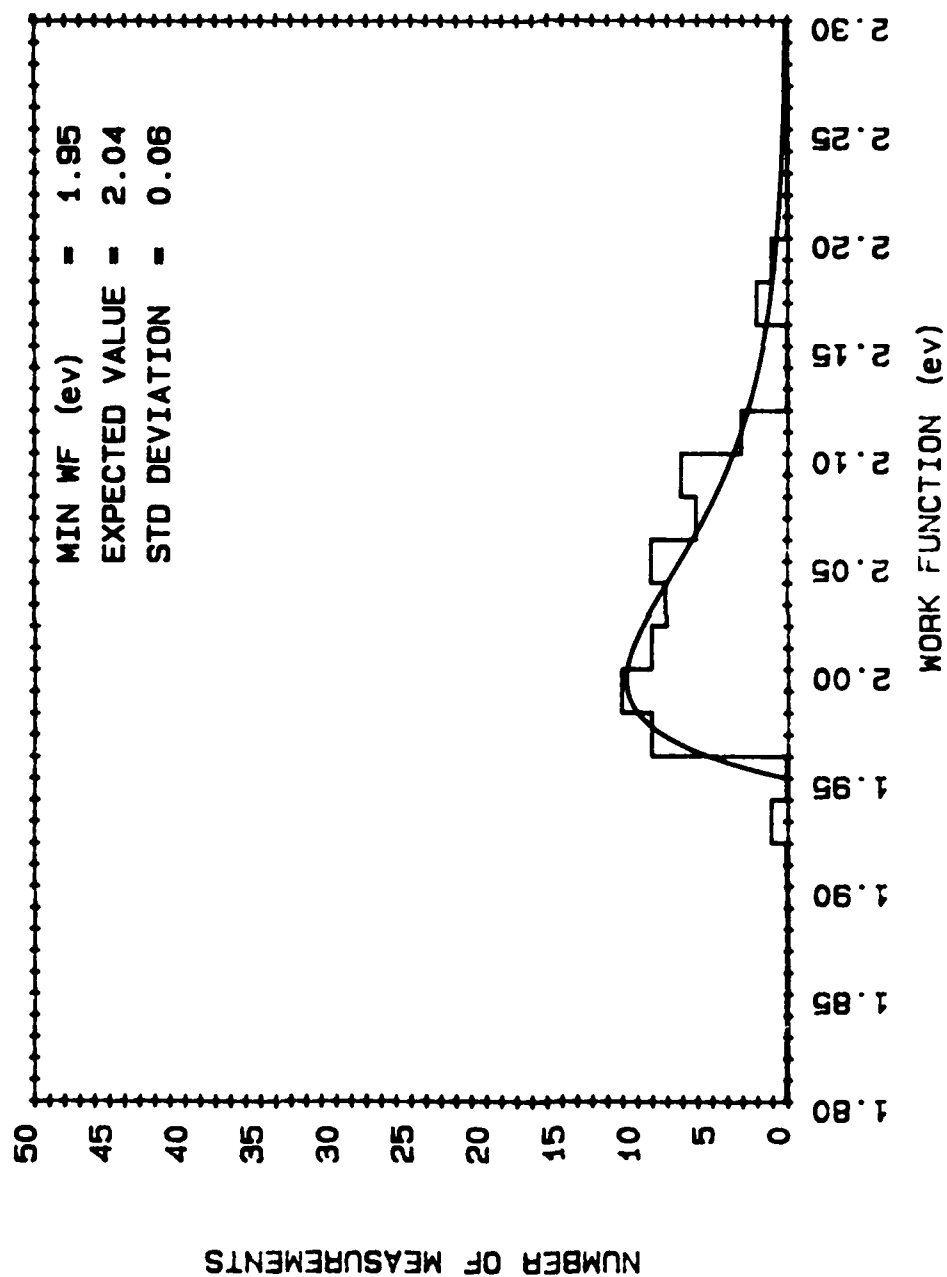


Figure 6.1-3 B-type classified OsRu coated.

# OsRu COATED B-TYPE UNCLASSIFIED

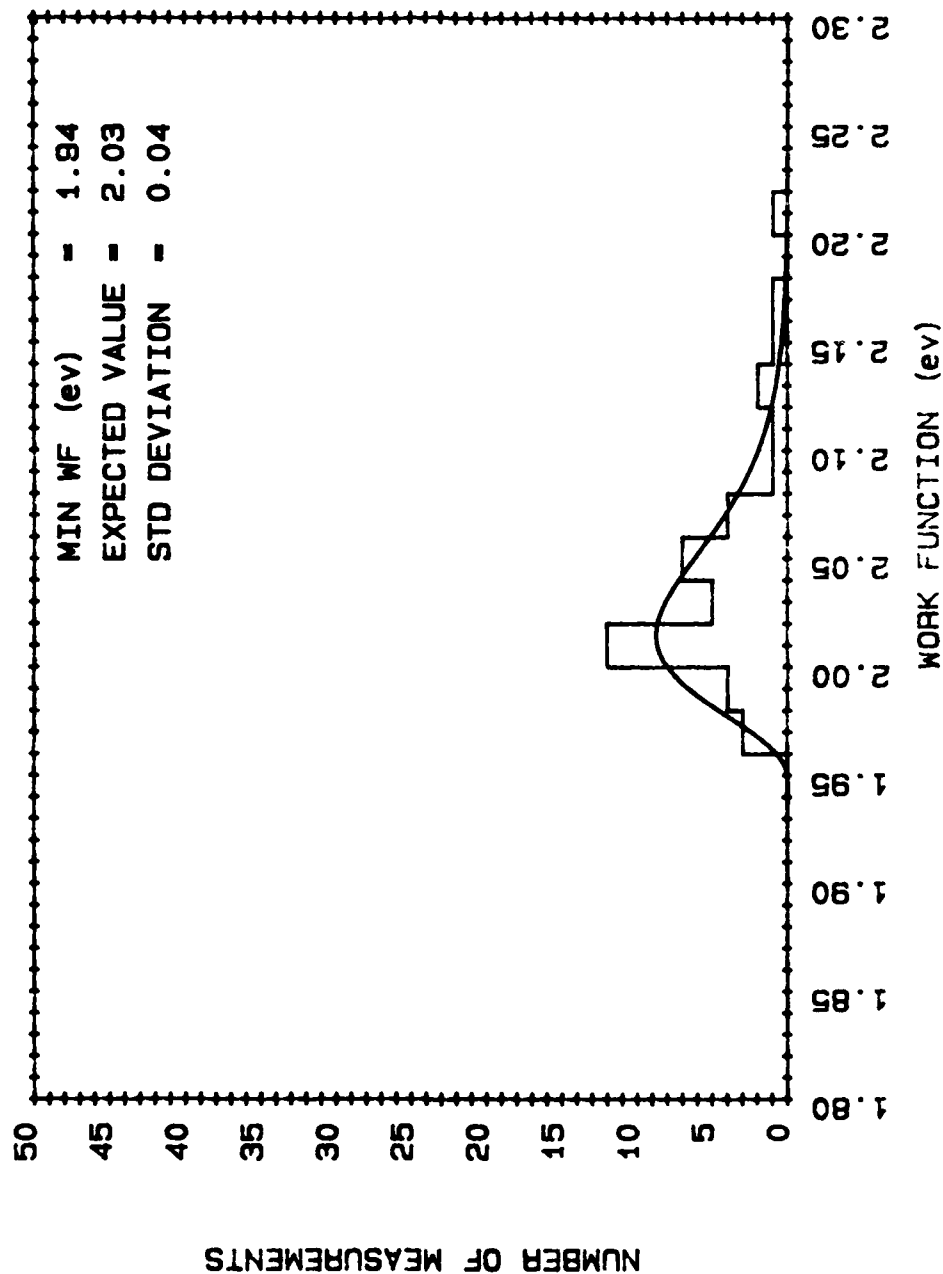


Figure 6.1-9 B-type unclassified OsRu coated.

# ALL TUNGSTEN S-TYPE CATHODES

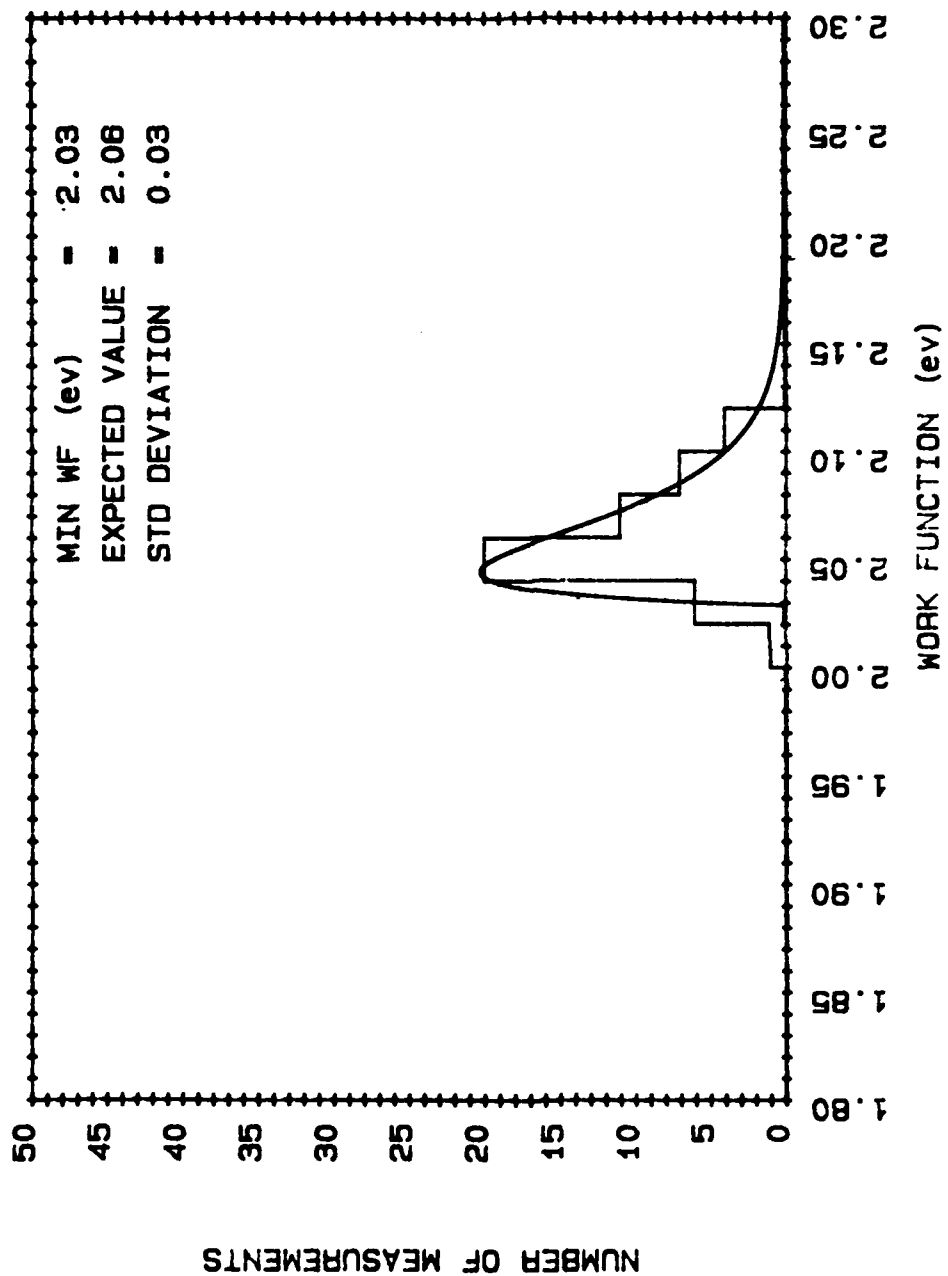


Figure 6.1-10 All S-type tungsten.

# ALL TUNGSTEN S-TYPE 5 AND 11 MICRON

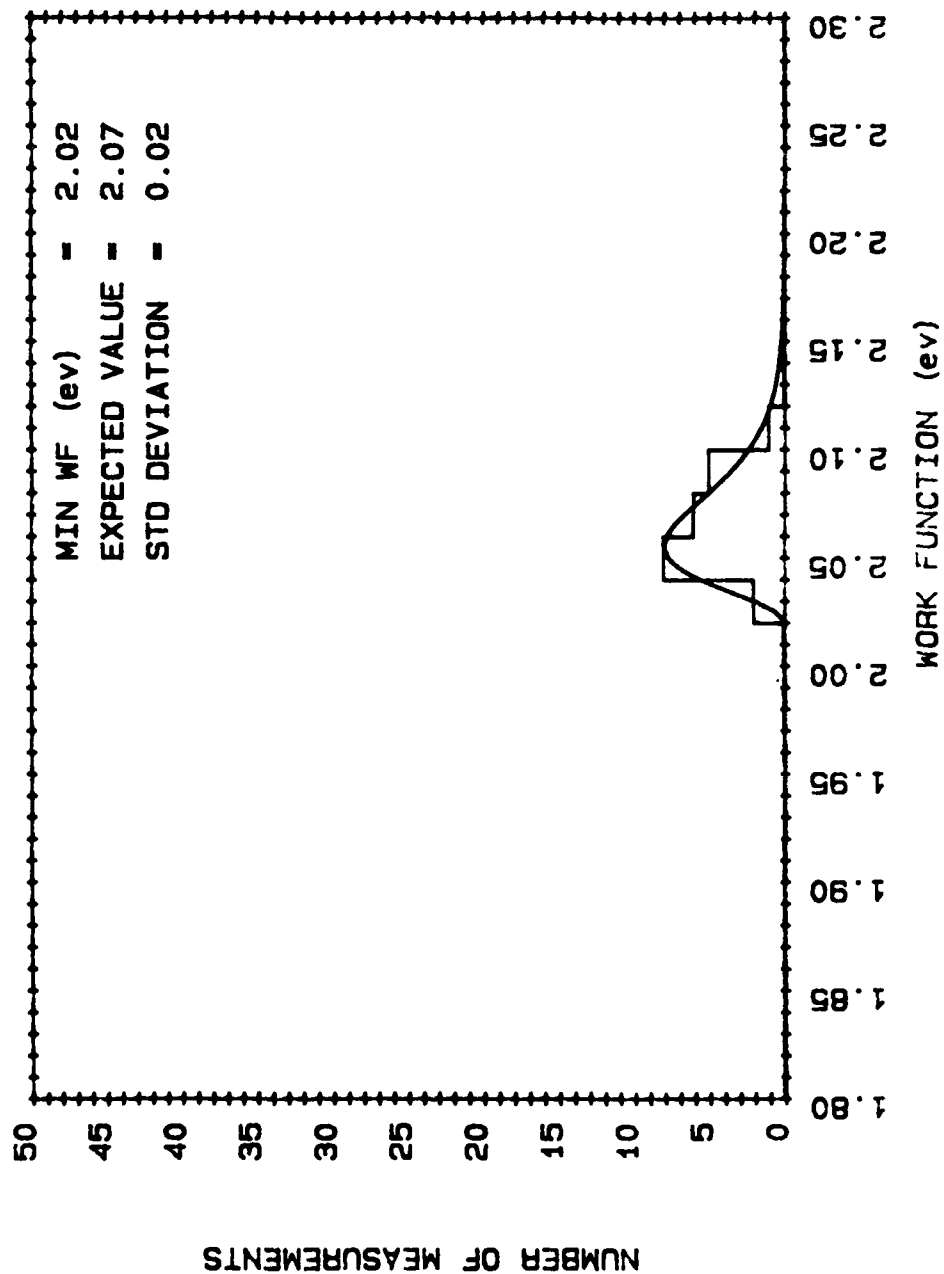


Figure 6.1-11 S-type classified tungsten.

# ALL TUNGSTEN S-TYPE UNCLASSIFIED

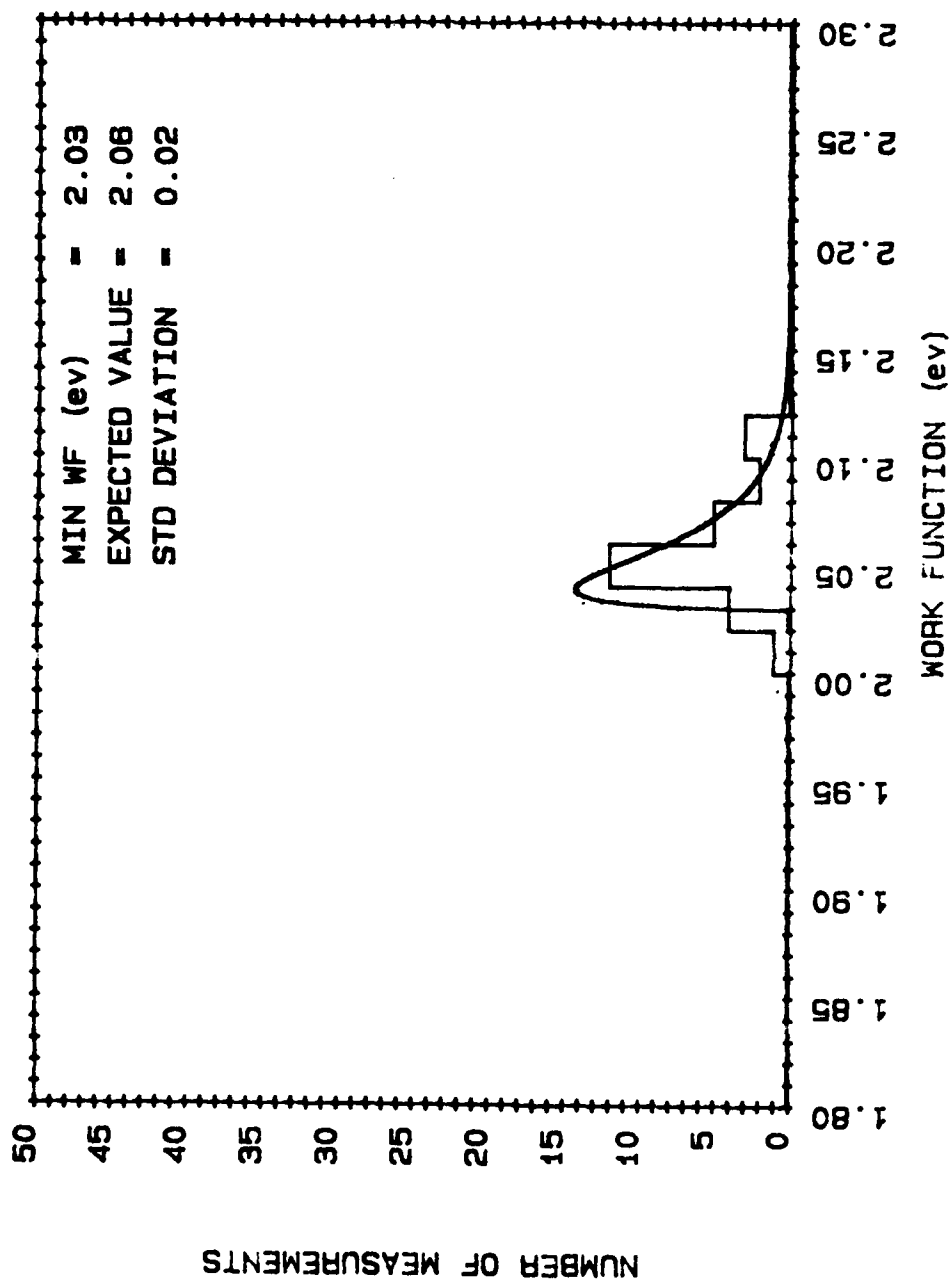


Figure 6.1-12 S-type unclassified tungsten.

# ALL TUNGSTEN B-TYPE CATHODES

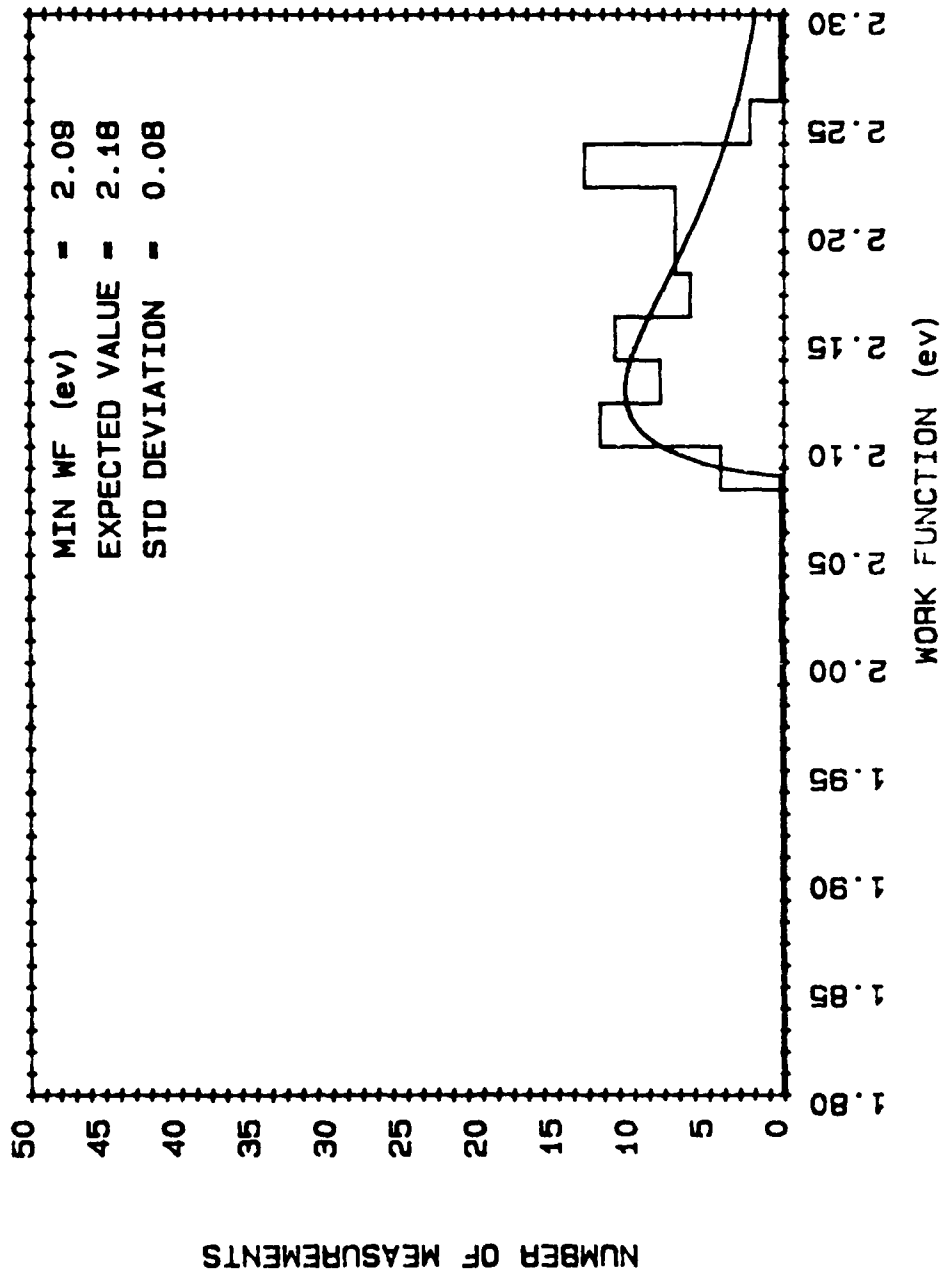


Figure 6.1-13 All B-type tungsten.

# ALL TUNGSTEN B-TYPE 5 AND 11 MICRON

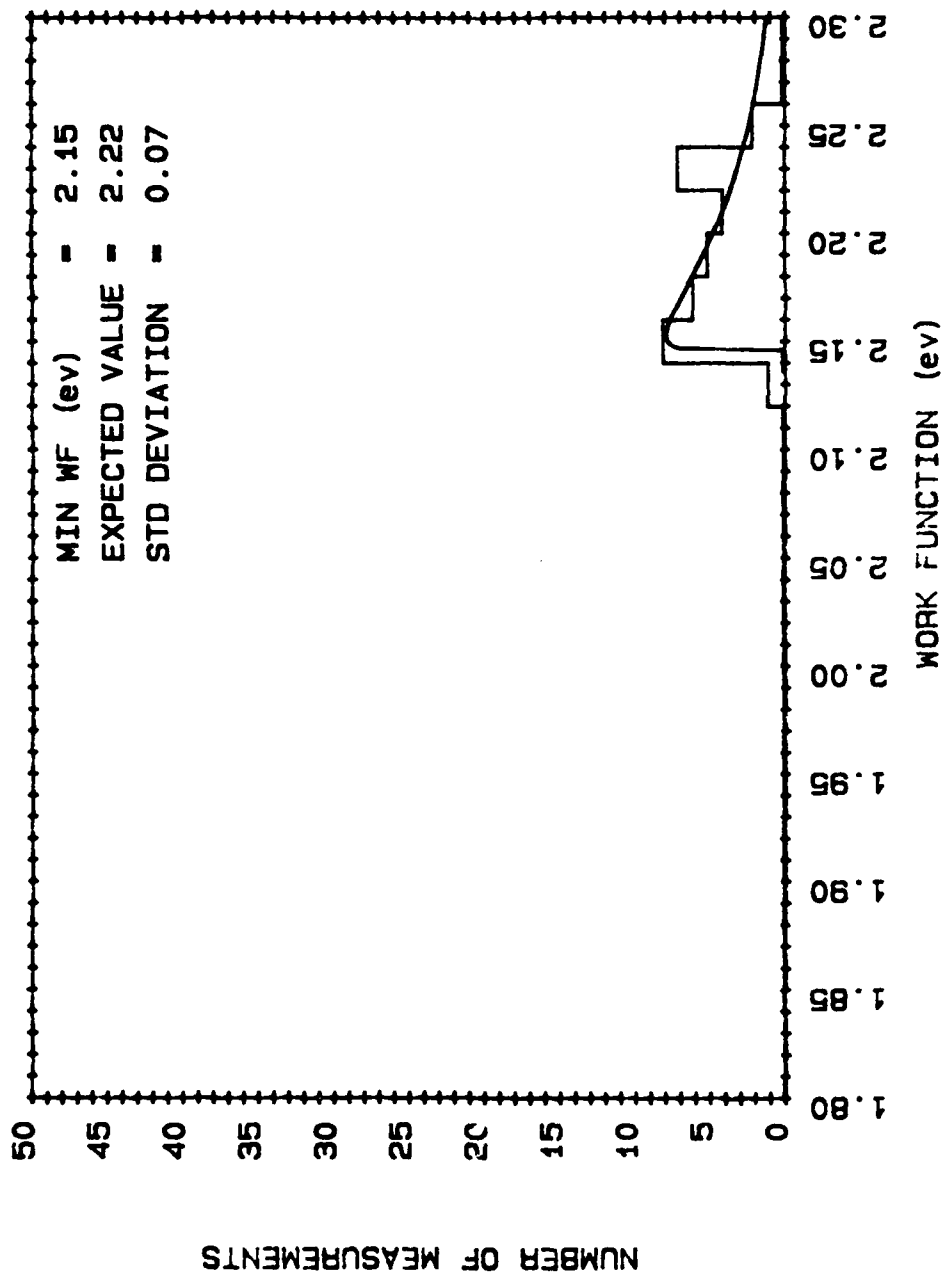


Figure 6.1-14 B-type classified tungsten.

# ALL TUNGSTEN B-TYPE UNCLASSIFIED

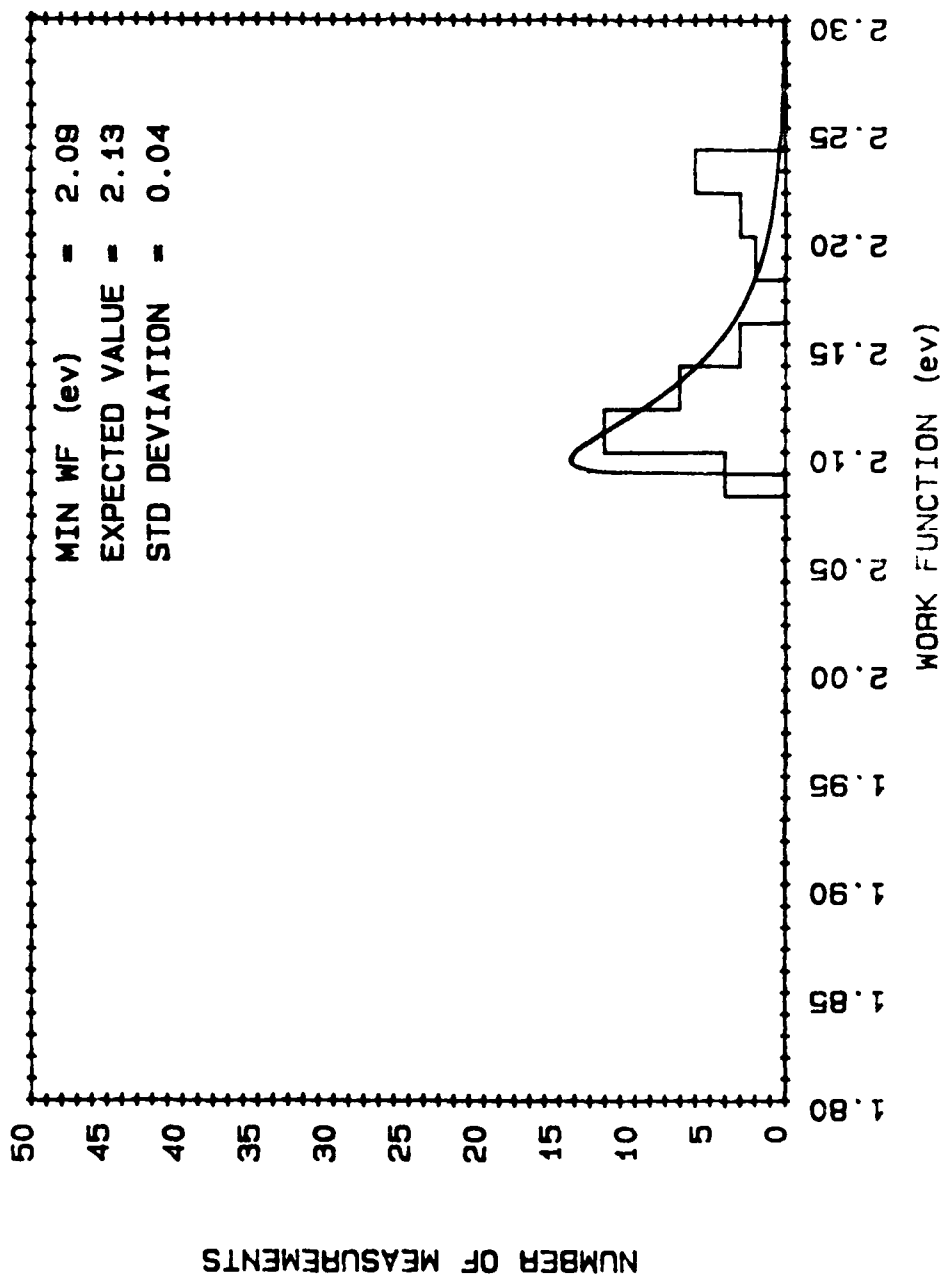


Figure 0.1-15 B-type unclassified, tungsten.



B5

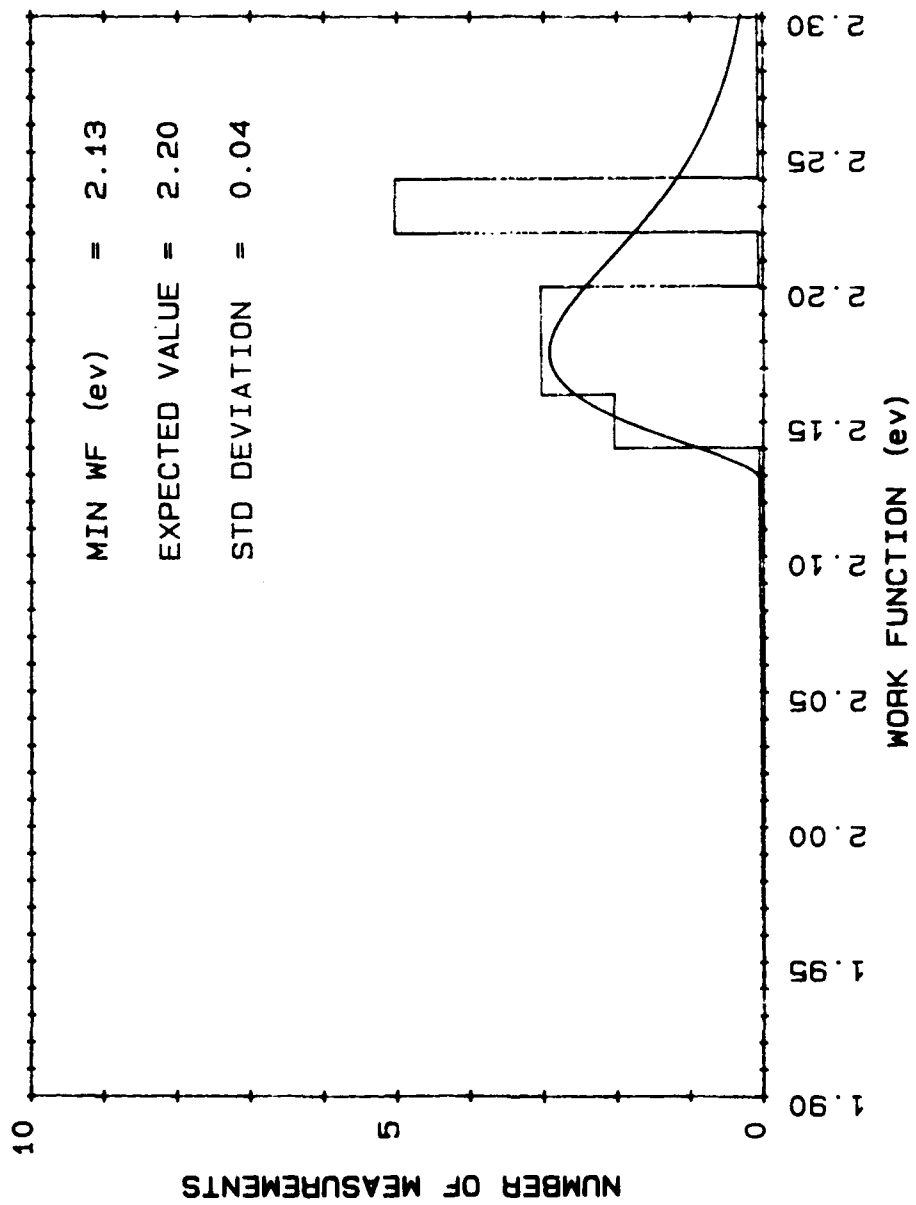


Figure 6.1-16 B-type 5 micron tungsten.

B11

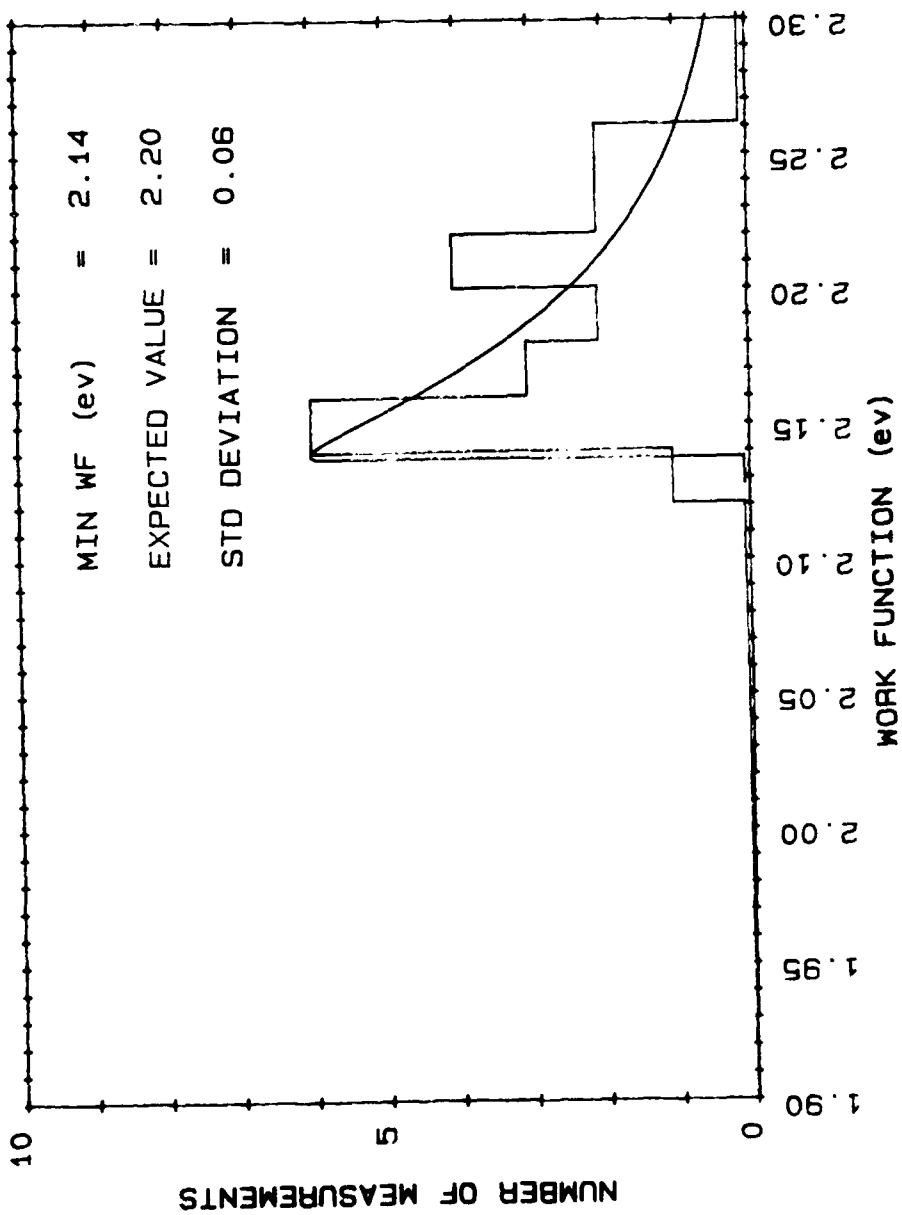


Figure 6.1-17 B-type 11 micron tungsten.

AD-A140 810

IMPROVED MATERIALS AND PROCESSES OF DISPENSER CATHODES

2/2

(U) HUGHES AIRCRAFT CO TORRANCE CA ELECTRON DYNAMICS

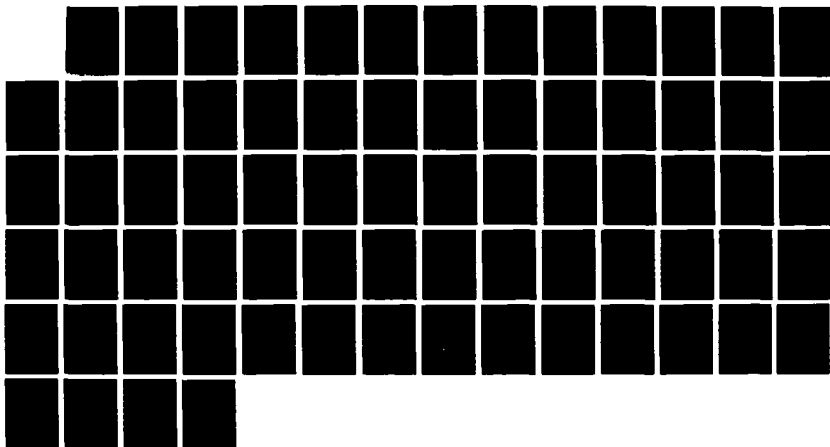
DIV R T LONGO ET AL. AUG 84 EDD-W-89514

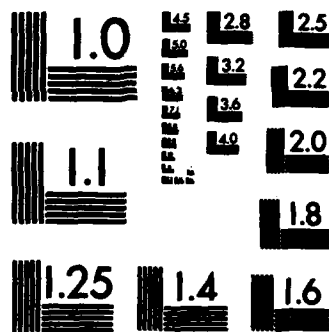
UNCLASSIFIED

AFMIL-TR-84-4072 F33615-80-C-5191

F/G 9/1

NL





MICROCOPY RESOLUTION TEST CHART  
NATIONAL BUREAU OF STANDARDS-1963-A

S5

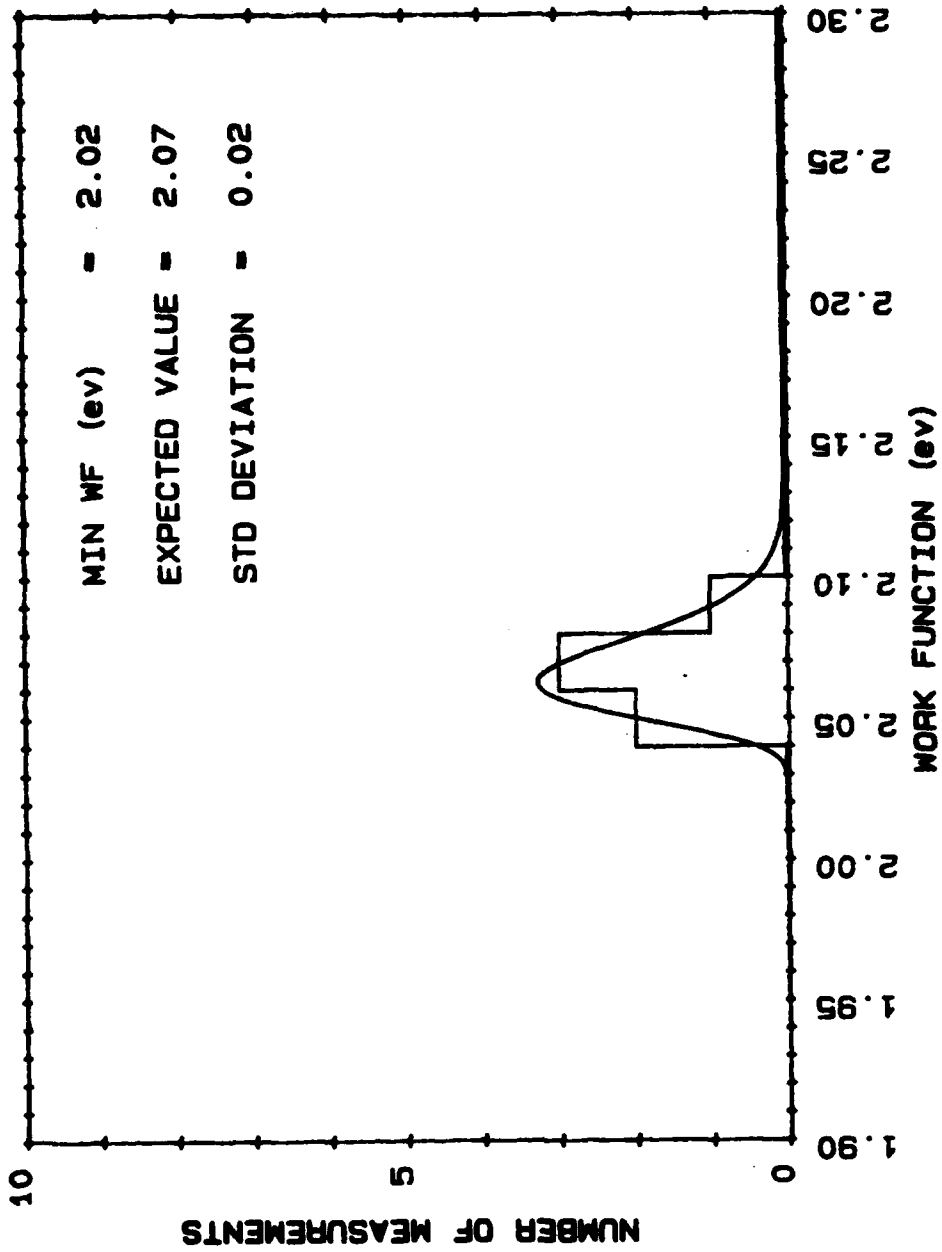


Figure 6.1-18 S-type 5 micron tungsten.

S11

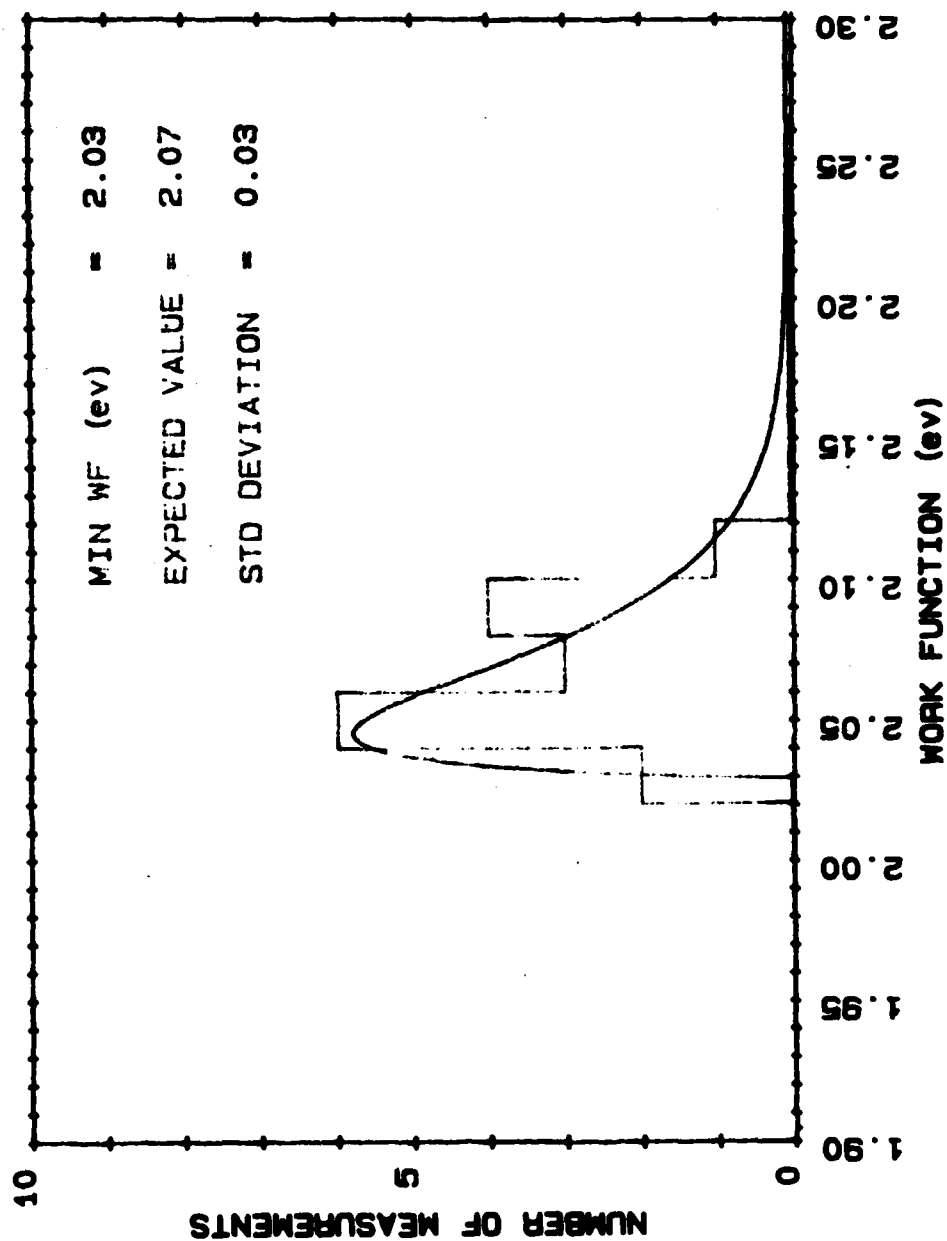


Figure 6.1-19 S-type 11 micron tungsten.

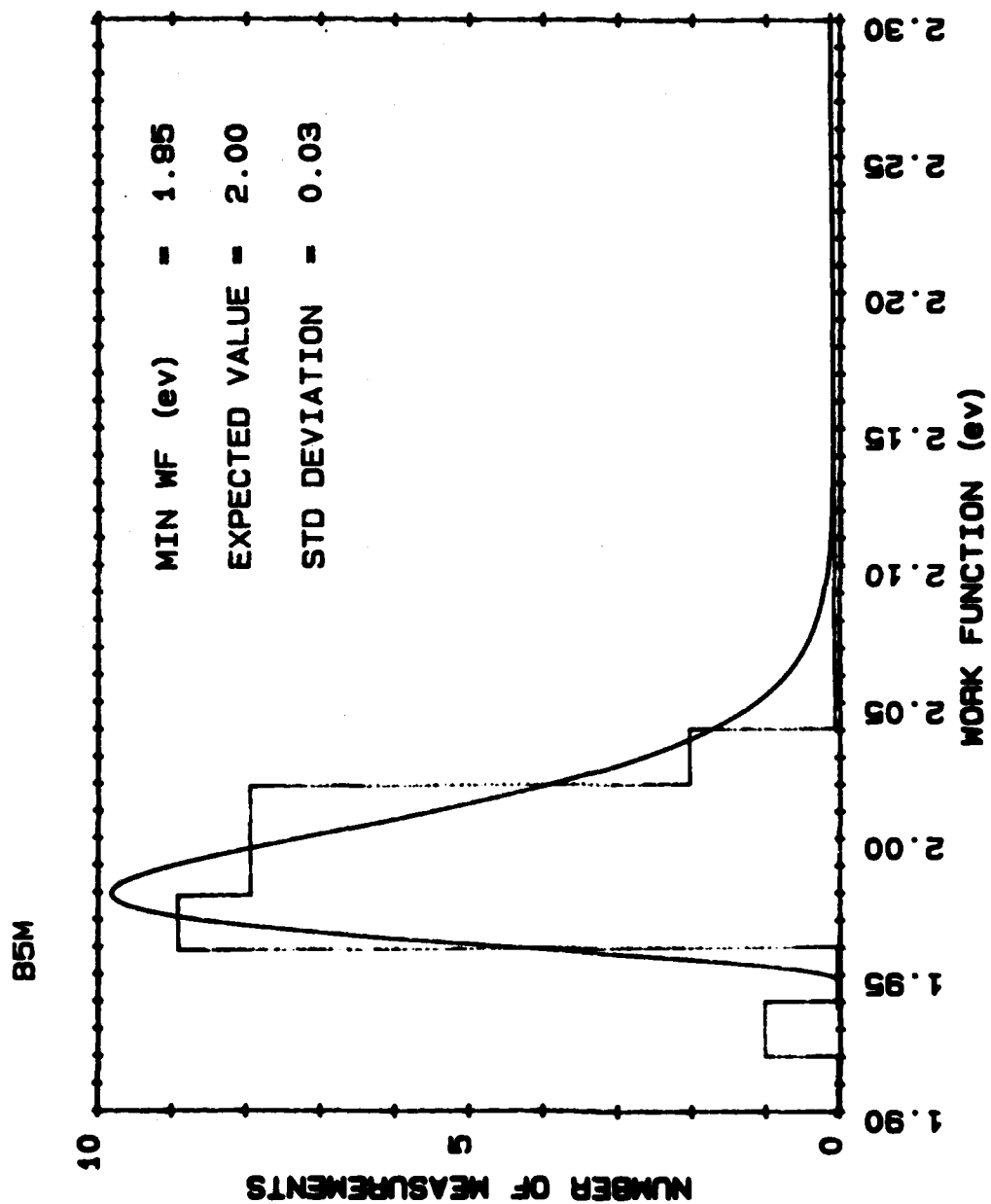


Figure 6.1-20 B-type 5 micron OsRu coated.

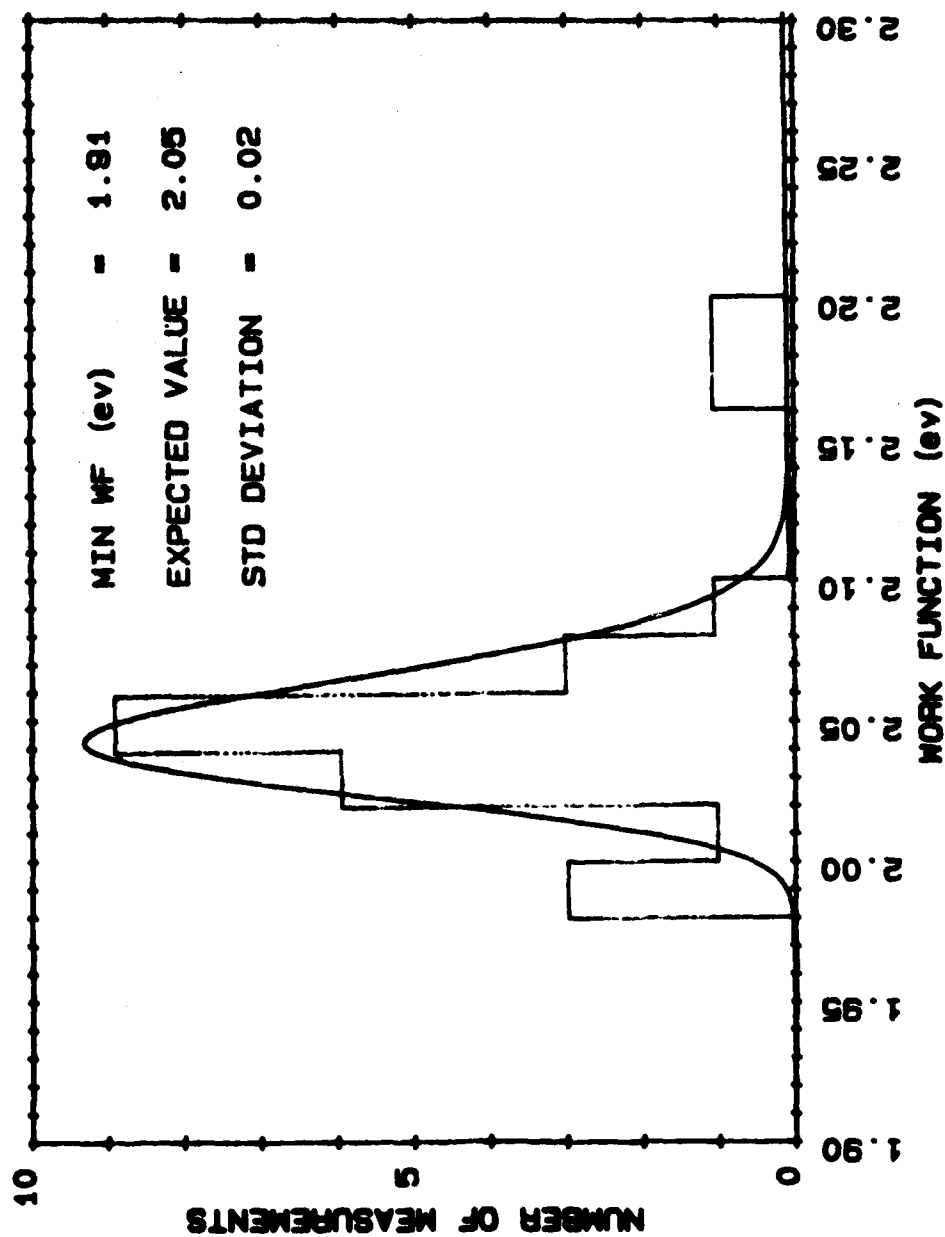


Figure 6.1-21 B-type 11 micron OsRu coated.



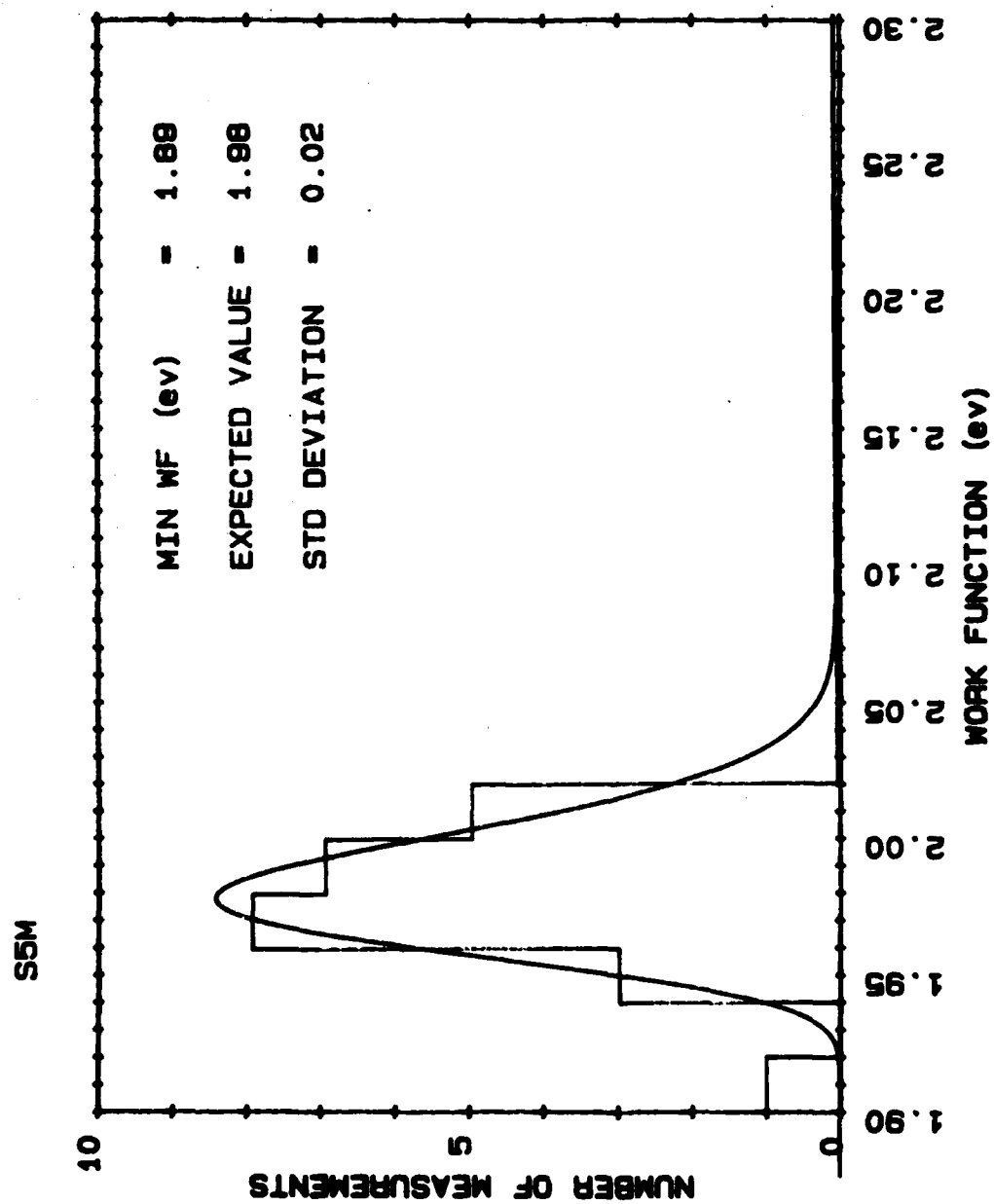


Figure 6.1-22 S-type 5 micron OsRu coated.

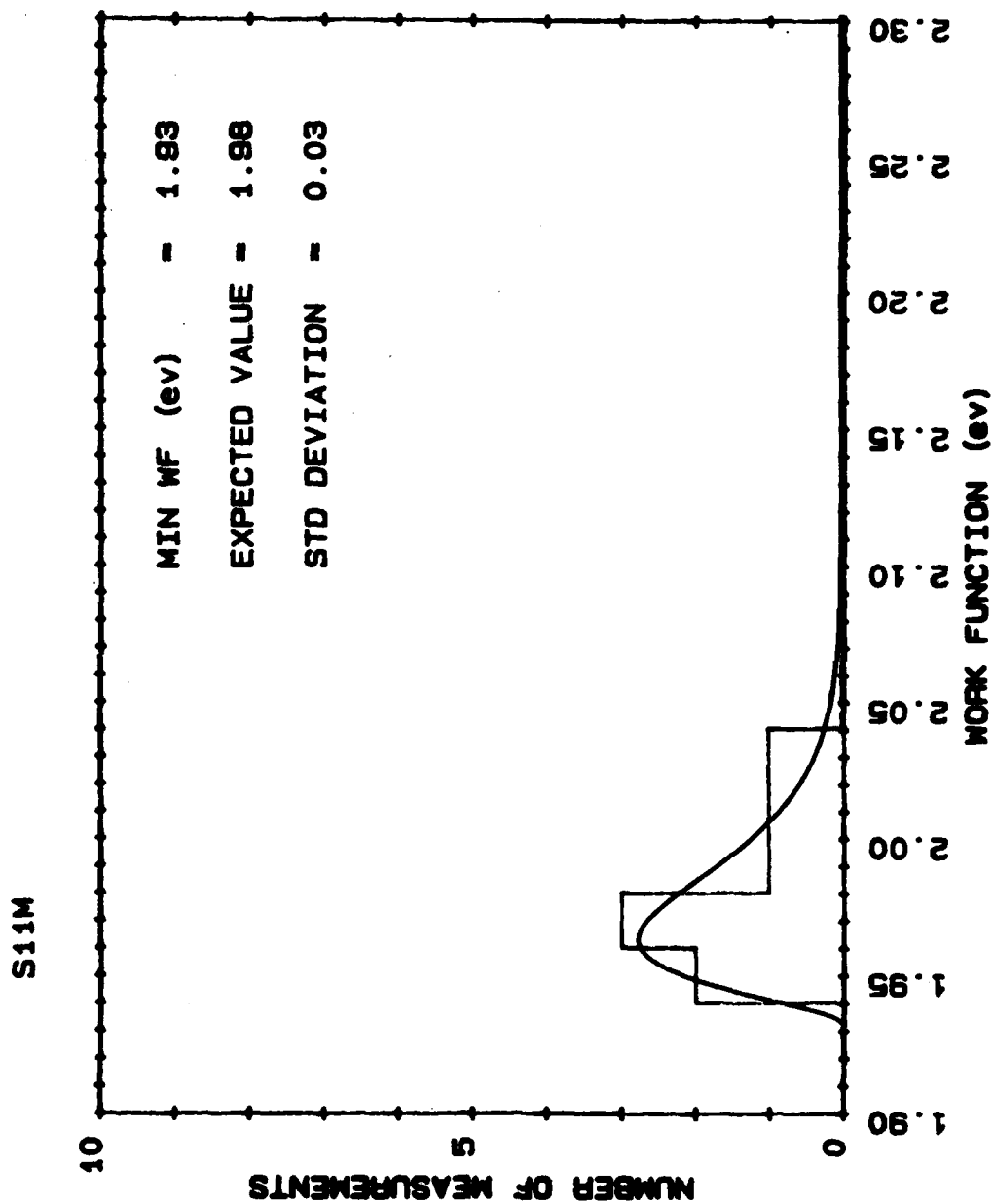


Figure 6.1-23 S-type 11 micron OsRu coated.

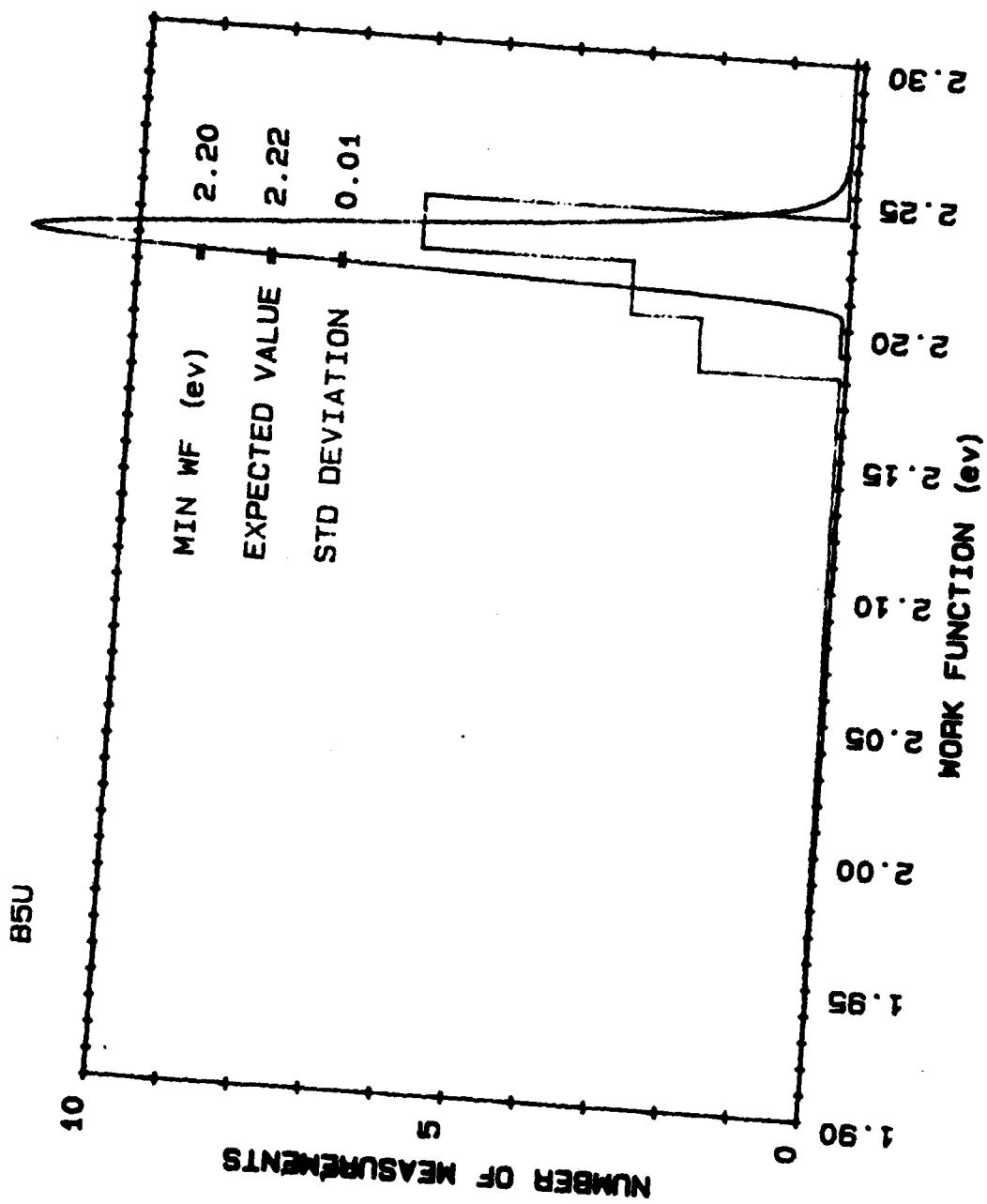


Figure 6.1-24 B-type 5 micron unclassified tungsten.

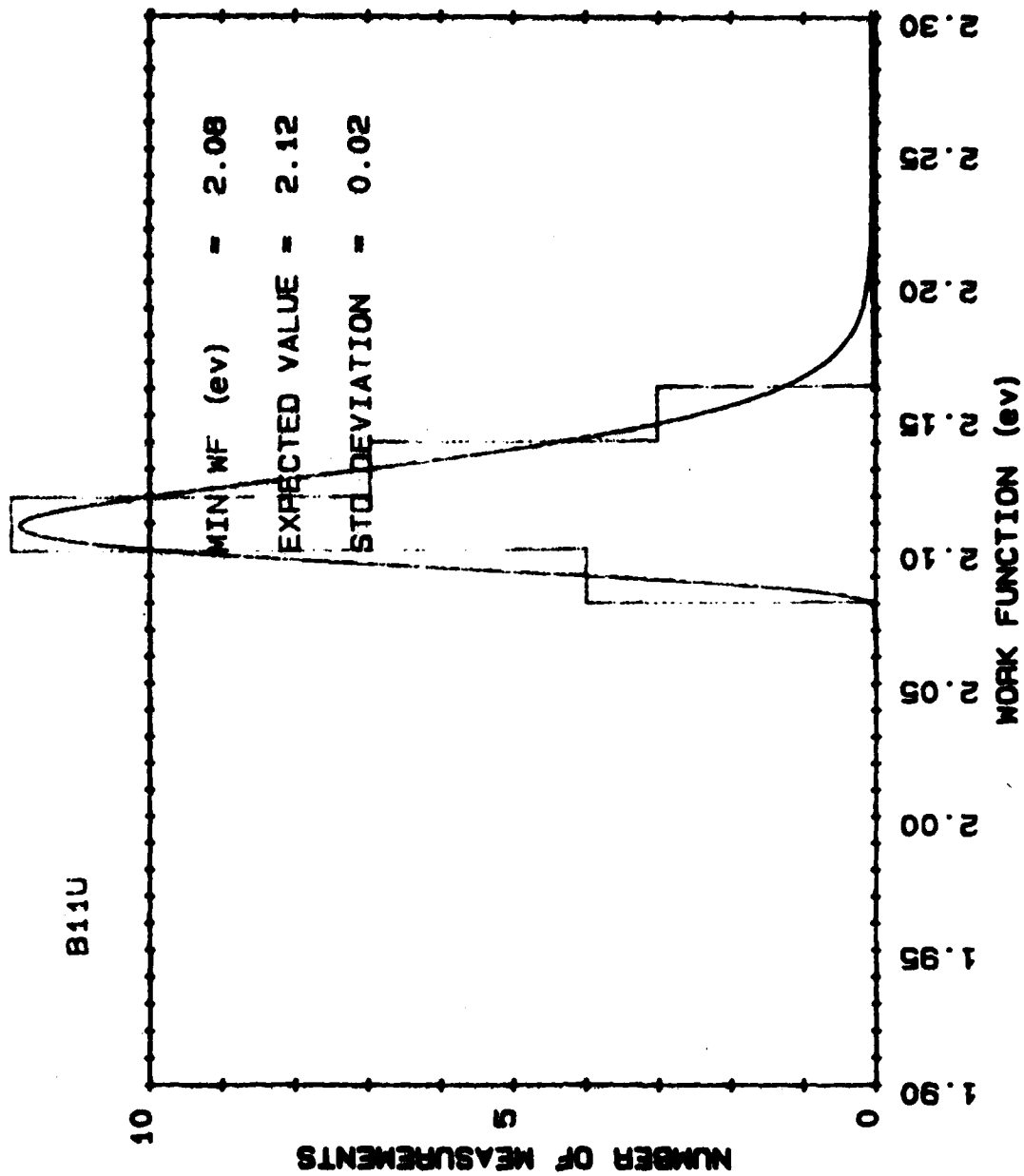


Figure 6.1-25 B-type 11 micron unclassified tungsten.

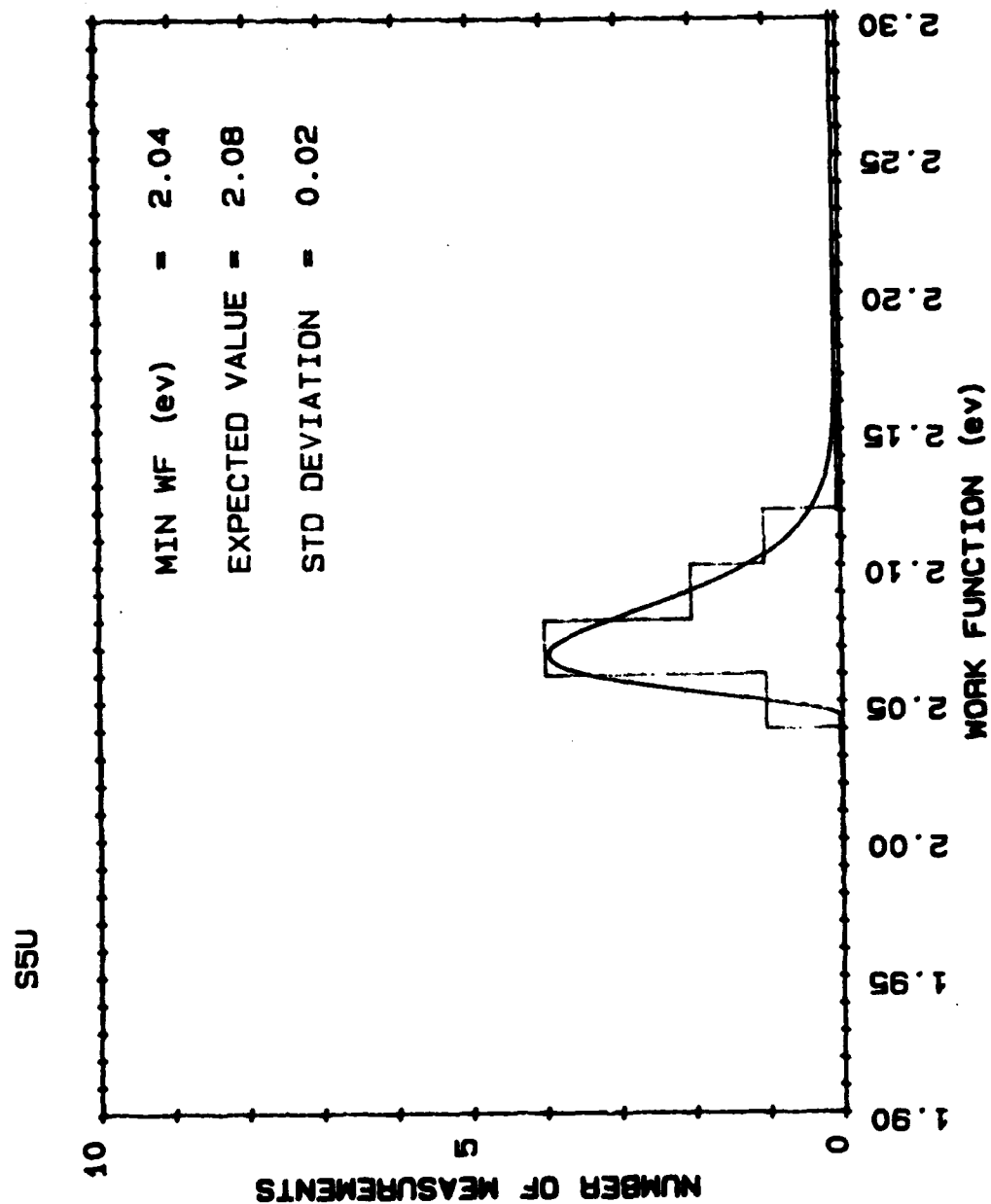


Figure 6.1-26 S-type 5 micron unclassified tungsten.

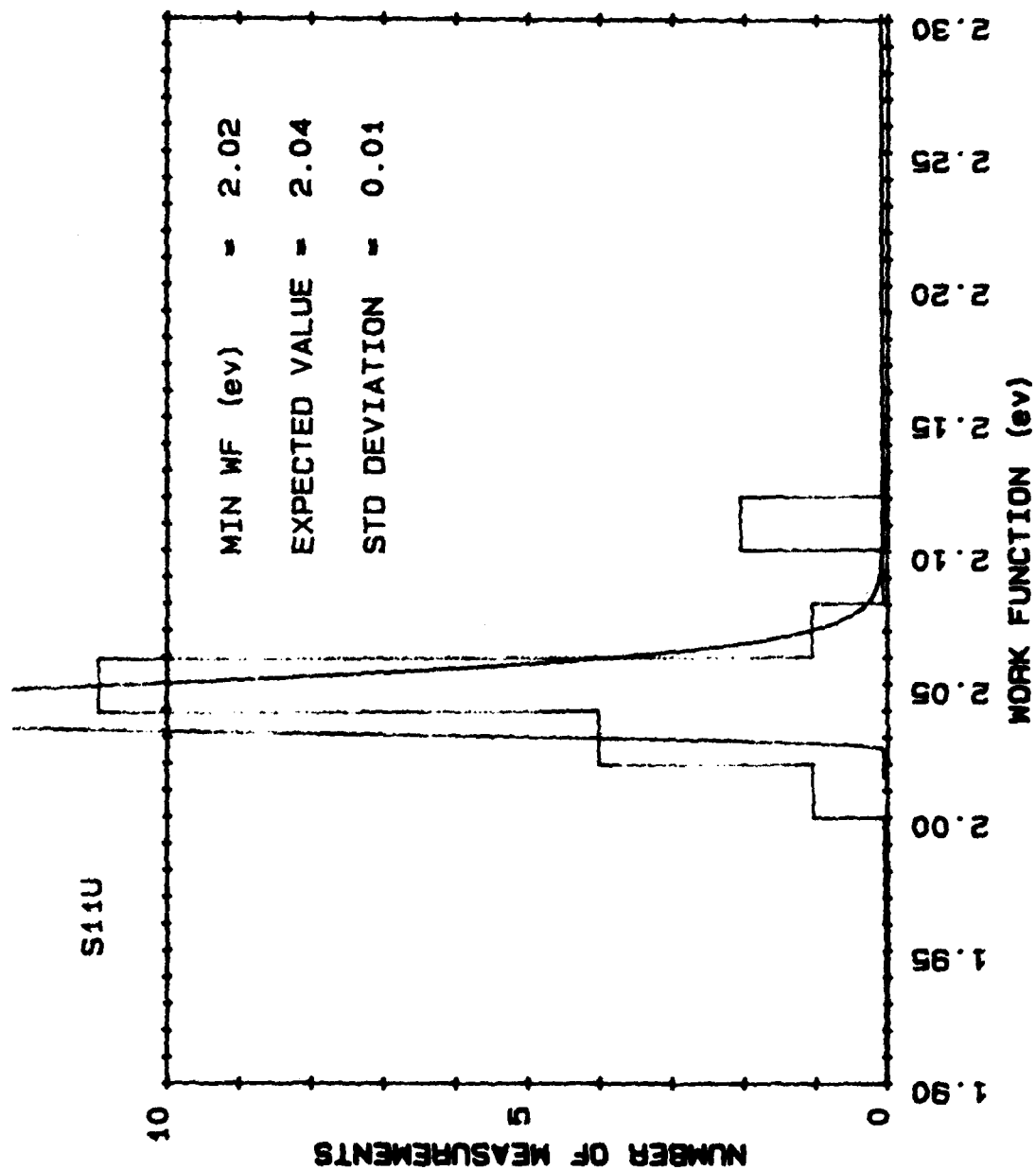


Figure 6.1-27 S-type 11 micron unclassified tungsten.

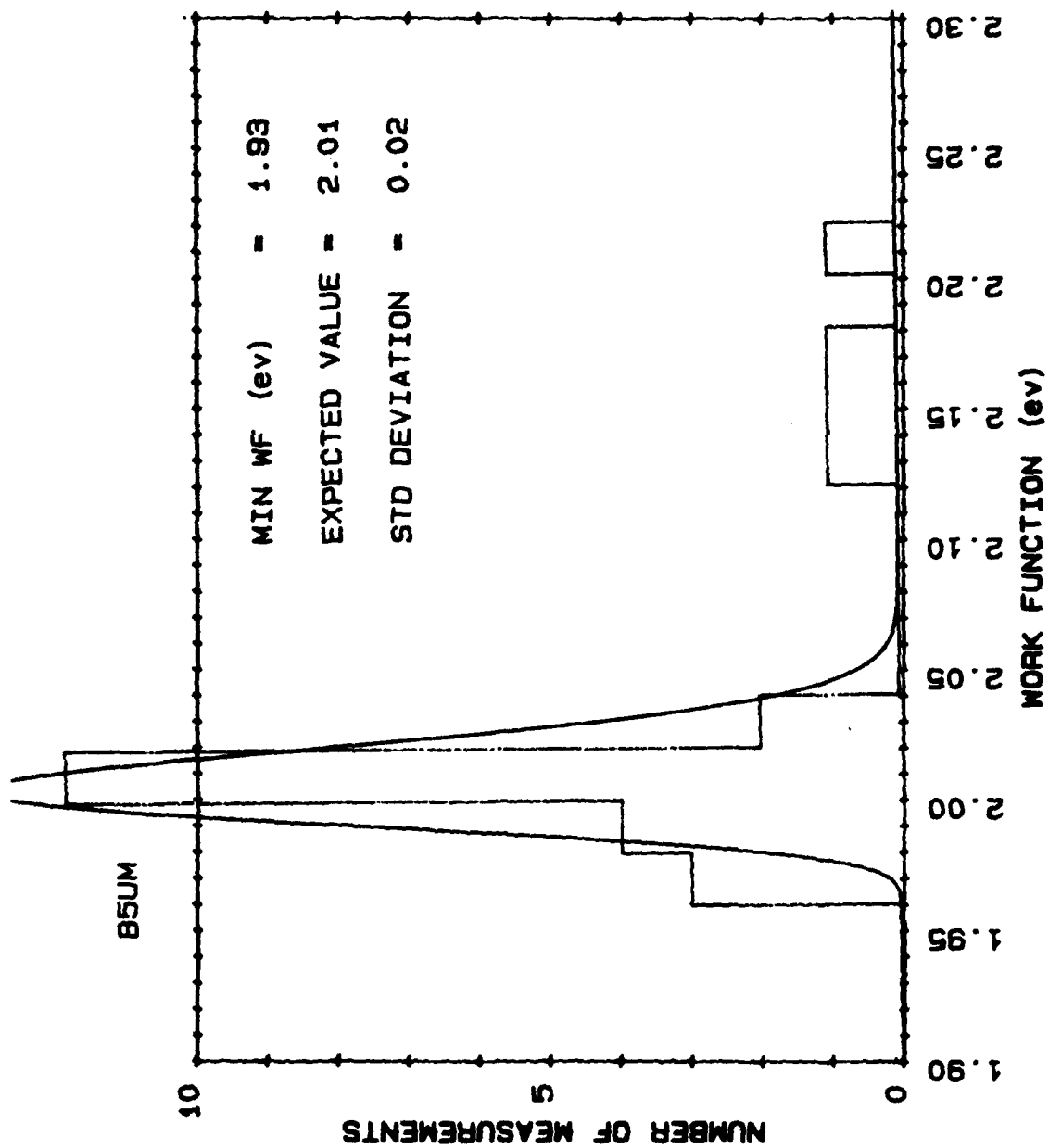


Figure 6.1-28 B-type 5 micron unclassified OsRu coated.

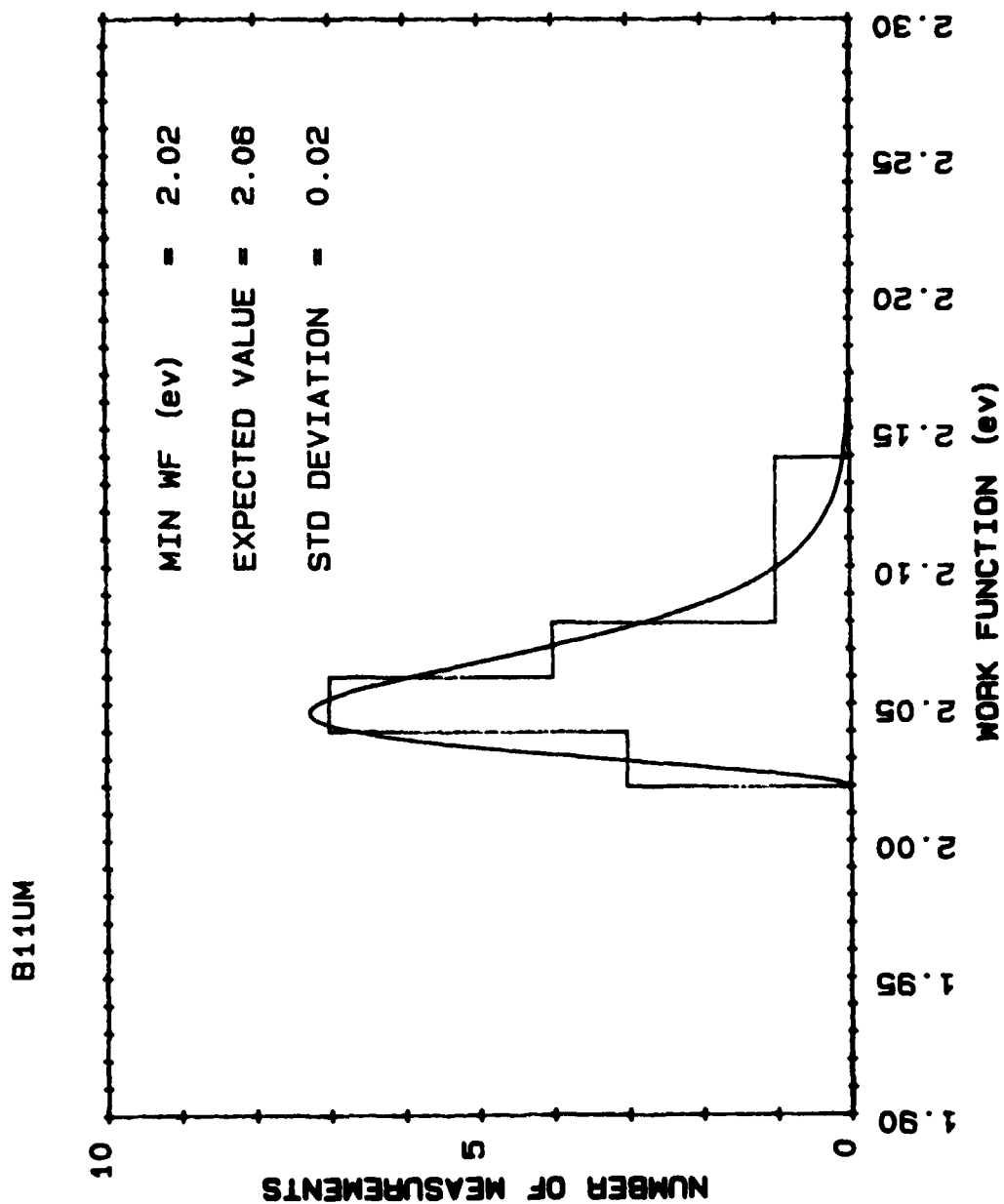


Figure 6.1-29 B-type 11 micron unclassified OsRu coated.



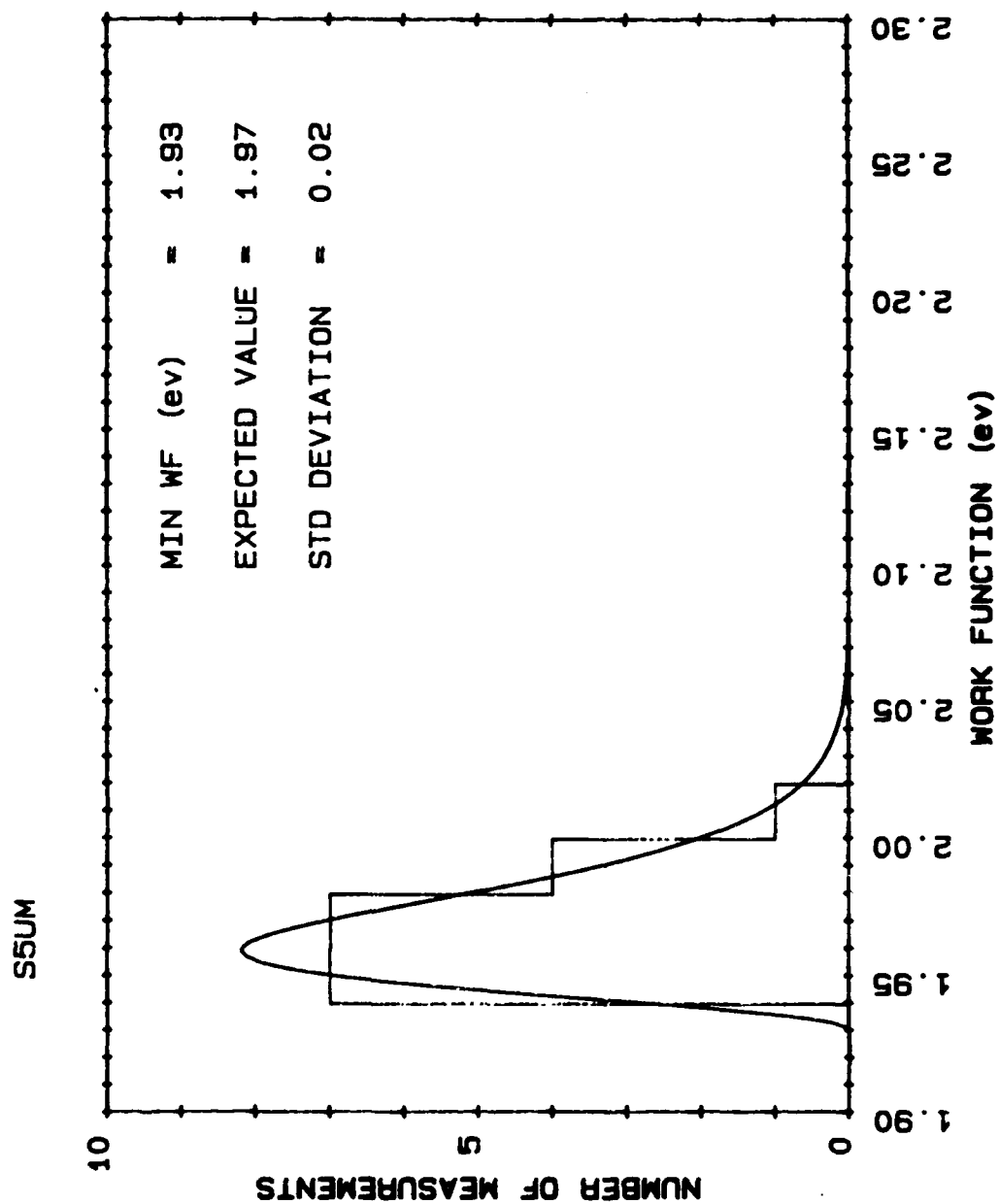


Figure 6.1-30 S-type 5 micron unclassified OsRu coated.

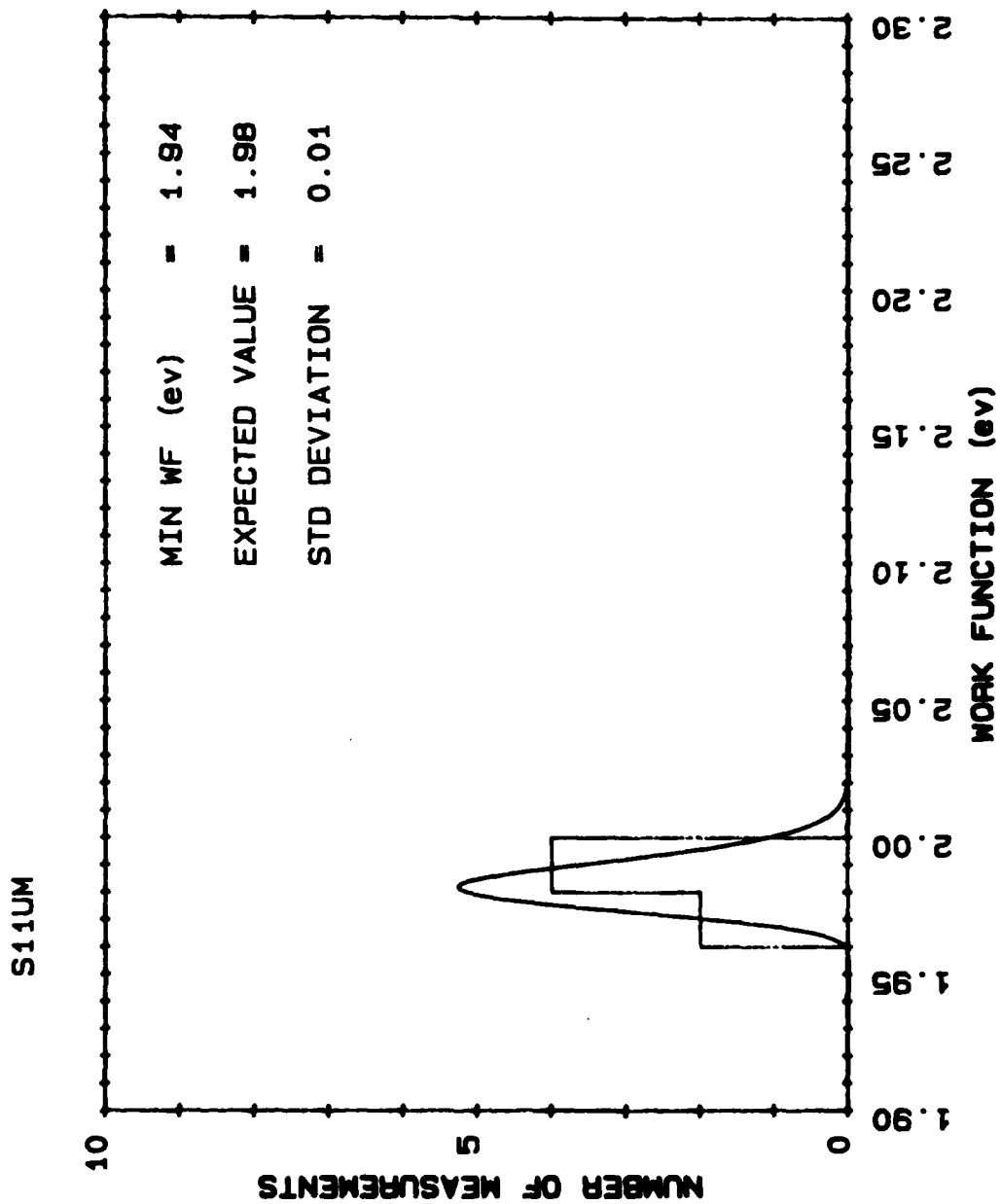


Figure 6.1-31 S-type 11 micron unclassified OsRu coated.

## 6.2 BARIUM EVAPORATION

Barium evaporation measurements were made on all the powder classified samples in the experimental matrix. The evaporation rates were measured at several different temperatures and are given in Appendix B. The evaporation rates behaved in the expected way, i.e.,

$$R(T) = R_0 e^{-\epsilon/T} . \quad (6.2-1)$$

Table 6.2-1 gives the values of  $\ln R_0$  and the activation energy  $\epsilon$  for each of the classified samples in the matrix.

## 6.3 DEPENDENCE OF WORKFUNCTION ON EVAPORATION RATE

Now that we have the evaporation rate and workfunction parameters for the statistics (see table 6.1-1 and 6.2-1) we can ask how the two are related. Figure 6.3-1 is a plot of the expected workfunction vs the evaporation rate taken at 1323°K (1060°C<sub>T</sub>). Figure 6.3-2 gives the minimum workfunction obtained from the gamma distribution plotted vs barium evaporation rate.

These two figures suggest that if we could go far enough out in the evaporation rate\* the tungsten and the Osmium:Ruthenium cathode would reach the same value. This is a surprising result. It suggests that the difference between the Tungsten surface cathode and the Osmium Ruthenium surface cathode is just due to the sticking time of the dipoles. We shall test this in the modelling section, (Section 7).

---

\* The use of the term "evaporation" rate is a misnomer. We are not talking of the rate at which barium leaves the surface but the total rate at which barium leaves the cathode pellet (mostly directly from the pores).

TABLE 6.2-1  
PARAMETERS OF BARIUM EVAPORATION MEASUREMENTS

	B-TYPE (5: 3: 2)	S-TYPE (4: 1: 1)
	5      11	5      11
UNCOATED		
ln ( R )	31.42   28.23	29.27   29.48
ACT.ENERGY	3.94    3.51	3.48    3.53
COATED		
ln ( R )	37.02   33.24	26.62   27.23
ACT.ENERGY	4.64    4.23	3.15    3.17

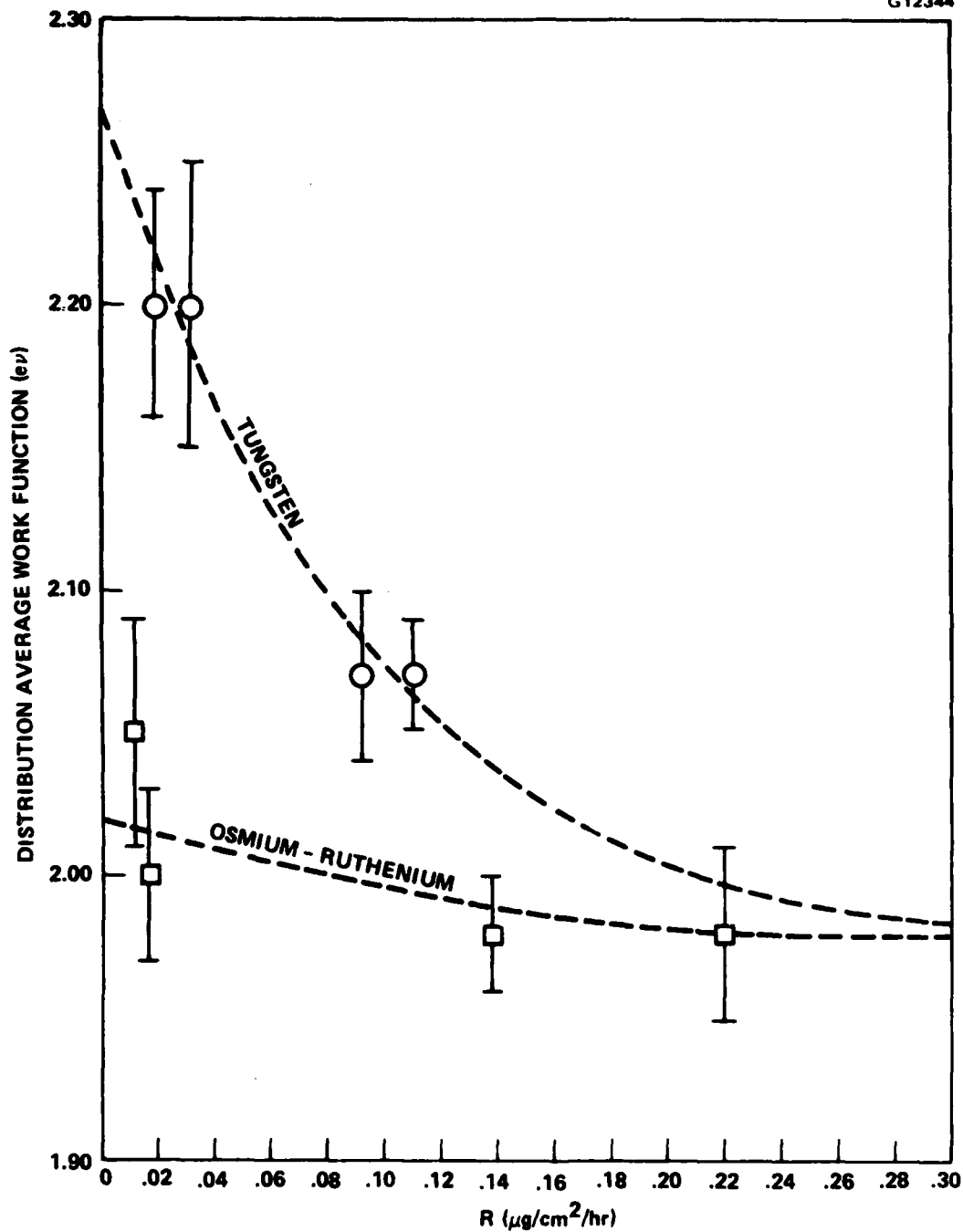


Figure 6.3-1 The expected value of the work function vs barium evaporation rate.

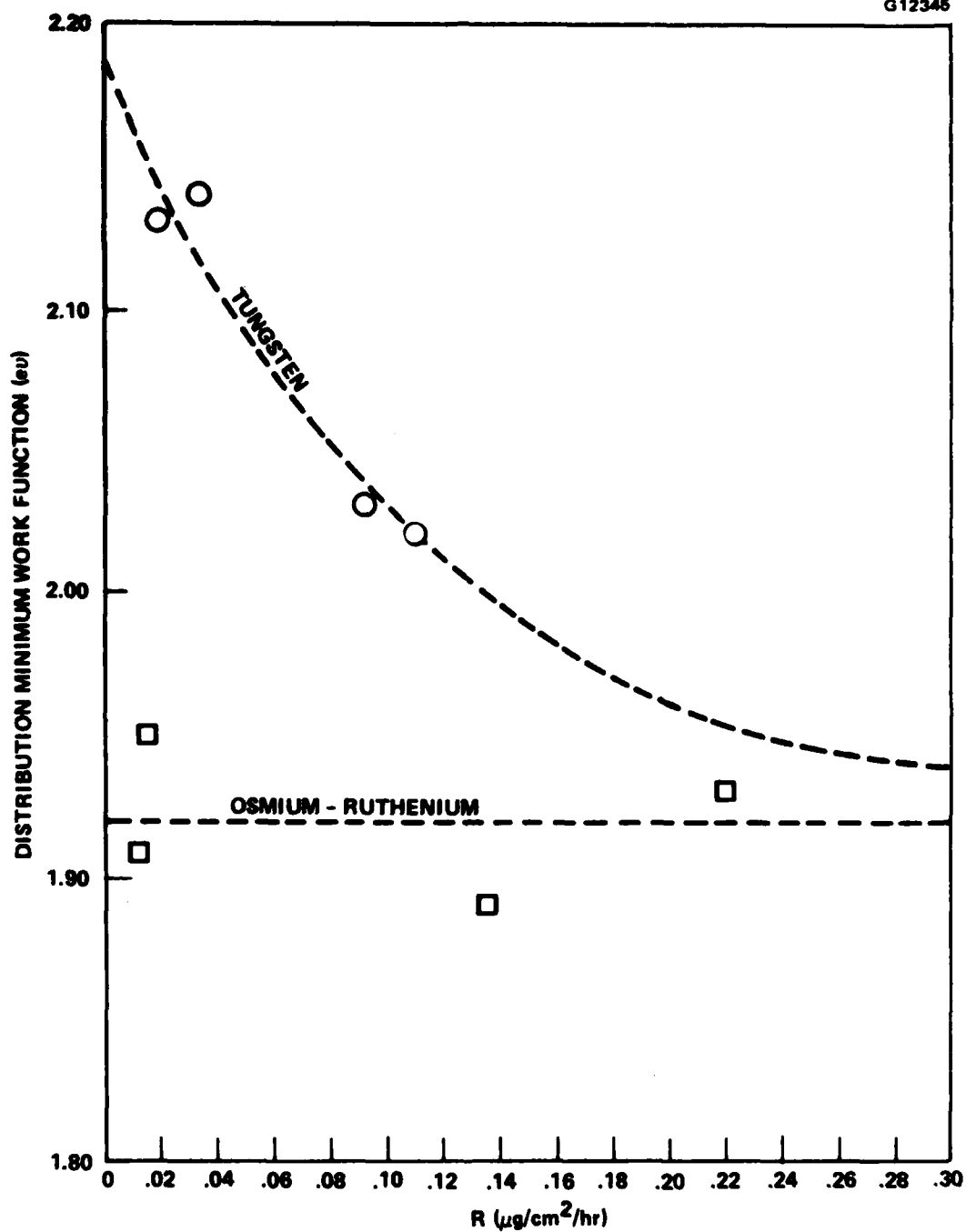


Figure 6.3-2 The minimum value of the work function vs barium evaporation rate.

If we take the lowest values in Table 6.1-1 we can fit the data to an exponential. We obtain

$$\langle \phi \rangle = 1.98 + 0.29 e^{-11.2R} \quad (6.3-1)$$

for tungsten, and

$$\langle \phi \rangle = 1.98 + .04 e^{-16.2R} \quad (6.3-2)$$

for Osmium:Ruthenium. R is the evaporation rate in units of  $\mu\text{gm}/\text{cm}^2/\text{hr.}$

For the minimum workfunction we obtain

$$\phi_m = 1.92 + .27 e^{-9.32R} \quad (6.3-3)$$

for tungsten, and

$$\phi_m = 1.92 \quad (6.3-4)$$

for Osmium:Ruthenium.

#### 6.4 EFFECTS OF IMPURITIES

As we noted in Section 4.3, our attempt to maintain high purity was not entirely successful. Sulfur contamination entered our material from the lot of  $\text{BaCo}_3$ . The question we must address is what effect this level of sulfur has on our experiment.

There are a number of independent pieces of information we can add to help draw some conclusions. The first question we must ask is how do our workfunctions compare with other independent measurements. To answer this question we must be careful. Our analysis techniques differ from those reported by others. A study of appendix A will clarify the differences. An industry standard for the workfunction of these kinds of cathodes in terms of a well defined distribution does not exist.

Earlier work at HEDD on close spaced parallel plate diode life tests is available and is useful here because of the similarity of the test vehicle and the same analysis technique was used (i.e., the empirical formula equation A-1). Figure 6.4-1 shows the results of many tests taken over a period of 4 to 5 years that include all manufacturers. Included in the distribution are all tungsten surface cathodes both (4:1:1) and (5:3:2). Table 6.4-1 provides the code to the various manufacturers. Each symbol represents a particular measurement on a given cathode. For example, the letter "F" represents a cathode from Philips.



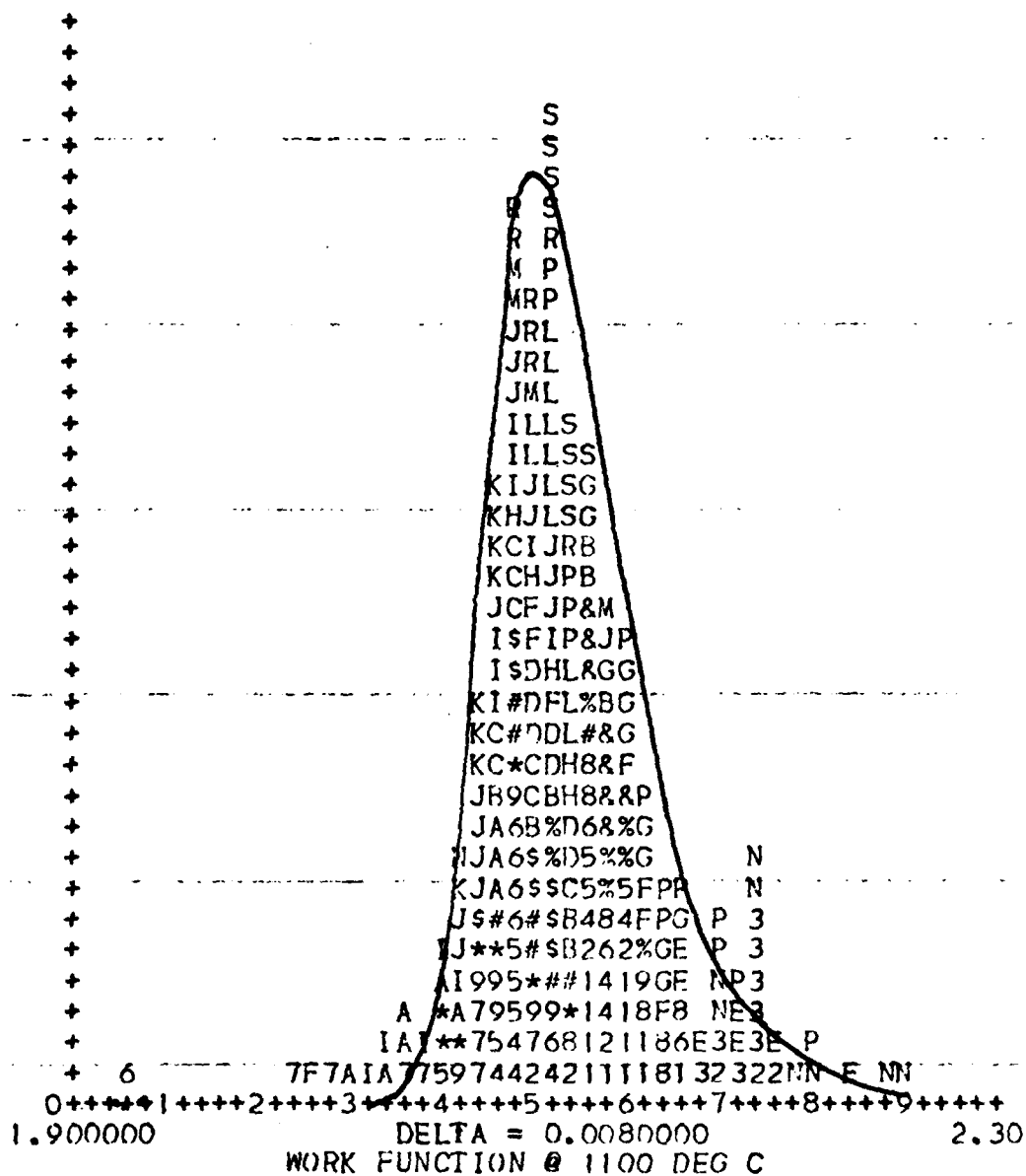


Figure 6.4-1 Histogram of HEDD life tests. The solid line is a gamma function with parameters  $\phi_{\min} = 2.028$  ev, expected value = 2.13 ev and standard deviation = 0.04 ev.

TABLE 6.4-1  
TUNGSTEN SURFACE DISPENSER CATHODES  
(All data obtained before 1980)

Manufacturer	I.D.Code given in Figure 6.4-1										
HEDD	1	2	3	4	5	6	7	8	9	*	#
	\$	%	S								
Philips	D	E	F	G							
Spectromat	N	P	R	S							
Semicon	H	I	J	K	L	M					
Komeko	A	B	C								

A couple of things should be mentioned about the data given in Figure 6.4-1.

1. The vehicle was a close spaced parallel plate diode with a flip anode, which was moved away from the cathode during the aging period and moved into place for the measurements. The positioning of the anode was by gravity. The vehicle was patterned after the early vehicle used by Philips.

The movable anode did introduce spacing variation from measurement to measurement which our analysis technique was reasonably effective in removing. However, the analysis cannot completely eliminate this scatter.

2. The temperature was measured with an optical pyrometer by sighting on the molybdenum body attached to the cathode pellet. All measurements were made at 1100°C brightness on molybdenum.

The distribution, Figure 6.4-1, shows the same effect as we observed in this program, namely a gamma distribution type behavior, i.e., a sharper leading edge (i.e., at low workfunction) and a larger tail on the high workfunction side. A reasonable gamma function fit to the distribution yields an expected value of 2.13 ev with a standard deviation of 0.04 ev and a minimum value of 2.03 ev.

This distribution should be compared with Figure 6.1-2 for all tungsten uncoated cathodes.

The expected value is not significantly different, 2.13 ev versus 2.15 ev. That is within the standard deviation of the smallest distribution. Similarly, the minimum values are effectively the same. The width or standard deviation of the two are considerably different; the standard deviation of this work being 0.1 ev, whereas for the life test it is 0.04 ev.

One major difference that we must keep in mind when comparing Figure 6.1-2 with Figure 6.4-1 is lengths of time that the cathodes were run. In this program the maximum time was 200 hours. In the life test data, Figure 6.4-1, the measurements ranged up to 2000 hours. In the early life test we did notice a tendency for the distribution to narrow with age.

A second piece of data which is more directly related to this program comes from several life tests that were run using the lot 12 aluminate material of this program.

Three M-type cathodes were made from some excess aluminate powder, lot 12, along with three M-type cathodes of lot 9 and four M-type cathodes from lot 14. See Table 4.3-3 for identities. All of this cathodes have accumulated approximately 3000 hours to date.

Figure 6.4-2 shows the average workfunction versus time. This data clearly shows the effects of sulfur, lot 14, being the purest.

The life tests, however, do not show a distinction between lot 12 (this program material) and lot 9 (effectively industry standard material). This suggests that the narrower distribution seen in Figure 6.4-1 might be age related instead of sulfur related.

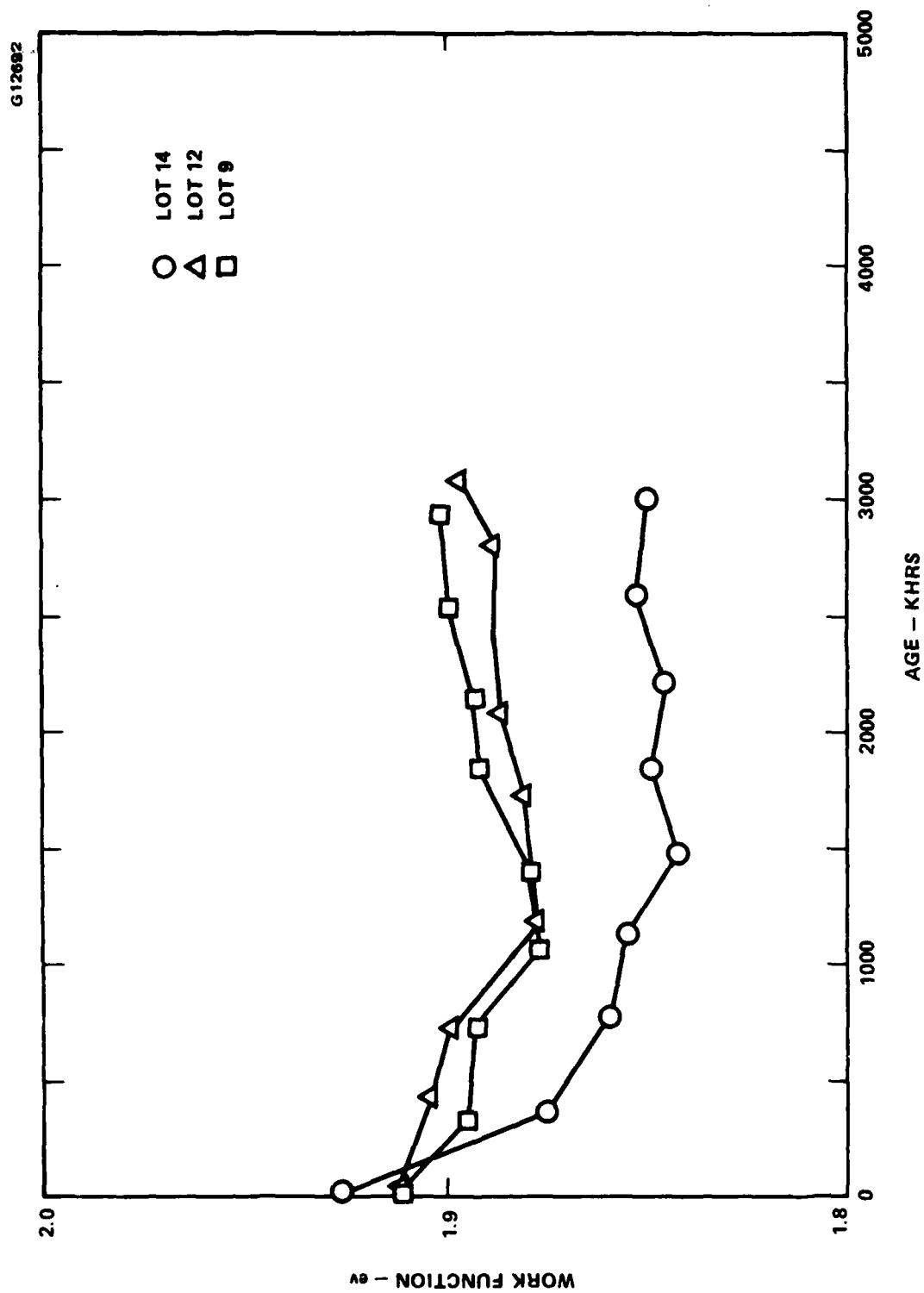


Figure 6.4-2 Life test results in a 877HA Pierce gun vehicle.

Several other observations must be made:

1. We should observe that all three lots (i.e. 9, 12 and 14) yielded effectively the same results for the first couple of hundred hours of their life; deviation becoming apparent only after aging.
2. The difference in the value of the workfunction enters because of the totally different geometry of the device. In this work and the early life test results of Figure 6.4-1, the vehicles were close spaced parallel plate diodes. In the life test results, given in Figure 6.4-2, the vehicles are Pierce gun geometry (877 HA devices). The empirical formula (equation A-1) was applied in all cases, however, it is not correctly applied in the Pierce gun cases (i.e., the geometric factors are not correctly accounted for). This leads to a systematic discrepancy in the value of the workfunctions.

## 7.0 THEORETICAL MODELING OF THE DISPENSER CATHODE

In this section we shall undertake to construct one of possibly many models for the dispenser cathode. The modeling that we will undertake here, we believe is consistent with the data taken in this program.

When one undertakes the task to construct a model based primarily on one set of data, it must be kept firmly in mind that the attempt is no more or no less than a way of summarizing that set of data into a simpler set of mathematical equations.

The mathematical equations of the model may be simply mathematical fits to data without underlying physical support, or we might give some physical arguments which provide form to the equations (e.g., many processes in thermodynamics behave via  $e^{-\epsilon/T}$ , so we might guess this form when temperature effects are considered).

The models presented here must be viewed more as engineering constructs than as basic physical models.

With these ideas in mind we shall begin to fold the data set into some mathematical forms, ending up with equations that are consistent with the data set and yielding the ability to interpolate within that set.

Attempts to extrapolate these equations beyond the bounds of the data set are very risky.

More rigorous first principle models are not yet possible with the present understanding and the present data.

Perhaps as data becomes available from surface analysis and other techniques that yield atomic information, a more rigorous physical theory can be generated.

In the models developed in this section we will make the assumption that the workfunction is a dependent variable, derivable from other effects such as barium evaporation rate and dependent upon such effects as the surface sticking time of the dipoles on the emitter surface.

Before we can begin to construct such a model we must discuss several preliminary effects.

### 7.1 EVALUATION OF EMISSION CURRENT

The data that was taken in this program was current-voltage-temperature-spacing (I-V-T-D) measurements. In order to extract the cathode properties from these measurements, we must assume some model of how the measurable parameters (i.e., I-V-T and D) vary with the more fundamental properties of the cathode (i.e., its workfunction). In Appendix A we have discussed several ways of evaluating the I-V-T-D data and the advantages and disadvantages of each.

In the modelling that we will construct in this section we will assure that the I-V-T-D curves can be sufficiently described by

$$\frac{1}{J} = \frac{1}{J_{SC}} + \frac{1}{J_{TL}} \quad (7.1-1)$$

where

$$J_{SC} = \frac{2.33 \times 10^{-6}}{d^2} V^{3/2} \quad (7.1-2)$$

and

$$J_{TL} = AT^2 e^{-11600\phi/T} e^{4.4\sqrt{V/d}/T} \quad (7.1-3)$$

All of the cathode information is obtained in the workfunction  $\phi$  and the Richardson constant  $A$ .

In  $J_{TL}$  we assume that  $\phi$  is an average workfunction, averaged over the emitter surface. Similarly, for the Richardson constant  $A$ . The expression for  $J_{TL}$  is an average value  $\langle J_{TL} \rangle$  so that equation 7.1.4 becomes

$$\frac{1}{J} = \frac{1}{J_{SC}} + \frac{1}{\langle J_{TL} \rangle} \quad (7.1-4)$$

All real cathodes can be expected to have some patchiness in the workfunction. We will now show that it is reasonable to take

$$\langle J_{TL} \rangle = J_{TL} (\langle \phi \rangle) \quad (7.1-5)$$

where  $\langle \phi \rangle$  is the average of the workfunction over the surface of the cathode, i.e.,

$$\langle \phi \rangle = \iint \phi(x,y) \, dx dy / \iint dx dy \quad (7.1-6)$$

In order to show that equation 7.1.5 is reasonable, we must make some assumptions about the workfunction distribution over the surface. We will assume that we can write, once we know the distribution  $f(\phi)$ , that



$$\langle \phi \rangle = \int_0^{\infty} f(\phi) \phi d\phi \quad (7.1-7)$$

where

$$\int_0^{\infty} f(\phi) d\phi = 1 \quad (7.1-8)$$

As we discussed in section 6 we should expect a distribution function that is bounded from below. The gamma distribution we found best describes our experimental results, so we will use the same gamma distribution to demonstrate that equation 7.1.5 is reasonable.

With this assumption we can write the average temperature limit current density by

$$\langle J_{TL} \rangle = \int_0^{\infty} f(\phi) J_{TL}(\phi) d\phi \quad (7.1-9)$$

Where  $J_{TL}(\phi)$  is given by equation 7.1.3 and  $f(\phi)$  satisfies the integral in equation 7.1.8.

Now if we insert the generalized gamma distribution given in section 6, equation 6.1.1 into equation 7.1.9 we get

$$\langle J_{TL} \rangle = \frac{\lambda^\eta}{\Gamma(\eta)} \int_0^{\infty} (\phi - \phi_m)^{\eta-1} e^{-\lambda(\phi - \phi_m)} J_{TL}(\phi) d\phi \quad (7.1-10)$$

where  $\phi_m$  is the minimum workfunction for the particular cathode type. Substituting equation 7.1.3 we can easily show that

$$\langle J_{TL} \rangle = J_{TL}(\phi_m) \frac{\lambda^\eta}{\Gamma(\eta)} \int_0^\infty (\phi - \phi_m)^{\eta-1} e^{-\left(\lambda + \frac{11600}{T}\right)(\phi - \phi_m)} d\phi \quad (7.1-11)$$

If we now use the relationship (see equation 6.1.4),

$$\langle \phi \rangle = \phi_m + \eta/\lambda, \quad (7.1-12)$$

we can show that

$$\langle J_{TL} \rangle = J_{TL}(\langle \phi \rangle) \left(1 - \frac{11600}{\lambda' T}\right)^\eta e^{\left(\frac{11600}{T \lambda'}\right)^\eta} \quad (7.1-13)$$

where

$$\lambda' = \lambda + \frac{11600}{T} \quad (7.1-14)$$

If we take the effective Richardson constant to be

$$A^* = 120 e \frac{11600\eta}{\lambda' T} \left( 1 - \frac{11600}{\lambda' T} \right)^\eta \quad (7.1-15)$$

we arrive at our result

$$\langle J_{TL}(\phi) \rangle = J_{TL}(\langle \phi \rangle) . \quad (7.1-16)$$

Effectively the same result can be obtained with the Weibull or Guassian distributions. Any reasonably sharply peaked distribution will give the same result.

The purpose for going through this argument is to justify the use of  $\langle \phi \rangle$  instead of having to work with the spacial integral

$$\langle J_{TL} \rangle = \iint J_{TL}(x, y) \, dx dy / \iint dx dy . \quad (7.1-17)$$

In an aging model for dispenser cathodes that we developed in the past,<sup>1</sup> we used this argument implicitly by writing down the linearized workfunction with surface coverage

$$\phi(\theta) = \phi_w (1 - \theta) + \phi_{sys} \theta . \quad (7.1-18)$$

---

1 R. T. Longo, IEDM, Washington 1978, p. 152.

In the modeling developed here we will write down a more realistic function for  $\phi(\theta)$  which is really an average workfunction, averaged over the surface.

## 7.2 SURFACE COVERAGE WORKFUNCTION MODEL

In this model we will assume that the surface can be described by the average surface dipole  $P$  which is a function of  $\theta$ .

The coverage  $\theta$  is a statistical variable which can be defined most easily by use of a schematic picture, see Figure 7.2-1.

Figure 7.2-1(a) shows a perfectly clean surface in this case  $\theta = 0$ . The dipole responsible for the workfunction is just the uniform outer layer of the substitute material.

As the number of atoms or molecules on the surface increases, figure 7.2-1(b) shows a typical situation, the average dipole on the surface can be thought of as some combination of the base substrate dipole and the add-on atom or molecule dipole.

It is clear from this picture that the surface condition may be changed considerably from a microscopic viewpoint, without changing  $\theta$ .

This indicates the macroscopic, statistical nature of  $\theta$ . Another way of looking at  $\theta$  is that it is related to the ratio of the number of add-on atoms, to sites (i.e.,  $\theta \sim N_a/N_s$ ), but it does not depend upon which sites are occupied or unoccupied. Figure 7.2-1(c) shows the system when  $\theta = 1$ . The important concept here is that even though the macroscopic variable  $\theta$ , indicates one effective monolayer, patches of the base substrate are still exposed and still influence the average surface dipole. As  $\theta$  increases beyond 1, as seen in Figure 7.2-1(d), the patches of base substrate get smaller and smaller, but  $\theta$

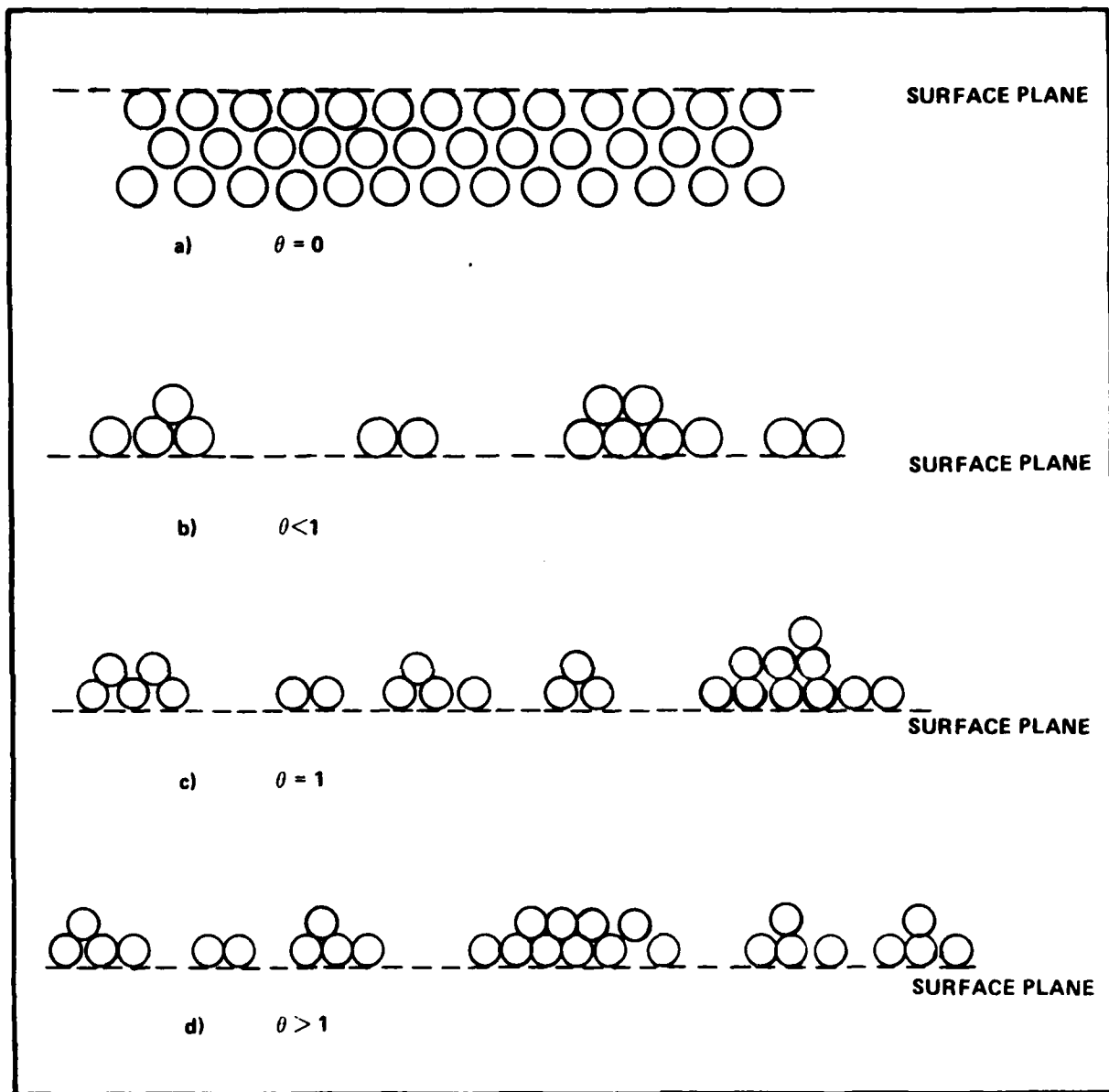


Figure 7.2-1 Schematic microscopic view of dipole coated surface for different value of the microscopic variable  $\theta$ .

must become fairly large before the substrate's influence becomes negligible. A final comment on the "picture" we have of  $\theta$ . Even though we sketched multiple layers of Ba in Figure 7.2-1, this is only to indicate the number of atoms we need to supply to the surface to produce a given  $\theta$ . In fact the multiple layers would evaporate so fast as to be nonexistent.

Now that we have defined our concept of  $\theta$ , let us now discuss the surface dipoles. With a bare surface (Figure 7.2-1a) the outer layer of atoms provide a dipole layer  $P_M$  (where M stands for metal). This is the sum of the diode at each site divided by the number of sites  $N_s$ , i.e.,

$$P_M = \frac{1}{N_s} \sum_i P_i . \quad (7.2-1)$$

Similarly we will argue that when  $\theta \rightarrow \infty$  all sites are covered, and from the outside world, the surface looks like pure Barium metal surface (in our case). The dipole of that surface is  $P_{Ba}$ .

Now our model for how the net dipole depends on  $\theta$  can be defined. This model envisions that each dipole component varies with respect to  $\theta$  by the simple rate equations

$$\frac{dP_M}{d\theta} = -\alpha P_M \quad (7.2-2)$$

$$\frac{dP_{Ba}}{d\theta} = -\beta (P_{Ba} - P_{Ba}(\infty)) \quad (7.2-3)$$

(i.e., the rate at which the change in the dipole takes place depends upon the value of the dipole, which in some sense is related to how many of a given dipole are present. The parameters  $\alpha$  and  $\beta$  are effectively the rates with respect to  $\theta$  .

The total average dipole is then

$$P(\theta) = P_M(\theta) + P_{Ba}(\theta) . \quad (7.2-4)$$

Finally we argue that the dipole surface layer, which is the value of  $P(\theta)$ , is the energy to move an electron across the surface dipole and therefore is the same as the workfunction, i.e.,

$$\phi(\theta) = \langle \phi_M(\theta) \rangle + \langle \phi_{Ba}(\theta) \rangle . \quad (7.2-5)$$

The solution of these two equations (equations 7.2-2 and 7.2-3) are simply

$$P_M(\theta) = P_M(0) e^{-\alpha\theta} \quad (7.2-6)$$

and

$$P_{Ba}(\theta) = P_{Ba}(\infty) (1 - e^{-\beta\theta}) . \quad (7.2-7)$$

Writing these in terms of workfunctions we get

$$\phi(\theta) = \phi_M e^{-\alpha\theta} + \phi_{Ba} (1 - e^{-\beta\theta}) . \quad (7.2-8)$$

Now, if we assume that at  $\theta = \theta_m$  (where  $\theta_m$  is the optimum coverage, not necessarily one monolayer), the net workfunction has a minimum, and we can place conditions on the rates  $\alpha$  and  $\beta$ .

Differentiating equation 7.2-8 and setting the result to zero, (i.e.  $\phi'(\theta_m) = 0$ ) we get

$$\left[ \Gamma \left( \frac{\phi_M}{\phi_{Ba}} \right) \right]^{\frac{1}{1-\Gamma}} = e^{-\beta\theta_m} , \quad (7.2-9)$$

where  $\Gamma = \alpha/\beta$ , the ratio of the relative covering rates.

We can then write an equation for the minimum workfunction  $\phi(\theta_m) = \phi_m$ ,

$$\phi_m = \phi_M \left( \Gamma \frac{\phi_M}{\phi_{Ba}} \right)^{\frac{\Gamma}{1-\Gamma}} + \phi_{Ba} \left( 1 - \left( \Gamma \frac{\phi_M}{\phi_{Ba}} \right)^{\frac{1}{1-\Gamma}} \right) . \quad (7.2-10)$$

The minimum workfunction is determined by one parameter,  $\Gamma$ , since  $\phi_M$  and  $\phi_{Ba}$  are known,



$$\phi_M = \phi_{\text{tungsten}} = 4.5 \text{ ev.}$$

$$\phi_{\text{Ba}} = 2.55 \text{ ev.}$$

If we know  $\phi_m$ , then we can determine  $\Gamma$ . Figure 7.2-2 is a plot of  $\phi_m$  vs  $\Gamma$ . If we take  $\phi_m = 1.98 \text{ ev}$ , we find that  $\Gamma = 2.50$  (for  $\phi_M = 4.5 \text{ ev}$  and  $\phi_{\text{Ba}} = 2.55 \text{ ev}$ ).

Once we know  $\Gamma$  we have completely determined  $\phi(\theta)$ . If we take  $\theta = \theta / \theta_m$  we can write

$$\phi(\theta) = \phi_M \left( \Gamma \frac{\phi_M}{\phi_{\text{Ba}}} \right)^{\frac{\Gamma\theta}{1-\Gamma}} + \phi_{\text{Ba}} \left( 1 - \left( \Gamma \frac{\phi_M}{\phi_{\text{Ba}}} \right)^{\frac{\theta}{1-\Gamma}} \right). \quad (7.2-11)$$

Figure 7.2-3 shows  $\phi(\theta)$  vs  $\theta$ , for the above condition.

In what follows, we shall use this to extract some further information from our work function data set. But before we can do that we must model the barium evaporation rate.

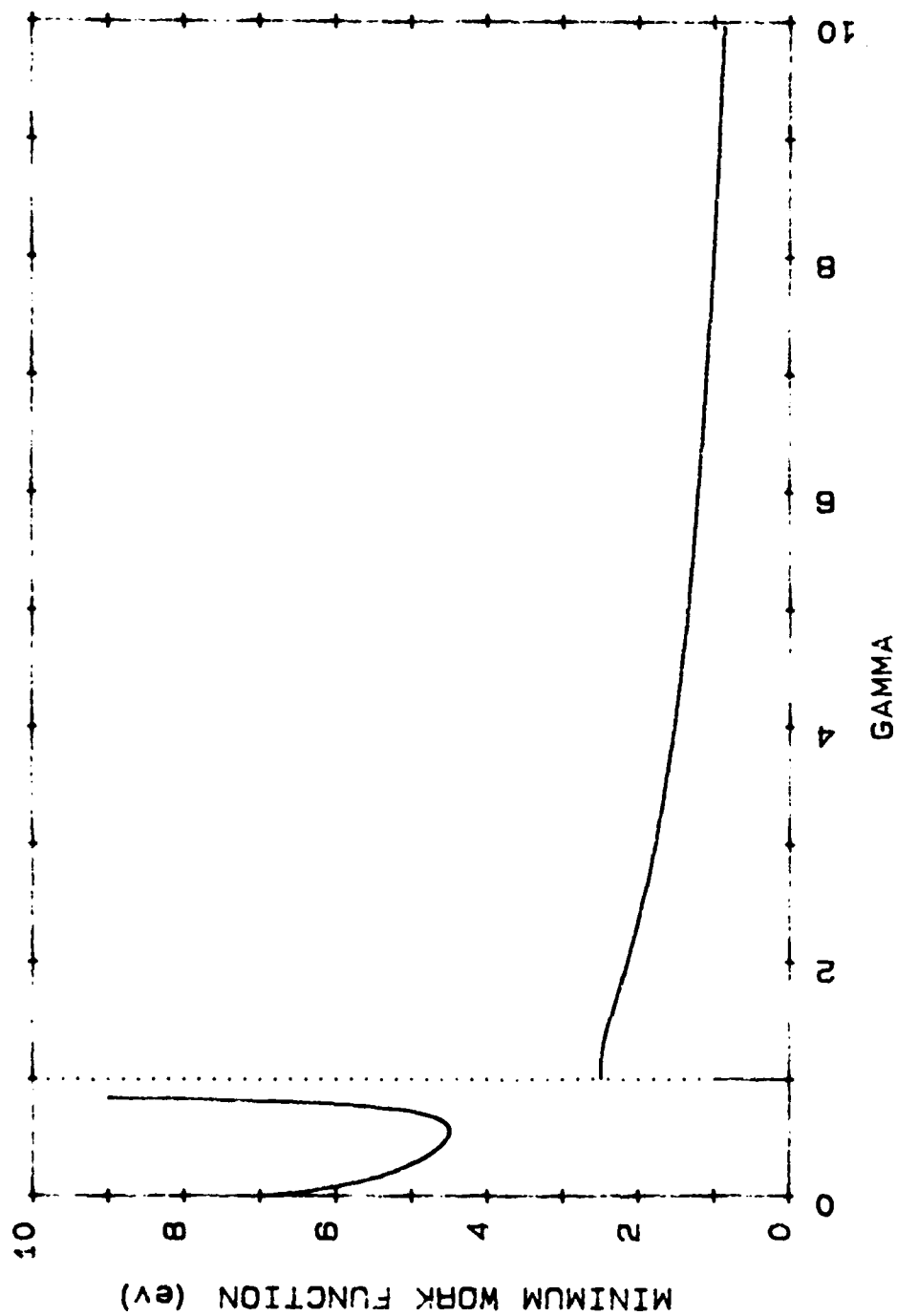


Figure 7.2-2 Minimum work function vs  $\Gamma$ .

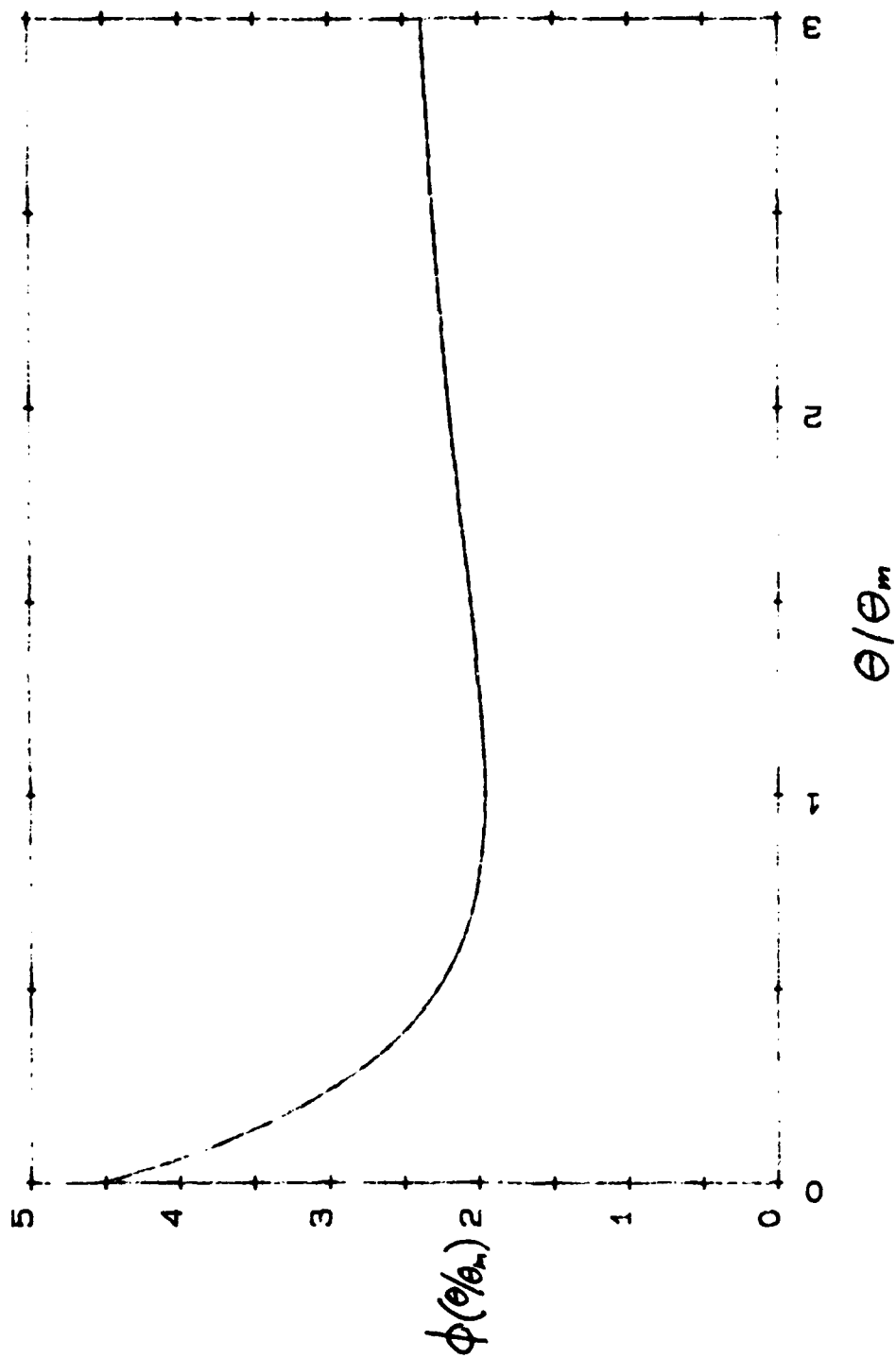


Figure 7.2-3 Average work function  $\phi(\theta/\theta_m)$  vs  $\theta/\theta_m$ .

### 7.3 BARIUM EVAPORATION RATE

The barium evaporation rate data was summarized in section 6.2, Table 6.2-1. It is dependent upon the billet powder size, the effects of coatings and the aluminate mix. Let us define several parameters:

1.  $r_g$  is the average tungsten particle grain radius (i.e.  $r_g = 5$  or 11 micron).
2. Let  $M = 0$  for a tungsten surface and  $M = 1$  for an OsRu coated surface.
3.  $F$  is the molar fraction of barium oxide in the aluminate  
 $F = .666$  for (4: 1: 1)  
 $F = 0.5$  for the (5: 3: 2)

(e.g., for the 4:1:1 we have  $4 + 1 + 1 = 6$ . Then the fraction of barium  $F = 4/6 = .666$ ).

With these variables we can summarize the parameters in Table 6.2-1 by the two mathematical equations,

$$\begin{aligned} \ln R_0 = & (49.2 - 2.2 r_g + 33.5 M - 0.6 r_g M) \\ & - (30.1 - 3.4 r_g + 54.8 M - 1.0 r_g M) F \end{aligned} \quad (7.3-1)$$

and

$$\begin{aligned} c = & 6.89 + 3.66 M - 0.26 r_g - 0.033 r_g M \\ & - (5.18 + 5.96 M - 0.37 r_g - 0.066 r_g M) F \end{aligned} \quad (7.3-2)$$

With these two equations we can now interpolate within the data set. The coefficient  $R_0$  must be multiplied by  $2.17 \times 10^{11}$  to obtain units of atoms/cm<sup>2</sup> sec.

#### 7.4 MODELING SURFACE COVERAGE WITH BARIUM EVAPORATION RATE

In section 6 we commented that the data suggested that the difference between the tungsten and the OsRu coated surfaces is due to the sticking time of the dipoles.

In the following we will attempt to extract a sticking time from the data. It turns out that we can determine the sticking time from the data by using the workfunction vs coverage model previously developed to determine  $\phi$  from the workfunction  $\phi$ . The surface coverage  $\theta$  is determined by two effects:

- 1) surface diffusion of dipoles out of the pores and along the surface and
- 2) backscattering of barium from the closely spaced anode. We can write

$$\theta = \theta_0 + \tau_A R G(d) \quad , \quad (7.4-1)$$

where  $R$  is the barium evaporation rate from the cathode and  $\tau_A$  is the average monolayer sticking time of barium on the anode (this is not the sticking time we are interested in).

$G(d)$  is a geometric factor which is a function of the cathode to anode distance  $d$ . We shall develop  $G(d)$  below.

The intercept  $\theta_0$  is the value of the coverage we wish to determine. It is due to surface diffusion and is primarily related to the average monolayer sticking time of barium dipoles on the surface (i.e., with the anode at infinity).

Since all the workfunction measurements were made at different cathode to anode spacings,  $d$ , we will attempt to determine  $\theta_0$  from a plot vs.  $G(d)$ . First we must develop  $G(d)$ .

### 7.4.1 Geometric Factor

The flux of barium back to the cathode can be calculated from first principles. The results are very complicated, however. We shall use a much simpler argument to determine a relationship for  $G(d)$ . Figure 7.4-1 shows the geometry. In this very simplified argument we will assume that an atom that strikes  $S_r$  is reflected back to the cathode. An atom that passes through the imaginary surface of area  $S_e$  escapes and does not reflect back to the cathode. With this idea in mind, we can say that the probability of an atom leaving the cathode and striking  $S_r$ , then leaving  $S_r$ , and returning to the cathode of area  $A_c$  is given by

$$P = \left( \frac{S_r}{S} \right) \left( \frac{A_c}{S} \right) \quad (7.4-2)$$

where  $S = S_r + S_e$ , the total surface area that an atom can impinge on once leaving the cathode. The probability that a particular atom undergoes  $n$  reflections before passing through  $S_e$  and is lost is just  $n$  products

$$P_n = \left[ \left( \frac{S_r}{S} \right) \left( \frac{A_c}{S} \right) \right]^n \quad (7.4-3a)$$

The total flux of atoms we take as the sum of the contributions from all orders of reflections is

$$F = R \sum_{n=1}^{\infty} \left( \frac{S_r A_c}{S^2} \right)^n \quad (7.4-3b)$$

which sums to

$$F = \frac{R S_r A_c}{S^2 - S_r A_c} \quad (7.4-4)$$

G12347

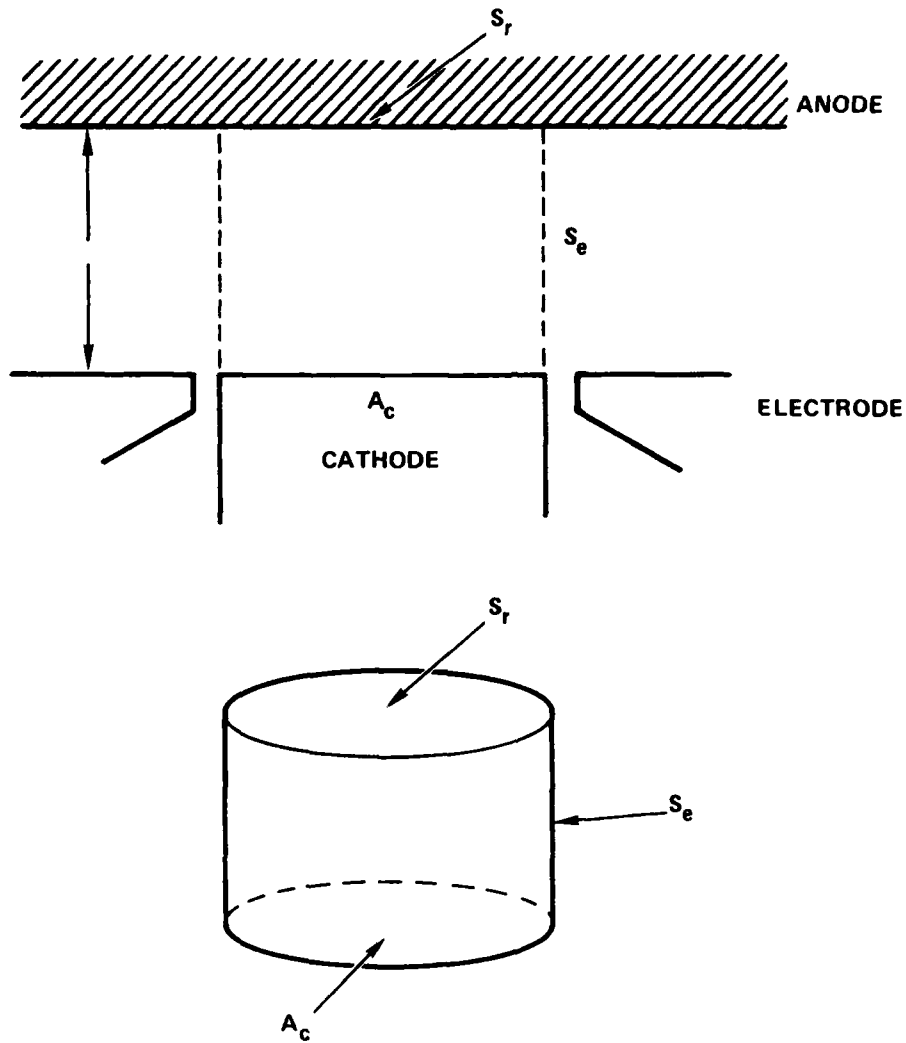


Figure 7.4-1 Geometry used to calculate the geometric factor.  $S_r$  is the reflection area.  $S_e$  is the escape area and  $A_c$  is the cathode area.

The geometric factor is therefore

$$G(d) = \frac{S_r A_c}{S^2 - S_r A_c} \quad (7.4-5)$$

The various areas can now easily be determined from the simple geometry given in figure 7.4-1. The result is

$$G(d) = \frac{A_c^2}{2d \left[ \sqrt{4\pi A_c} + 2\pi d \right]}, \quad (7.4-6)$$

where we have taken  $A_c = S_r$ .

#### 7.4.2 Analysis of data with surface coverage model

The next step is to use the surface coverage model to invert  $\phi(\theta)$  to obtain  $\theta$ . This can be done in two ways: 1) for  $\theta < 1$  and 2) for  $\theta > 1$ .

It turns out that all of our data is consistent with  $\theta < 1$ . When we try to use  $\theta > 1$  we obtain a negative  $\tau_A$  i.e., the slope of the spacing dependence is negative which is not physical. The analysis that follows then is for  $\theta < 1$  in all cases. This is done for each work function and a corresponding  $\theta$  is obtained.

We now separate the total data set into two subsets: 1) all tungsten surface cathodes and 2) all OsRu coated cathodes.

We then divide the temperature interval of our experiment (which ranges from 1200 K to 1400 K) into  $20^\circ$  K intervals.

With the computer we sort all data of each subset (W and Os:Ru) into the  $20^\circ$  K intervals. The values of  $\theta$  are then plotted versus the geometric factor times the evaporation rate,  $RG(d)$ , for each temperature interval. The slope of the curves gives  $\tau_A$  (one for each temperature interval of  $20^\circ$  K). The slopes result in positive values for the average monolayer sticking time on the anode and are the same for both the tungsten and Osmium:Ruthenium cathodes. As expected, they are:



$$(\tau_A)_W = 0.51 \pm 0.45 \text{ sec/monolayer}$$

and

$$(\tau_A)_{OsRu} = 0.51 \pm 0.73 \text{ sec/monolayer.}$$

(7.4-7)

The fact that we get the same result for both subsets is exactly what we expect because the slope is a property of the Molybdenum anode and not a property of the cathode.

The intercept  $\Theta_0$  on the other hand is dependent on the cathode surface. The average values for all temperatures are

$$(\Theta_0)_W = 0.58 \pm 0.03$$

and

$$(\Theta_0)_{OsRu} = 0.68 \pm 0.03 .$$

(7.4-8)

These values also show a temperature dependence which can be seen in figure 7.4-2.

Here we plotted the natural log of  $\Theta_0$  versus  $1/T$  which is the usual way to plot a temperature dependent effect. The data are reasonable straight lines:

$$(\ln \Theta_0)_W = \frac{1120}{T} - 1.42$$

(7.4-9)

$$(\ln \Theta_0)_{OsRu} = \frac{1010}{T} - 1.17 .$$

Both the tungsten surface and the Osmium:Ruthenium surface have approximately the same slope, but are offset from each other.

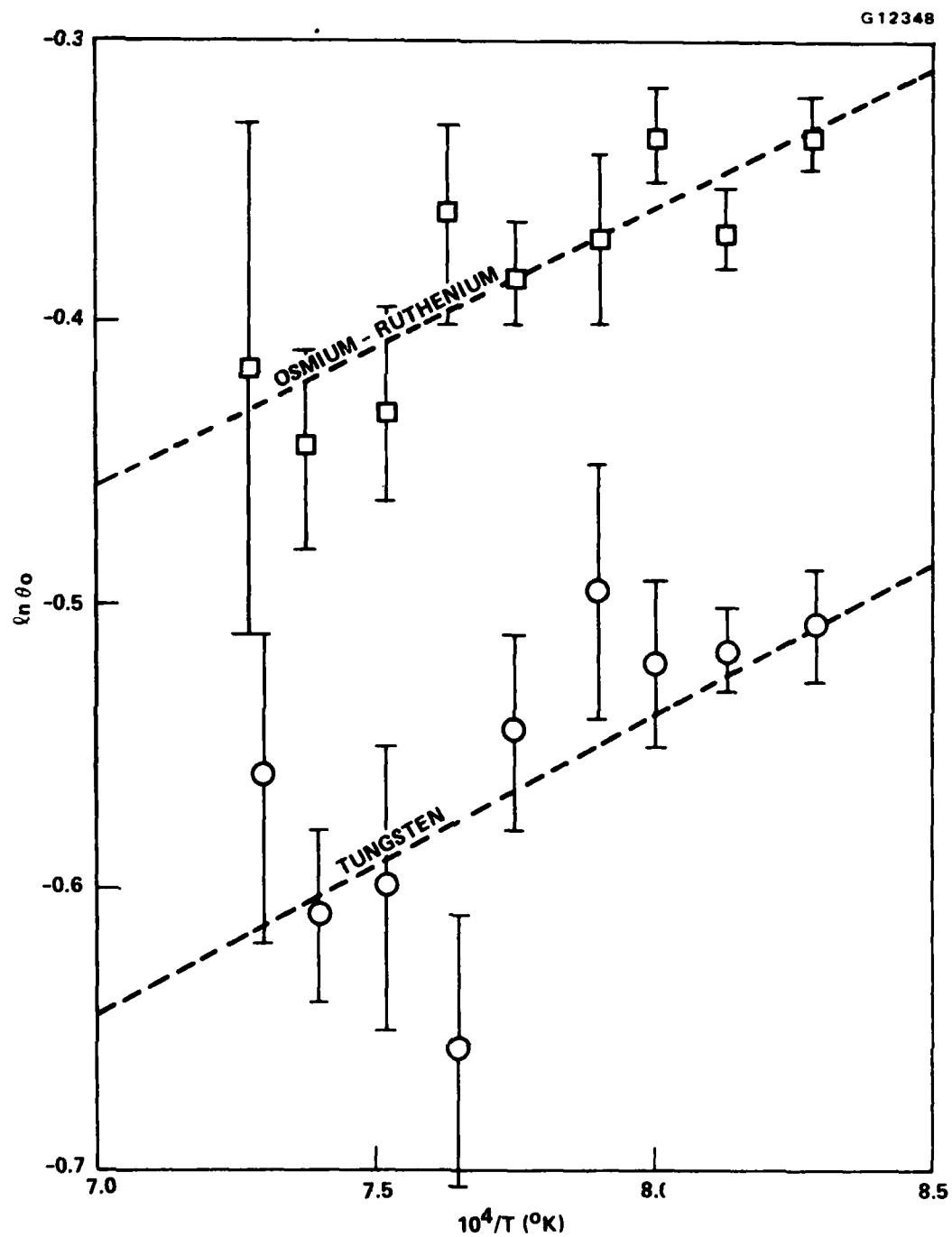


Figure 7.4-2 Temperature dependence of diffusional surface coverage.

The surface coverage due to diffusion,  $\theta_0$ , is related to the evaporation rate  $R$  and the average monolayer sticking time  $\tau$  by

$$\theta_0 = \tau R \quad (7.4-10)$$

We will write this as

$$\theta_0 = \tau_0 R_0 e^{+11600(\epsilon_\tau - \epsilon_R)/T} \quad (7.4-11)$$

Table 7.4-1 summarizes the parameters. It must be noted that the accuracy with which we can determine these parameters is poor. However, it must be noted that  $\epsilon_R < \epsilon_\tau$  is consistent with life test data. This data analysis yields an average monolayer sticking time for barium of about a factor of 2 longer for the Osmium:Ruthenium surface than for a tungsten surface. Table 7.4-2 gives the average monolayer sticking times for different temperatures.

#### 7.5 SUMMARIZING THE MODEL

In this model the objective is to determine the average cathode workfunction from more primitive quantities. We can write the average workfunction in summary as

$$\phi = \phi(\tau(M,T), R(r_g, M, F, T)) \quad (7.5-1)$$

The coverage factor

$$\theta = \theta(\tau, R) \quad (7.5-2)$$

is a function of the average monolayer sticking time of the dipoles on the surface and the evaporation rate of barium from the porous matrix. In turn, the average monolayer sticking time is a function of temperature  $T(^{\circ}\text{K})$  and the kind of substrate surface (tungsten or Osmium:Ruthenium).

TABLE 7.4-1

## SUMMARY OF SURFACE COVERAGE PARAMETERS

	$\epsilon_R$ (ev)	$\epsilon_T$ (ev)	$R_0 \left( \frac{\text{monolayer}}{\text{cm}^2 \text{ sec}} \right)$	$\tau_0 \left( \frac{\text{sec}}{\text{monolayer}} \right)$
Tungsten	3.6	3.7	$4.9 \times 10^8$	$9.6 \times 10^{-9}$
Osmium: Ruthenium	3.8	3.9	$2.0 \times 10^9$	$3.1 \times 10^{-9}$

TABLE 7.4-2

## AVERAGE MONOLAYER STICKING TIMES

$T^\circ\text{K}$	Tungsten $\tau$ (sec)	Osmium:Ruthenium $\tau$ (sec)
1200	$3.3 \times 10^7$	$7.5 \times 10^7$
1300	$2.2 \times 10^6$	$4.1 \times 10^6$
1400	$2.0 \times 10^5$	$3.3 \times 10^5$

The evaporation rate we determined to be a function of the partial grain size,  $r_g$ , in microns and the type of surface ( $M = 1$  for Osmium:Ruthenium and  $M = 0$  for tungsten), the relative fraction of barium in the aluminate,  $F$ , and the temperature. Once the workfunction is determined from the properties at the surface, porous matrix and aluminate, it can be folded into the emission current density given by

$$\frac{1}{J} = \frac{1}{J_{SC}} + \frac{1}{J_{TL}} \quad , \quad (7.5-3)$$

to determine the magnitude of current emission in a particular device.

#### 7.6 FINAL REMARKS

The modeling we have developed here is highly empirical and leaves a great deal to be desired from the purist. We make no claims about the physical reality of the model. It has been developed primarily to aid the experimentalist evaluate data, a "straw man" in effect to poke holes at with the hope that a more realistic and fundamental model will evolve.

## 8.0 CONCLUDING REMARKS

We can conclude from this study that, given the condition and level of impurities in the cathodes, the variations in the manufacturing process parameters reveal that:

1. The coating has the largest effect on the reduction of the cathode work function and little effect on the evaporation rate of barium from the cathode. This is not a surprising result and is in keeping with practical observations of TWT manufacturers.
2. The aluminate type (i.e. the amount of barium in the aluminate) has a substantial effect on both the work function and evaporation rate. Again, this is not an unexpected result from practical observations of TWT manufacturing. The S-type or (4:1:1) has always been easier to work with in early life, but can present problems with excess Ba evaporation contaminating the insulators.
3. The porosity of the billet appears to have very little effect on the work function or the evaporation rate of barium from the cathode. There has not been much emphasis among the manufacturers of dispenser cathode to hold a tight tolerance on the porosity of the billet so there has not been much practical experience with this parameter.

In general the more barium that arrives at the emitter surface per unit time the more active the cathode, (i.e. the lower the work function). The data from this program suggests the somewhat surprising results that if the evaporation rate is high enough the uncoated tungsten cathode approaches that of the coated Osmium:Ruthenium coated cathode.

We must remember that all of these measurements are on very young cathodes. The maximum age of any cathode studied was not more than 200 hrs, (and careful aging records on the cathodes were not kept). In effect we have only defined the initial conditions for the dispenser cathode based on the various process parameters.

The attempt to keep the material as pure as possible appears not to have been as successful as hoped. The higher than expected sulfur content of these cathodes, first noticed by B. Lamertine, undoubtedly had some effect on the values obtained for the workfunction as we discussed in Section 6.4. We believe, however, that the impurity levels represent a relatively constant background with little variation from cathode to cathode and therefore do not alter the basic conclusions drawn about the effects of the manufacturing process and material parameters. (Furthermore, our measurements indicate that the level of the main impurity sulfur is slightly lower than what is normally found in production dispenser cathodes throughout the industry.)

Modeling the dispenser cathode is a much more difficult task. To arrive at a true physical model we have to await the results of the surface study work being carried out at Wright-Patterson and elsewhere. We included some semi-empirical model suggestions in Section 7. The modeling will have to remain empirical until a more detailed atomic picture of the surface emerges.

#### 8.1 FURTHER WORK

At this time funding has been exhausted. The results of this program suggest that the coatings and the aluminates should be further investigated. Alloy coatings should be investigated to find those that maximize the barium sticking time. The generation rate of barium from the aluminates should also be studied.

#### 8.2 ACKNOWLEDGEMENT

The authors would like to thank Mr. C.R. Harrison for his technical support. Thanks also to Mr. G. Allaria, Mr. M. Barillas and Mr. D. Block for their efforts in the material and sample preparation. We extend thanks also to Mr. L. Dawson, a summer student, for taking a considerable amount of P.E.T. data.

## APPENDIX A

Any experimental study of thermionic emitters relies on some way to extract the cathode's work function from the measured cathode current. This is not trivial. The simplest way to obtain the work function is to lower the temperature of the emitter or to increase the field between the cathode and anode until the cathode is so temperature limited that the simple Schottky technique can be used.

There are several major objections with this approach:

1. Temperatures at which the Schottky technique becomes useable are considerably below the temperature range of application. The result therefore has to be extrapolated into the region of practical application. This introduces considerable uncertainty.
2. At normal operating temperatures the emission current is so large that realistic fields strengths will not be able to sweep out all of the space charge. Furthermore, extraneous heating of the entire system affects outgassing and disrupts the cathode work function.

These are serious objections and must be carefully considered. The question we must ask ourselves is how do we obtain a reasonably accurate measure of the cathode's work function under normal (or practical) operating conditions. The answer to this question may be different for each worker depending upon the equipment available.

The ability to effectively remove the influence of space charge from the J-V-T measurements is very important if reliable repeatable results are to be obtained. If the space charge is not correctly accounted for, the resulting workfunction will have an anomalously large geometry dependence (i.e., cathode to anode spacing dependence). This will be clearly shown below.



At the present time there does not exist an answer that can be developed from basic physical principles. In this effort we rely upon an empirical relationship which we have found to be a reasonably good representation of the observed current at any voltage or temperature. The empirical relationship is

$$\frac{1}{J} = \frac{1}{J_{SC}} + \frac{1}{J_{TL}} \quad (A-1)$$

$$J_{SC} = \frac{2.33 \times 10^{-6}}{d^2} V^{3/2} \quad (A-2)$$

$$J_{TL} = AT^2 e^{-11600\phi/T} e^{4.4\sqrt{V}/d/T} \quad (A-3)$$

This model was obtained by a principle we call asymptotic modeling. This principle suggests that we determine from basic physical principles the behavior of a system in asymptotic limits. In this case  $J_{SC}$  and  $J_{TL}$  are well known expressions and we view them as asymptotes. We then look for a simple analytical expression that approaches the appropriate asymptotes. The result is equation A-1.

The results that are obtained from this expression have some nice properties:

1. The resulting work function has less spacing dependence than it does when obtained by the Schottky technique. This can be easily seen by comparing the zero voltage intercept in figures A-1 through A-6. Figure A-1, A-2 and A-3 use the empirical equation, equation A1, to obtain  $J_{TL}$ . In Figures A-4, A-5 and A-6 the standard Schottky technique is used to obtain  $J_{TL}$ .

SAMPLE ID. B5M

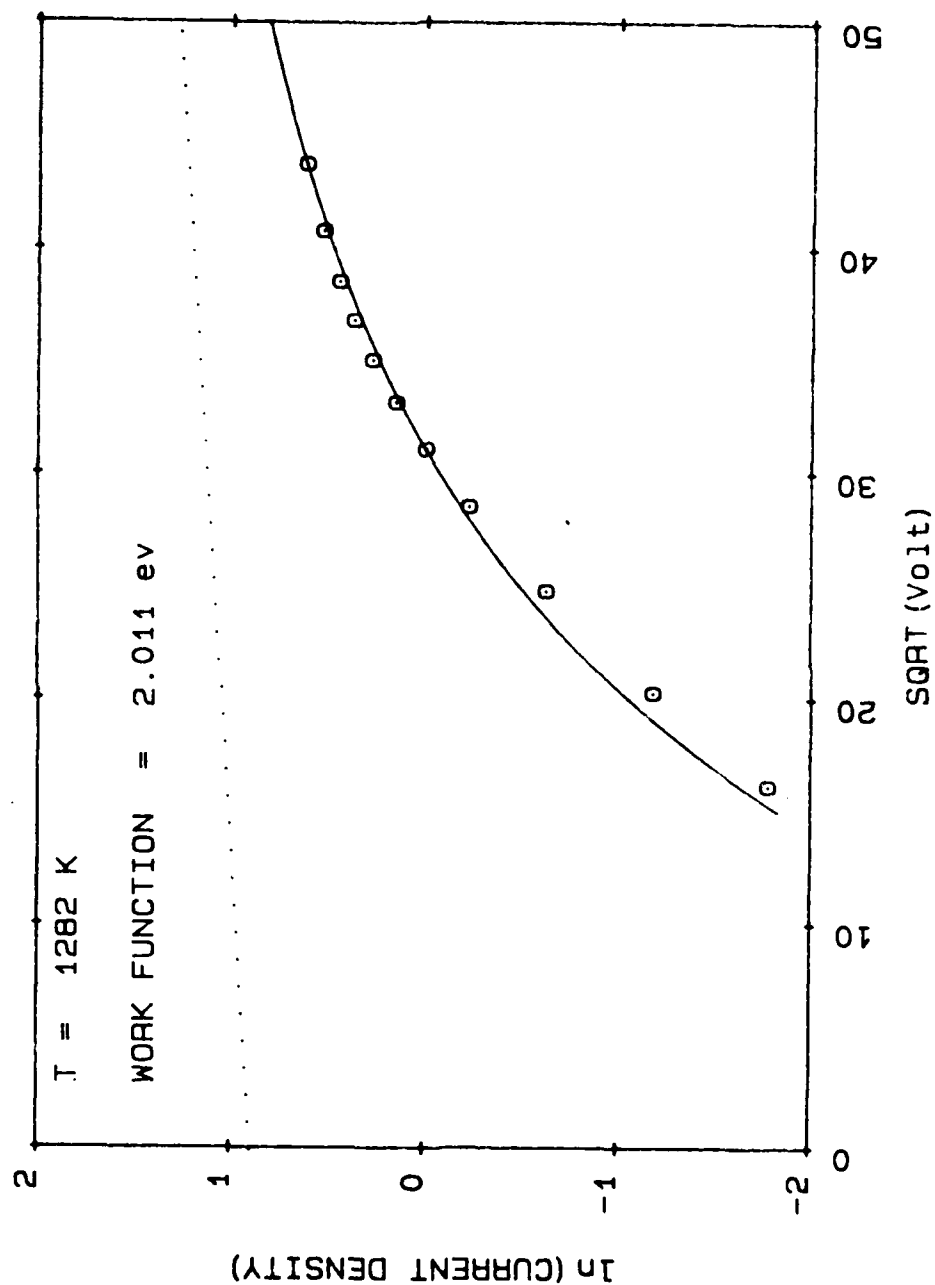


Figure A-1 Solid line is the reciprocal formula, dotted line is  $J_{TL}$ , the spacing is .22 cm.

SAMPLE ID. B5M

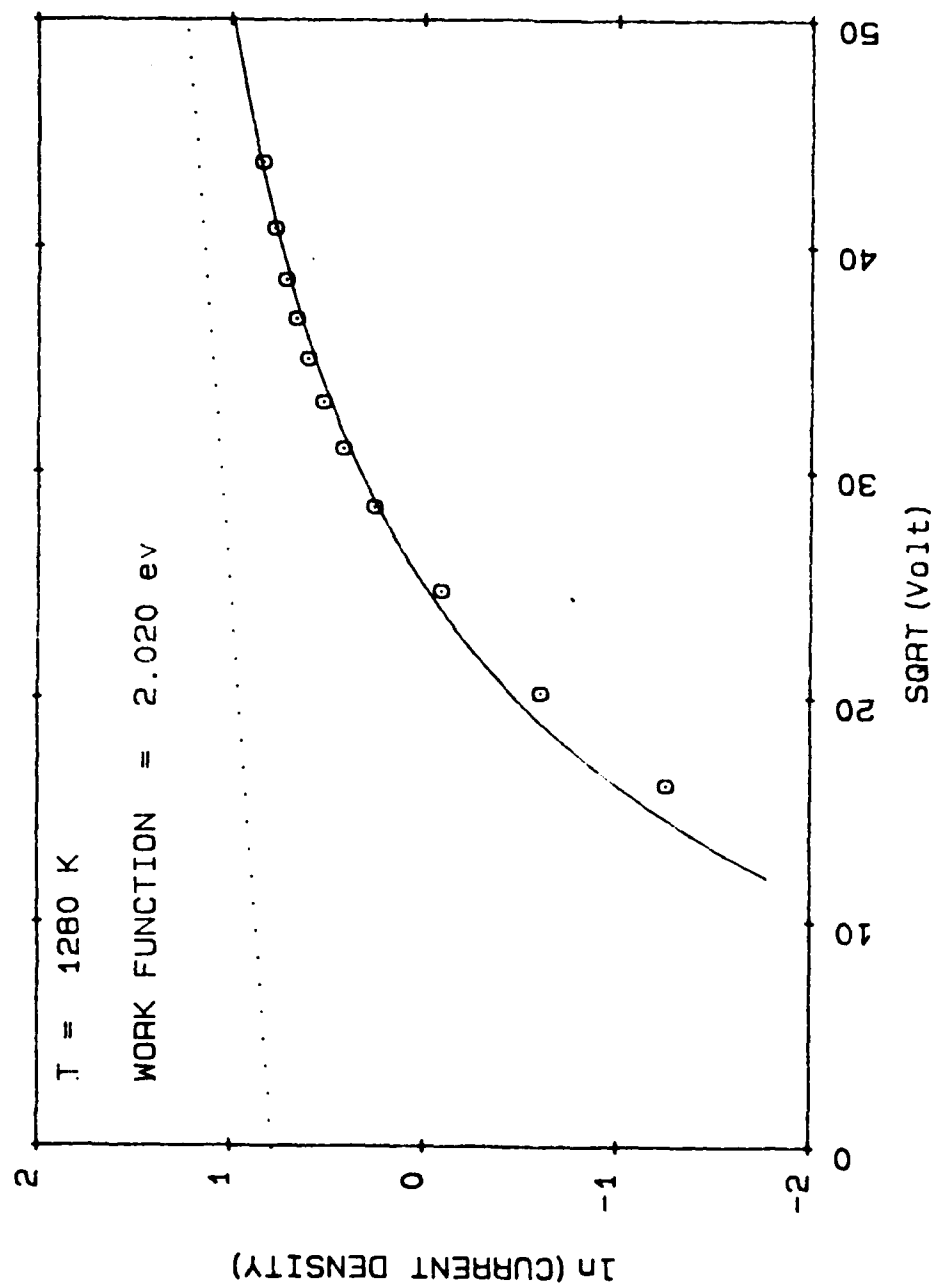


Figure A-2 Solid line is the receiptrocal formula, the dotted line is  $J_{TL}$ , spacing is .15 cm.

SAMPLE ID. B5M

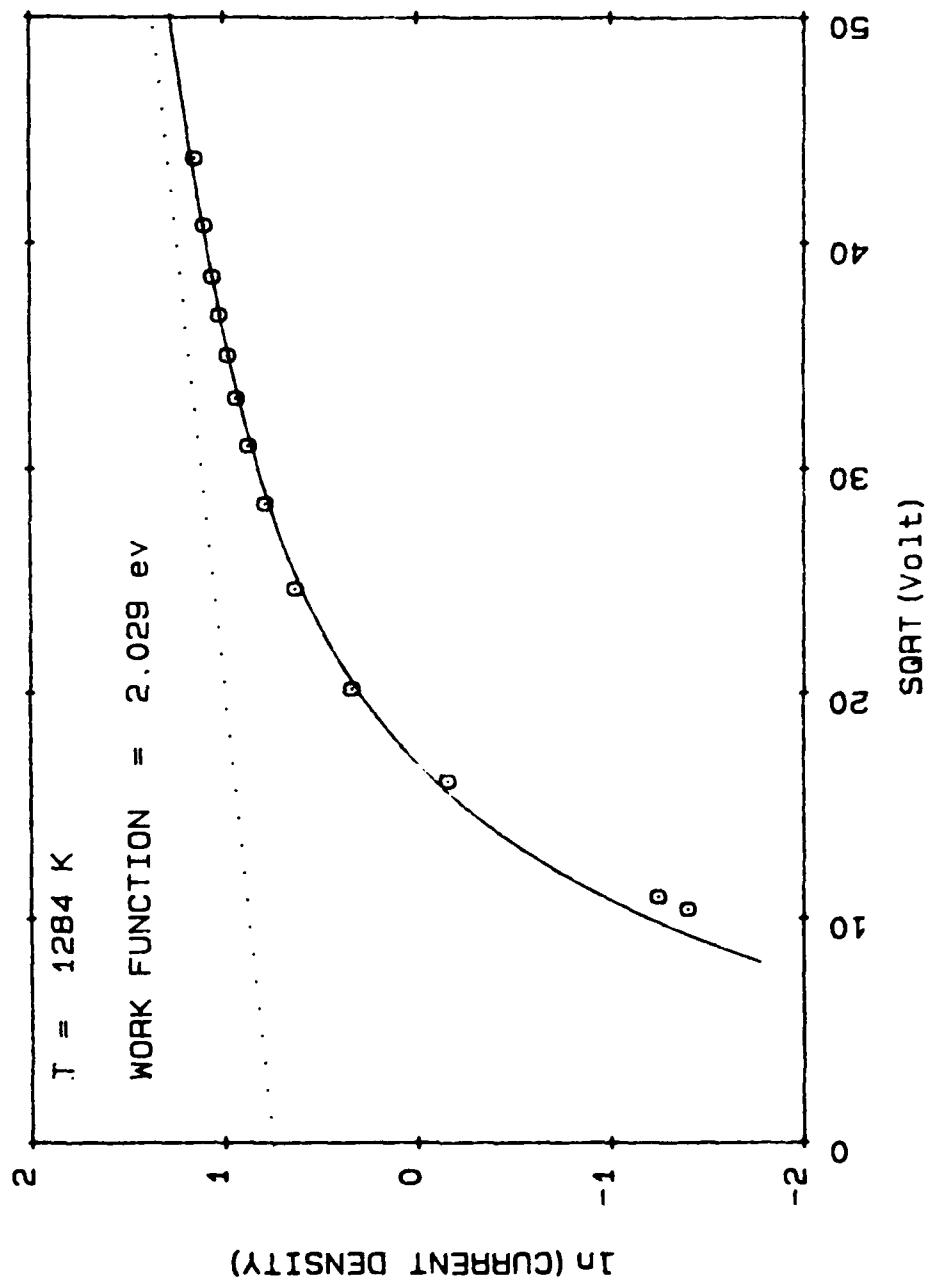


Figure A-3 Solid line is the reciprocal formula, the dotted line is  $J_{TL}$ , the spacing is .08 cm.

SAMPLE ID. B5M

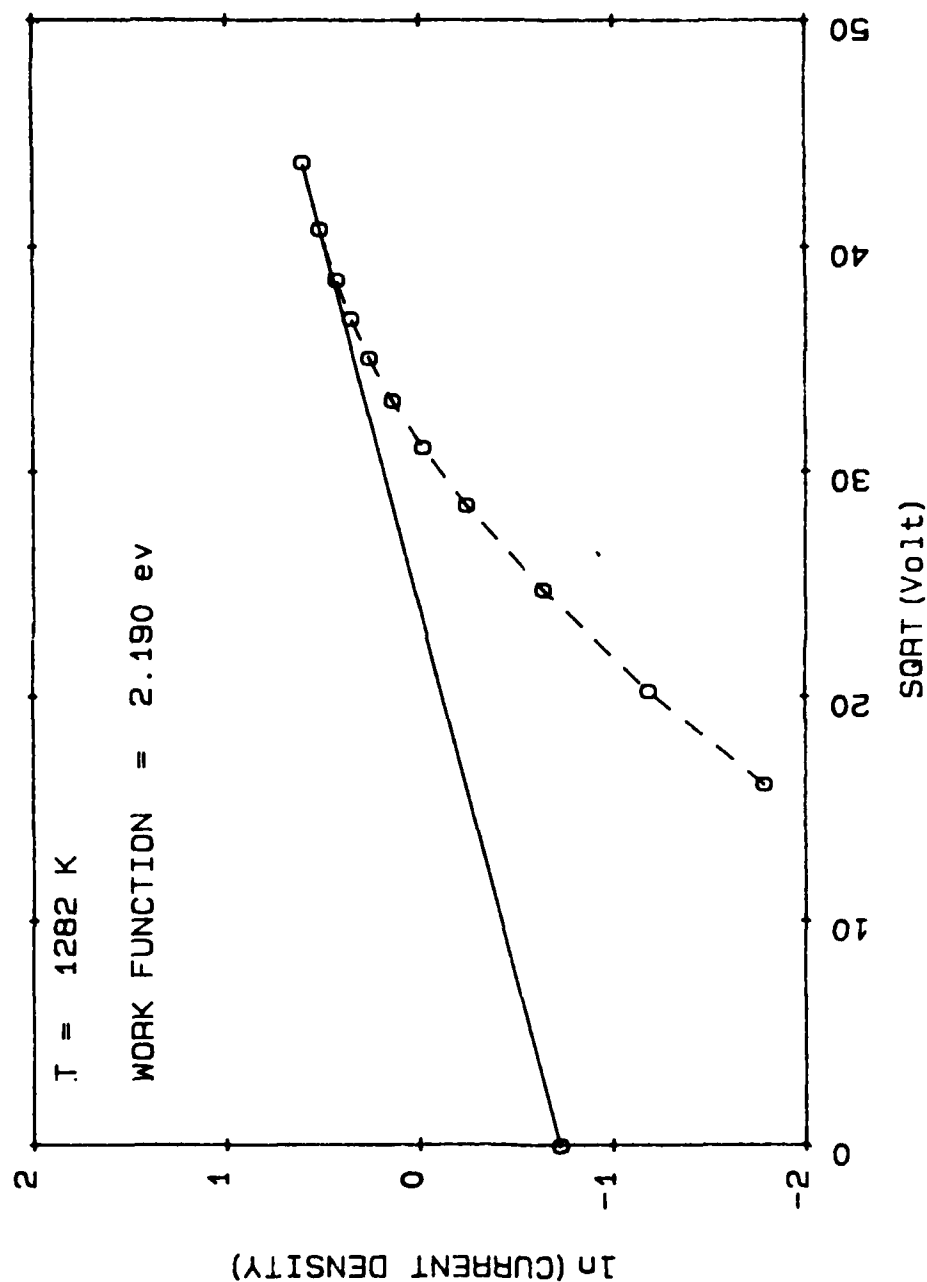


Figure A-4 Schottky analysis solid line is  $J_{TL}$ , spacing .22 cm.

SAMPLE ID. B5M

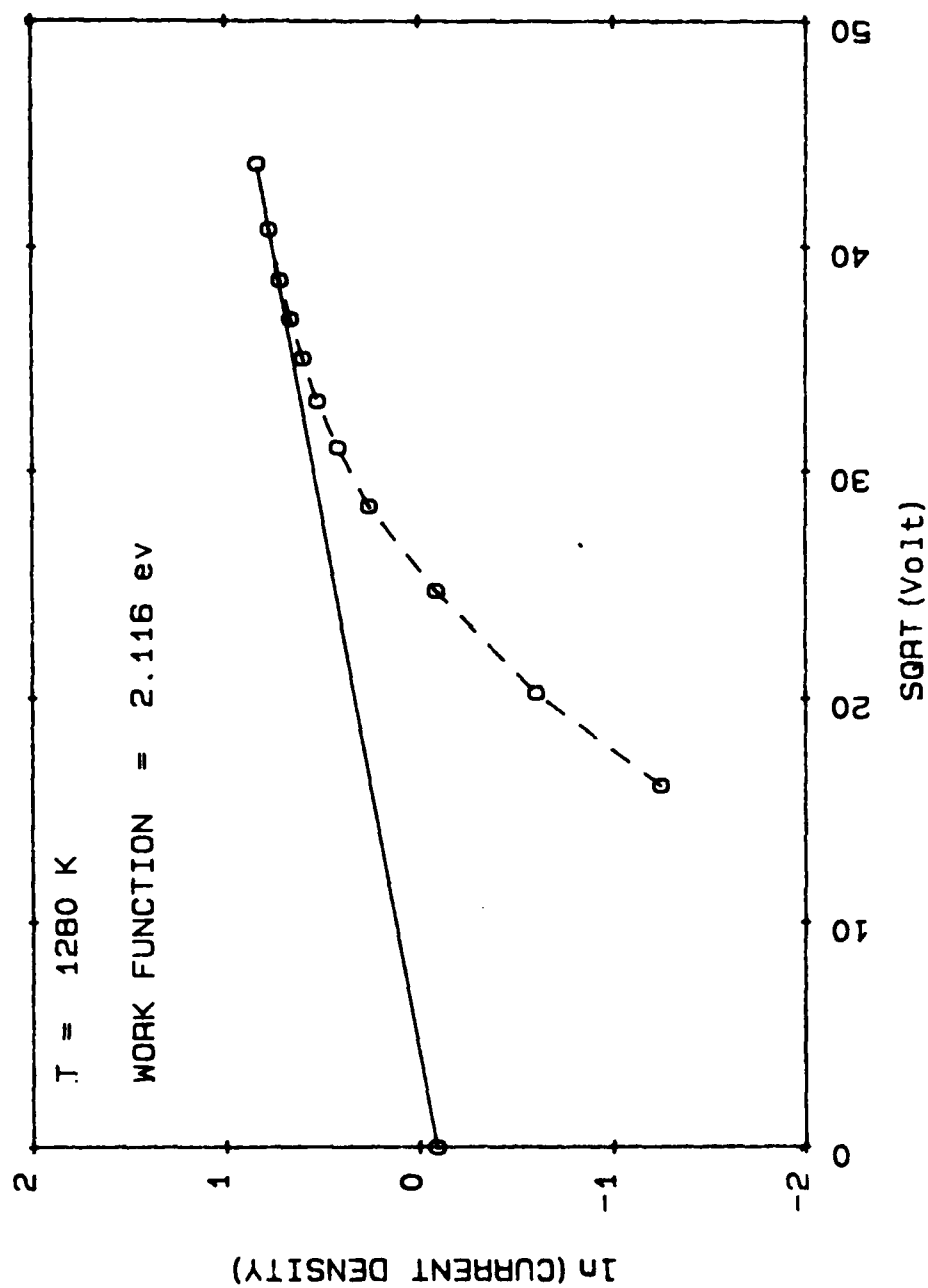


Figure A-5 Schottky analysis, solid line is  $J_{TL}$ , spacing is .15 cm.

SAMPLE ID. B5M

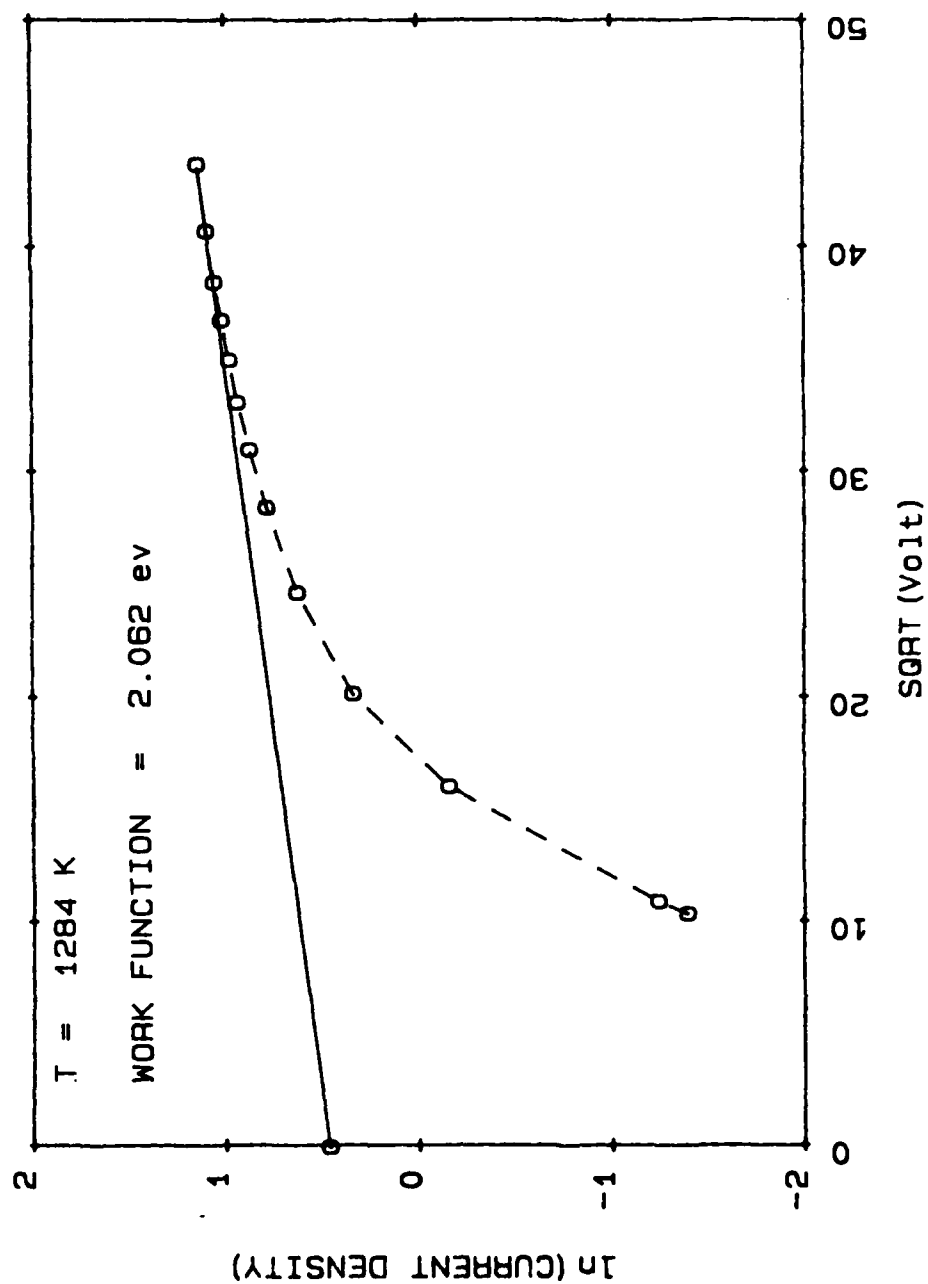


Figure A-6 Schottky analysis solid line is  $J_{TL}$ , spacing is .08 cm.

It is clear from these figures that as the spacing increases the space charge effects become more predominant at higher voltages. The empirical expression, equation A-1 compensates well for the space charge. Figures A-1 to A-3 show the saturated current density, which is the zero voltage intercept (the dotted line), does not vary much as the spacing is changed.

On the other hand, when analyzing the data with the so called standard Schottky technique of drawing a tangent to the highest available voltage points, the zero voltage intercept obtained is very spacing dependent, see Figures A-4 to A-6. The effects of spacing must be carefully evaluated by each worker and is dependent upon the equipment available for the measurements. Clearly, if one could take the applied voltage higher, the correct asymptote is approached. Furthermore, as the spacings get smaller the results obtained by both techniques merge.

2. The data fits a universal curve generated from equation A1 but does not fit the equivalent Child-Schottky universal curve. This can be seen from figure A7. The solid line is the universal curve obtained from equation A1, the dotted line (with slope 1) is the Child-Schottky universal curve. It is obvious from figure A7 that the data is described by the empirical express and is not described by the Child-Schottky universal curve. The universal curves are simply obtained as follows:

1. Child-Schottky case:

$$J = \begin{cases} J_{SC} & \text{for } J_{SC} < J_{TL} \\ J_{TL} & \text{for } J_{SC} > J_{TL} \end{cases} \quad (A-4)$$



The universal curve is obtained by plotting  $J/J_{TL}$  versus  $J_{SC}/J_{TL}$ . It is a line of slope = 1 until saturation; then it is a constant = 1 thereafter.

2. The empirical universal curve case: equation A-1 yields

$$J/J_{TL} = \frac{(J_{SC}/J_{TL})}{1 + (J_{SC}/J_{TL})}, \quad (A-5)$$

and is obtained by plotting

$$J/J_{TL} \text{ versus } J_{SC}/J_{TL}.$$

As a result, the workfunctions presented in this work are obtained by extracting  $J_{TL}$  from the empirical equation, equation A-1.

It is clear from figure A-7 that equation A-5 is a better representation of the data.

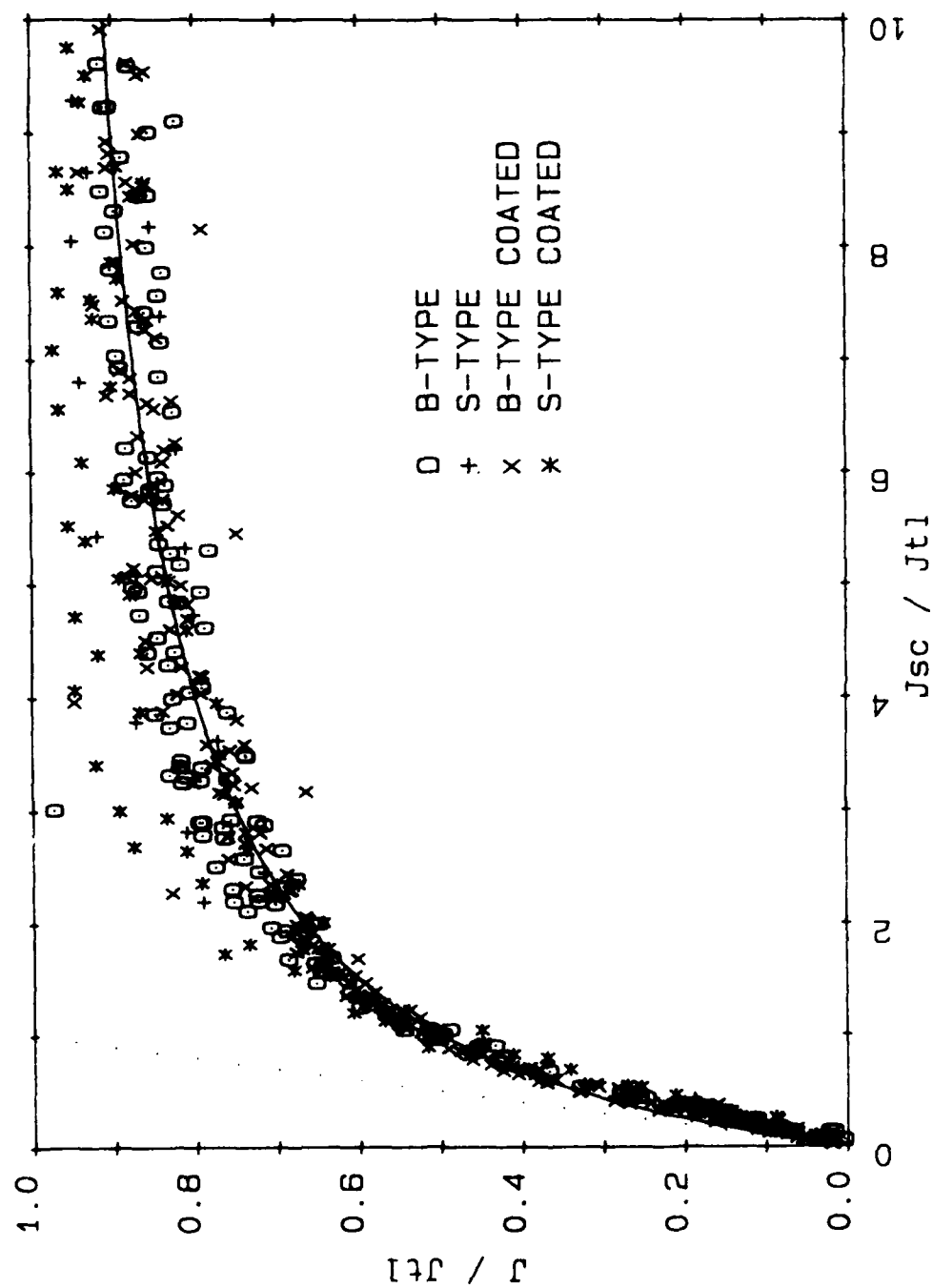


Figure A-7 Universal thermionic emission curve. The solid line is the reciprocal formula, the dotted line is the Child-Schottky curve.

APPENDIX B  
BARIUM EVAPORATION DATA

Barium Evaporation Data Figures B-1 to B-8 give the natural log of the times to peak in hours versus the reciprocal temperature in  $^{\circ}\text{K}$ .

The units of  $\text{ugm}/\text{cm}^2/\text{hr}$  are obtained by multiplying  $1/\tau$  by 0.18.

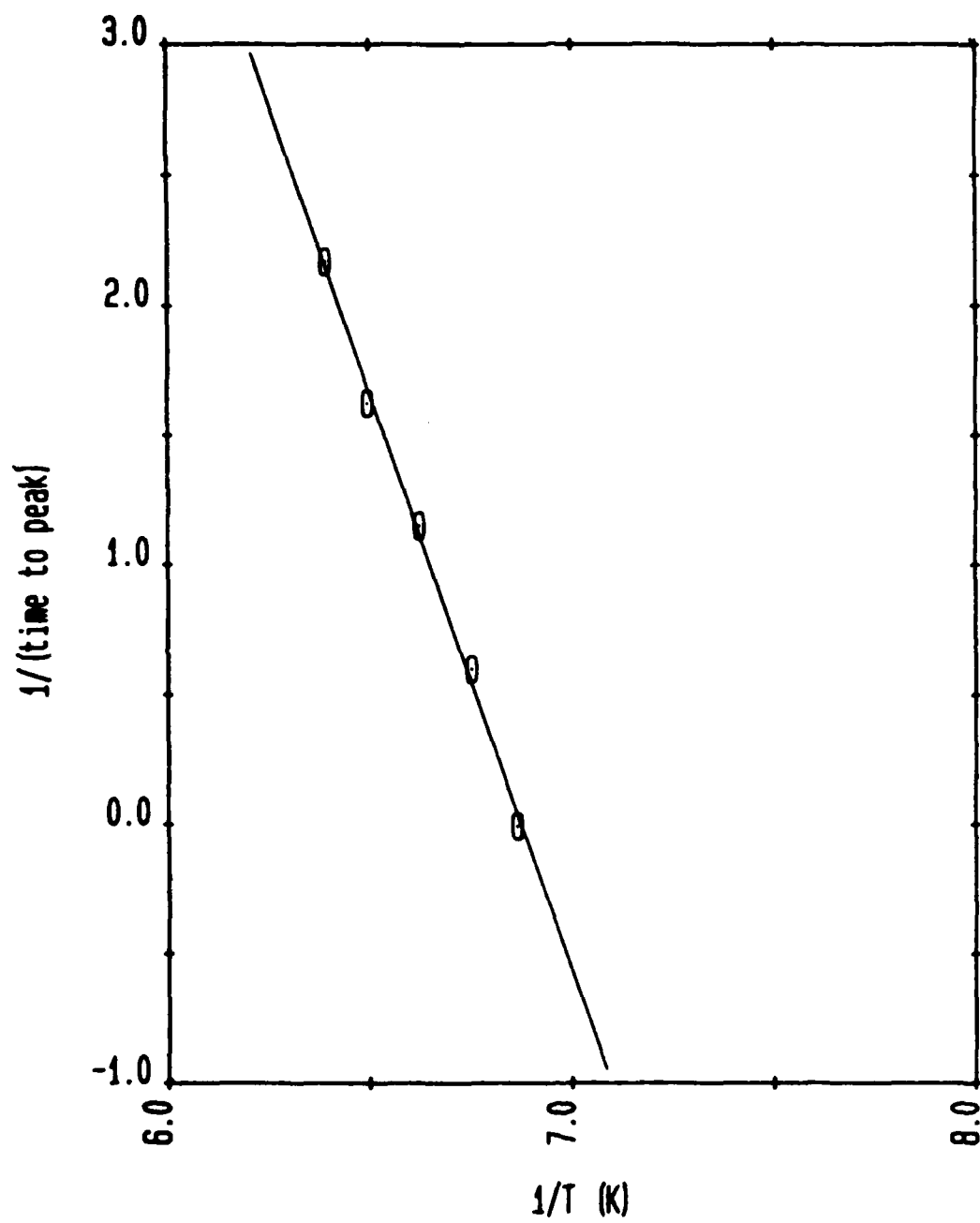


Figure B-1 B-type 5 micron tungsten.

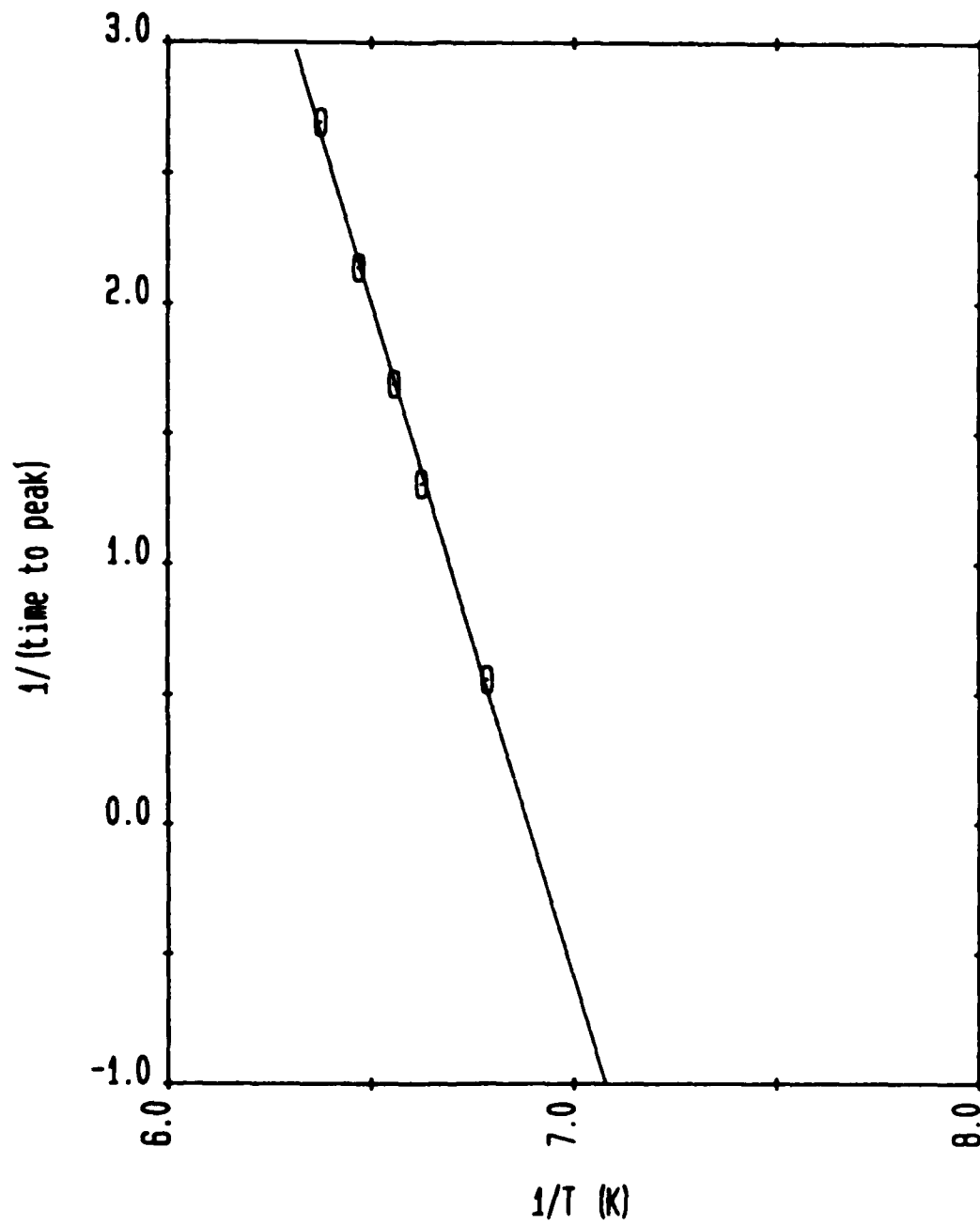


Figure B-2 B-type 5 micron OsRu coated.

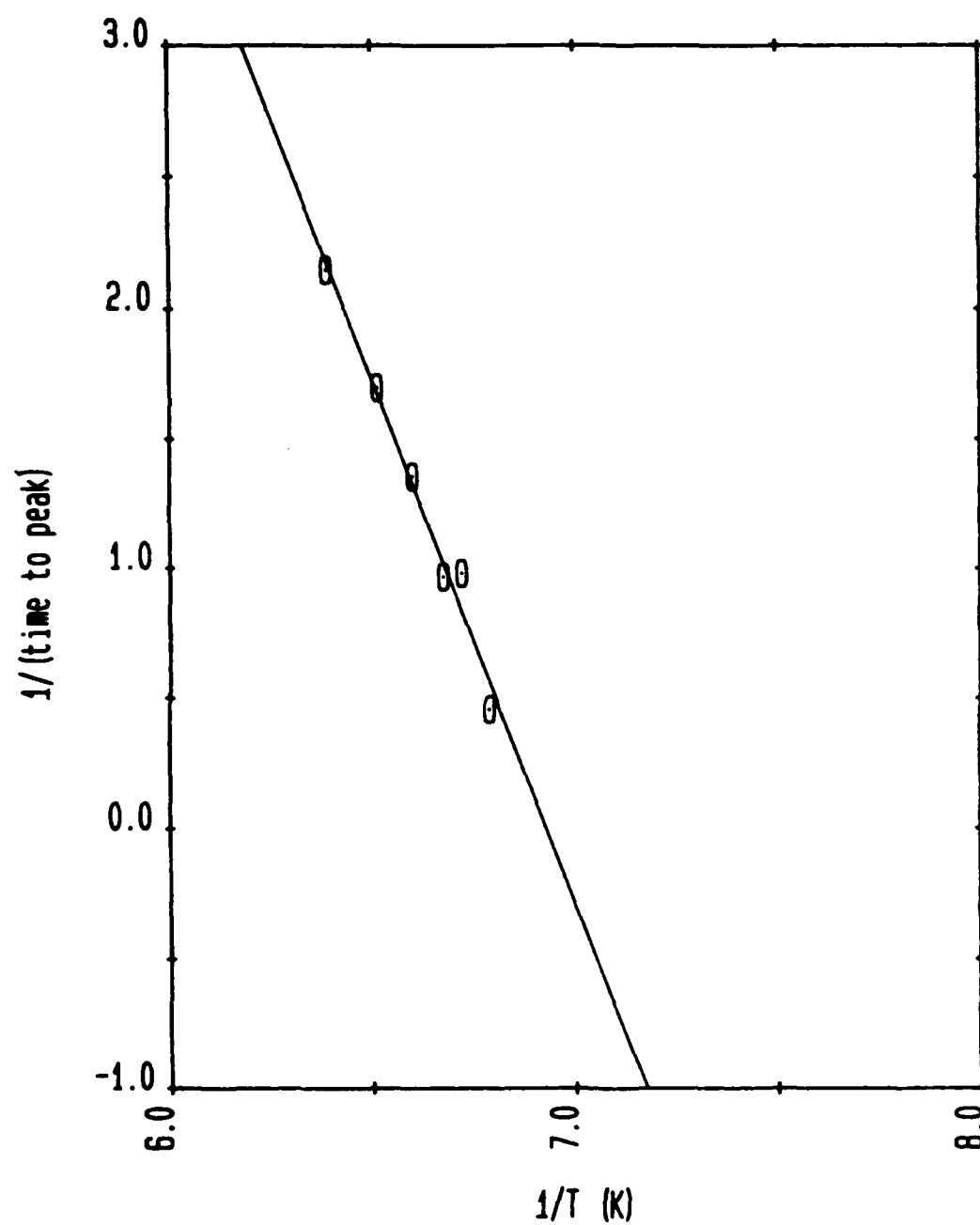


Figure B-3 B-type 11 micron.

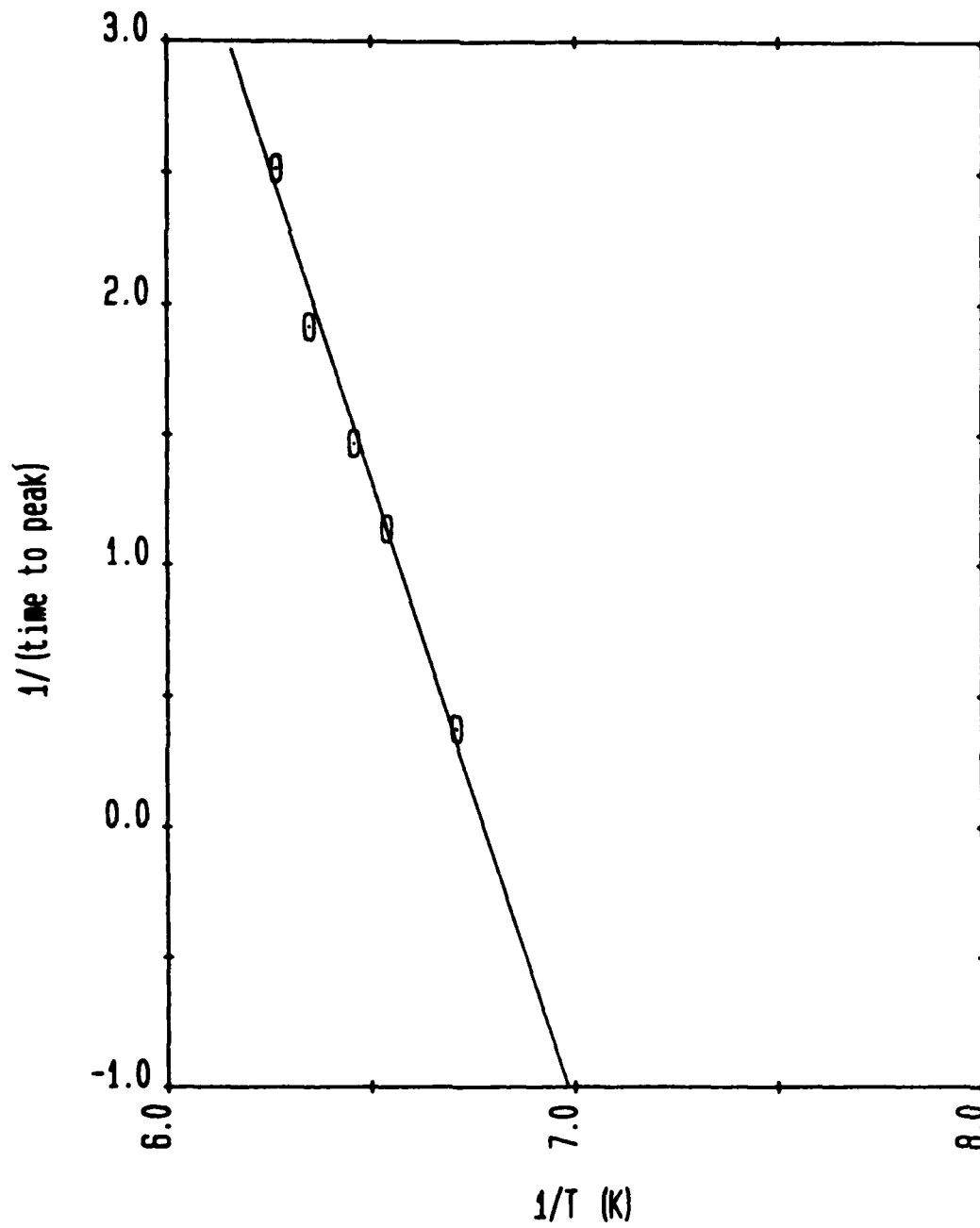


Figure B-4 B-type 11 micron OsRu coated.

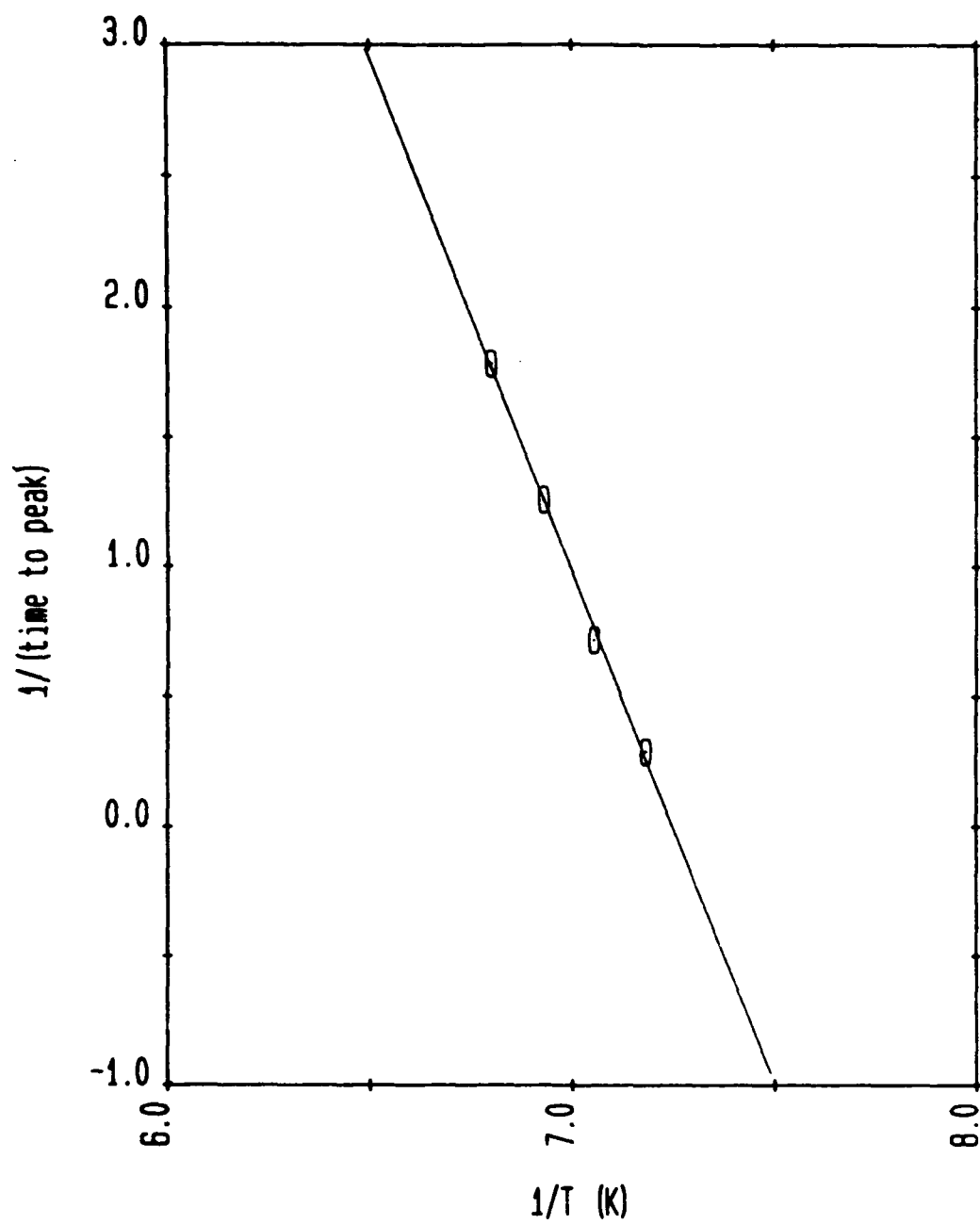


Figure B-5 S-type 5 micron tungsten.



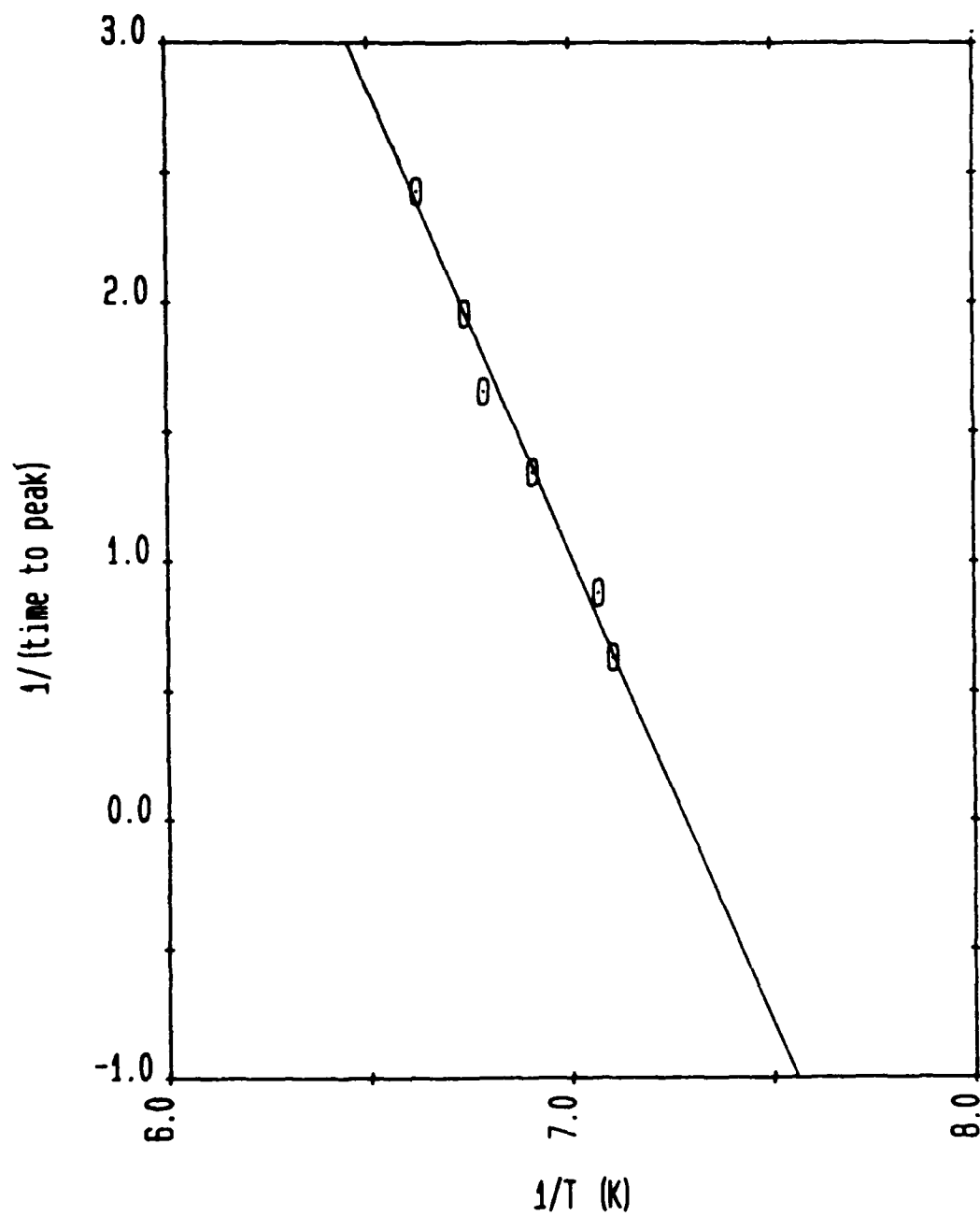


Figure B-6 S-type 5 micron OsRu coated.

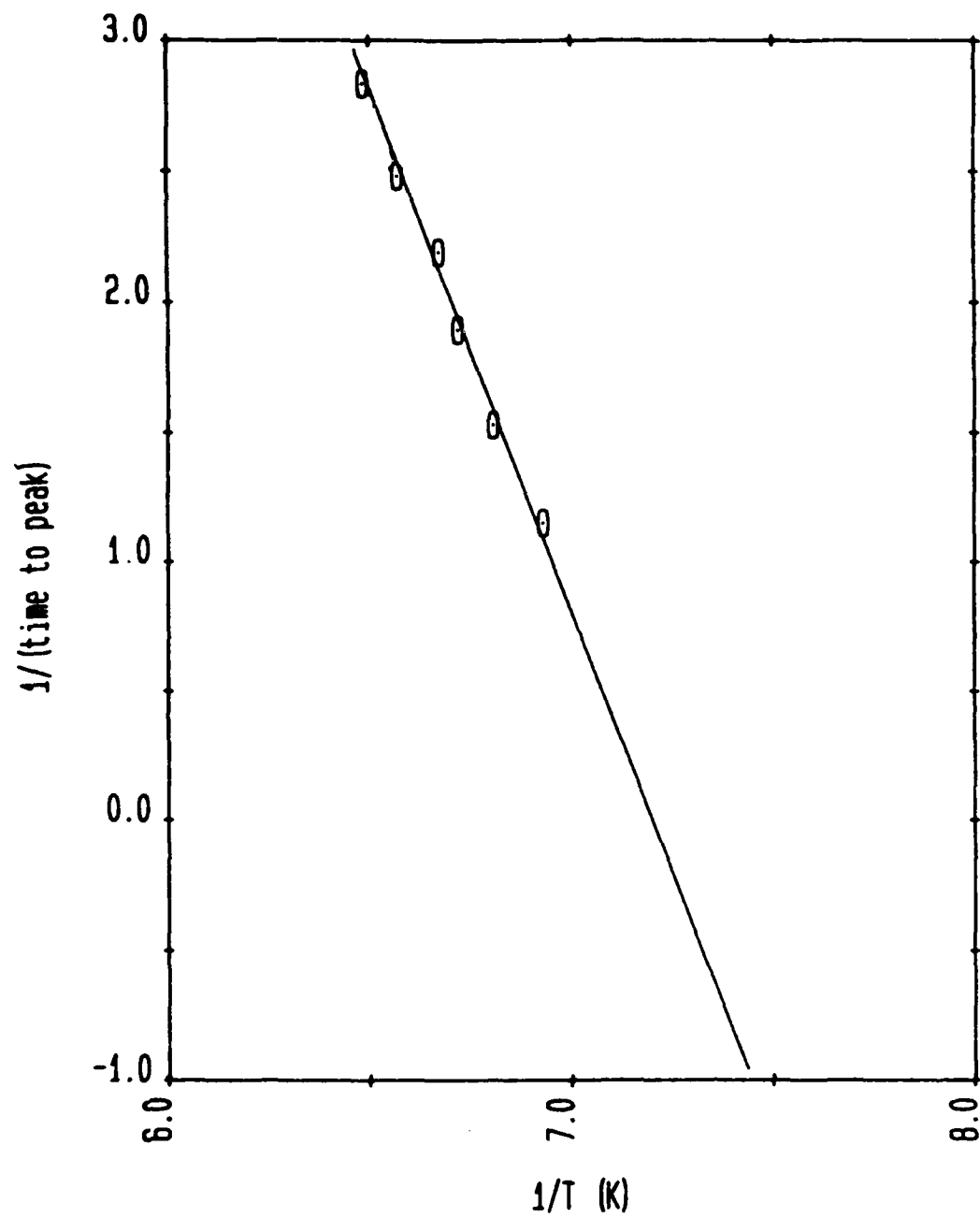


Figure B-7 S-type 11 micron tungsten.

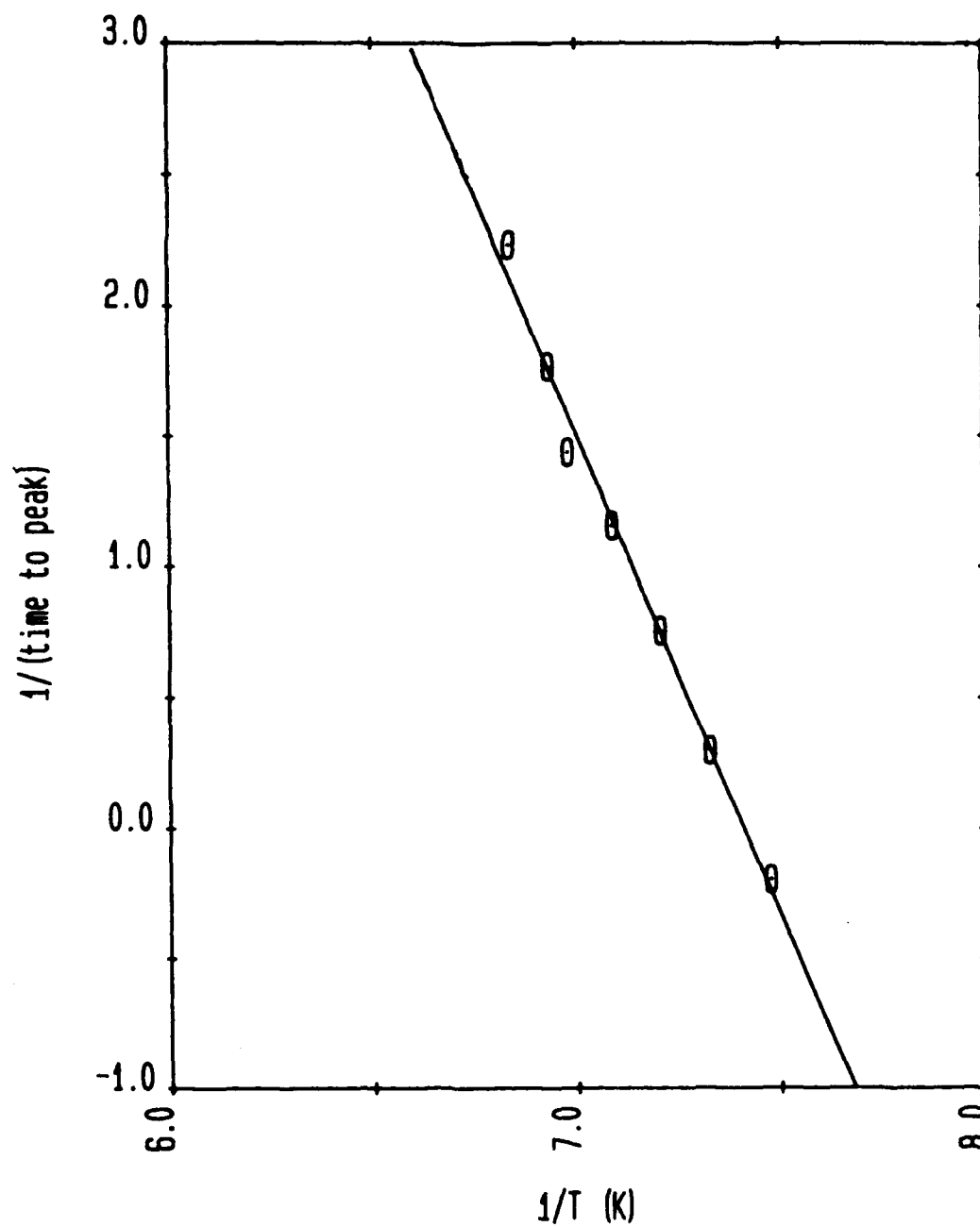


Figure B-8 S-type 11 micron OsRu coated.

END

11-87

DTIC